A FUEL CELL SINGLE PHASE AC POWER GENERATION SYSTEM WITH GALVANIC ISOLATION

PRABHURAJ SHANMUGHAM

A Thesis Submitted to the Graduate School of Naresuan University
in Partial Fulfillment of the Requirements
for the Doctor of Philosophy Degree in Renewable Energy
December 2017

Thesis entitled "A fuel cell single phase AC power generation system with galvanic isolation"
By Mr. Prabhuraj Shanmugham
has been approved by the Graduate School as partial fulfillment of the requirements for the Doctor of Philosophy Program in Renewable Energy of Naresuan University

Oral Defense Committee

Thavatchai Tayjasanant
.... Chair
(Associate Professor Thavatchai Tayjasanant, Ph.D.)

.... Advisor
(Assistant Professor Sakda Somkun, Ph.D.)

.... Internal Examiner
(Assistant Professor Nipon Ketjoy, Ph.D.)

C. Sirisamphanwong
.... Internal Examiner
(Chatchai Sirisamphanwong, Ph.D.)

Approved

....
(Associate Professor Paisarn Muneesawang, Ph.D.)
Dean of the Graduate School

14 DEC 2017

ACKNOWLEDGEMENT

I would like to express my sincere gratitude to my advisor, Assistant Professor Dr. Sakda Somkun, for his initial idea, support, guidance and encouragement which enabled me to carry out my research successfully.

I would like to thank the Director, Dr.Sukruedee Sukchai and all the Professors of School of Renewable Energy Technology, Naresuan University who have mentored in all means during the course of my study.

My sincere thanks to the Management of Hindustan University, Chennai, India and the Management of Naresuan University, Phitsanulok, Thailand for providing me the Scholarship for my entire study.

I would like thank and appreciate all my friends for their constant support both technically and morally throughout my study and life.

I gratefully appreciate my beloved family for their love, support and encouragement throughout my life.

Finally, I thank the Almighty God for His Blissful Blessings which made everything possible.

Prabhuraj Shanmugham

Title	A FUEL CELL SINGLE PHASE AC POWER GENERATION SYSTEM WITH GALVANIC ISOLATION
Author	Prabhuraj Shanmugham
Advisor	Assistant Professor Sakda Somkun, Ph.D.
Academic Paper	Thesis Ph.D. in Renewable Energy, Naresuan University, 2017
Keywords	Fuel cell power generation, dual active bridge, DC-DC converters, *LCL* filter, grid connected inverter

ABSTRACT

Fuel cell system is a promising alternate way of power generation from clean, green fuel such as Hydrogen with almost zero emissions. It can be a primary power to the local loads or an aiding power to the grid during instability in the case of distributed generation. The grid connected fuel cell systems experience double line frequency ripples from the power converters such as the inverters which affect the life of fuel cells. The current ripples in the fuel cell systems are limited within 15% for safe and reliable operation of the fuel cells. This study presents design of a $1kW$ grid connected single phase fuel cell power generation system with galvanic isolation. This involves the design of a dual active bridge DC-DC converter to boost the low voltage DC output from fuel cells and a grid synchronized single phase PWM inverter with unbalanced synchronous reference frame grid current control suitable for fuel cell systems.

There are many topologies available for DC-DC converters and the Dual Active Bridge (DAB) topology is found to be more suitable for fuel cell applications due to various advantages such as high power density, high efficiency, Zero Voltage Switching (ZVS) capability and galvanic isolation. The inherent ZVS and galvanic isolation nature of DAB made it suitable for fuel cell power conditioning system. The fuel cells are generally low voltage systems which need isolated converters in case medium and high power applications for safety operations. An average current modeling of DAB is presented in this study with a PI controlled DC bus voltage control loop. An optimum bandwidth of the DC bus voltage control loop has been found to limit the injected double line frequency current ripples to the fuel cell system. A simple phase shift modulation in open loop is used to transfer the required amount of power from fuel cell to the grid.

The modeling and designing of a grid connected single phase inverter is done with *LCL* line filter. An unipolar PWM scheme is used for switching pattern generation due to lower harmonics compared to its counter part bipolar PWM. An *LCL* line filter is chosen for higher ripple attenuation over *L* and *LC* filters. A careful design of *LCL* filter is done as the controlling is complex due to its inevitable resonance behavior. An unbalanced synchronous reference frame grid current control is employed for stable operation of the system. This also enables an independent control of real and reactive power injections into the grid with $d-axis$ and $q-axis$ current controls respectively. Extended Symmetrical Optimum method is used to optimally tune the PI controllers. MATLAB®/ Simulink is used for the design and is verified with a 1kW Horizon PEM fuel cell system. Phase shift modulation is used to control the power export with measured *THDi* of 2% in the grid current. The overall DAB and inverter system efficiency is measured to be 86%.

LIST OF CONTENTS

Chapter **Page**

III RESEARCH METHODOLOGY

LIST OF CONTENTS (CONT.)

Chapter **Page**

IV RESULTS AND DISCUSSION

LIST OF TABLES

Table **Page**

LIST OF FIGURES

Figure **Page**

LIST OF FIGURES (CONT.)

Figure **Page**

LIST OF FIGURES (CONT.)

Figure **Page**

ABBREVIATIONS

°C	Degree Centigrade
A	Amperes
AC	Alternating Current
AFC	Alkaline Fuel Cell
C_b	Base capacitance (F)
C_{dc}	DC link capacitance (F)
C_f	Filter capacitance (F)
CHP	Combined Heat and Power
CO_2	Carbon di oxide
CSI	Current Source Inverter
d	Primary referred voltage transfer ratio
DAB	Dual Active Bridge
dB	Decibel
DC	Direct Current
DMFC	Direct Methanol Fuel Cell
DSP	Digital Signal Processor
e^-	Electron
f_1	Modulating frequency (Hz)
FC	Fuel Cell
f_g	Grid frequency (Hz)
f_r	Resonance frequency (Hz)
f_{sw}	Switching frequency (Hz)
H^+	Proton
H_2	Hydrogen
H_2O	Water
$i_c(t)$	Current through L_c
$I_{FC_{ave}}$	Average current drawn from fuel cell (A)
$i_p(\theta)$	Primary current at any instant θ
$i_s(t)$	Grid current (A)

ABBREVIATIONS (CONT.)

kHz	Kilo Hertz
kW	Kilo Watt
L/min	Liter / min
L_c	Inverter side inductance (H)
LCL	Inductor Capacitor Inductor
LF	Loop Filter
L_{lk}	Leakage inductance (H)
LPF	Low Pass Filter
L_s	Grid side inductance (H)
m_a	Amplitude modulation ratio
MCFC	Molten Carbonate Fuel Cell
m_f	Frequency modulation ratio
MW	Mega Watt
O_2	Oxygen
OECD	Organization for Economic Cooperation and Development
OH^-	Hydroxyl
PAFC	Phosphoric Acid Fuel Cell
PD	Phase Detector
PEMFC	Proton Exchange Membrane Fuel Cell
$P_{FC_{ave}}$	Average power drawn from fuel cell (W)
PI	Proportional Integral
PLL	Phase Locked Loop
PWM	Pulse Width Modulation
QSG	Quadrature Signal Generator
R_c	Winding resistance of inverter side inductance (ohms)
RMS	Root Mean Square
R_s	Winding resistance of gird side inductance (ohms)
S_n	Apparent power (kVA)
SOFC	Solid Oxide Fuel Cell

ABBREVIATIONS (CONT.)

V	Volts
V_α	α - axis component of grid voltage (V)
V_β	β - axis component of grid voltage (V)
V_d	d- axis component of grid voltage (V)
V_{FC}	Fuel cell output voltage (V)
V_q	q - axis component of grid voltage (V)
V'_{dc}	Primary referred secondary voltage (V)
VAC	AC voltage (V)
V_{cf}	Voltage across the filter capacitance C_f (V)
VCO	Voltage Controlled Oscillator
$V_{control}$	Sinusoidal Modulating signal (V)
V_{dc}	DC link voltage (V)
v_s	RMS grid voltage (V)
VSI	Voltage Source Inverter
V_{tri}	Triangular - Carrier signal (V)
W	Watt
Wh/l	Watthour/litre
Z_b	Base impedance (ohms)
ZCS	Zero Current Switching
ZVS	Zero Voltage Switching
ϕ	Phase shift between input and output bridge of DAB

CHAPTER I

INTRODUCTION

In recent years, to meet the world energy crisis and to mitigate the global warming, the use of renewable energy has become prominent in today's world of power generation. The world's primary energy consumption during the year 2014 was contributed by various resources viz. 32.6% by Oil, 30.0% by coal, 23.7% by natural gas, 6.8% by hydroelectric and 4.4% by nuclear (1), which clearly shows energy from the fossil fuels dominates the energy sector which is the world concern now. Renewable energy used in power generation grew by 12.0% accounting for a record 6.0% of global power generation (1).The energy sectors have started focusing on alternate energy sources such as Wind, Solar and other renewable energy resources as there is a continuous increase in the use of renewable sources at a rate of 3.0% in 2014 an up of 0.9% from a decade ago (1).

Most of the alternative energy sources are intermittent by nature as shown in figure 1, where there is always a gap between the power generated and the power demanded. Thus the system should be such that the excess power generated is stored in a

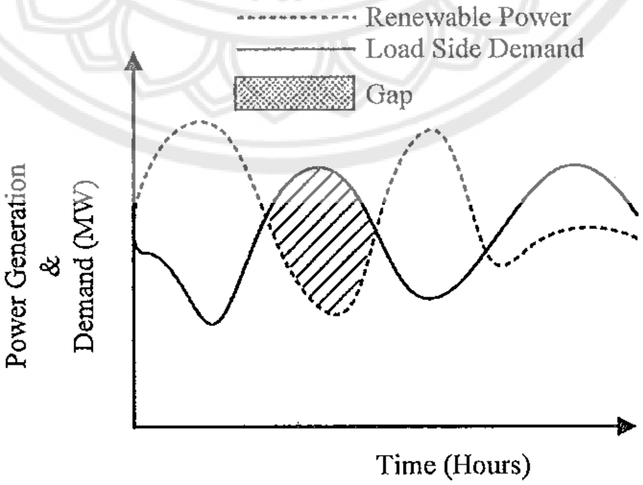

Figure 1 Intermittent Nature of Renewable Power Generation

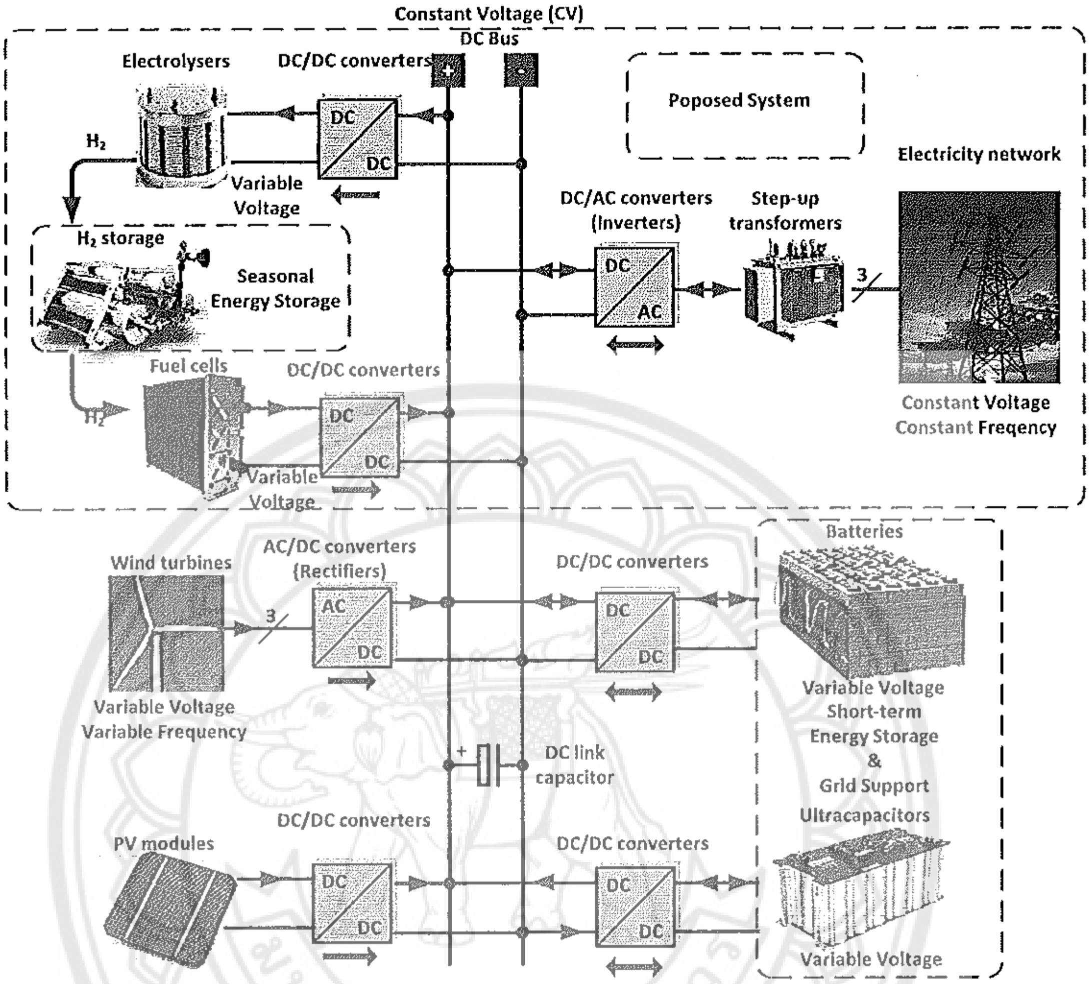

Figure 2 Renewable Power System Integration

storage system and the same is delivered when needed. Moreover as the power generated from these sources are fluctuating at times in addition to intermittent, and hence needed to be conditioned to give a constant output for any kind of load or grid integration.

Hydrogen gas is one such promising clean energy storage which can be used for small and medium scale applications in which the production of hydrogen from/by renewable energy sources makes it as a green fuel. Fuel cells can then be used to convert the stored chemical energy from the Hydrogen gas to electricity. Being a chemical device, the fuel cell produces directly the electricity without any intermediate stage has recently drawn much attention of researchers. The most significant advantages are low emission of green house gases and high power density. The emission consists of only harmless gases and water and the noise emission is low. The energy density of a typical fuel cell is 200 Wh/l, which is nearly 10 times of a battery and the efficiency of the fuel cell is quite high [40%-60%]. The waste heat generated by the fuel cell can be used for co-generation such as steam, air conditioning, hot air and heating, then the overall efficiency of such systems could be as high as 80% (2)

The hydrogen storage system can be integrated with the other renewable systems as proposed in figure 2 to overcome the intermittency of certain energy sources. This can aid the grid in case of instability due to the intermittent nature of the renewable energy sources. In such integration the power conditioning circuits such as DC-DC converters and DC-AC inverters are inevitable in the system as shown in figure 2. Power electronics, the technology of efficiently processing electric power, plays an essential part in the integration of the dispersed generation units for good efficiency and high performance of the power systems (2). These power conditioning circuits in addition to give constant power output, also deliver the power at the required electrical specifications such as voltage, frequency and power factor as per the load or grid requirement.

This study aims at 1 kW AC power generation at 230 VAC, 50 Hz by a Hydrogen Fuel Cell with Grid integration, which involves the modeling and design of a Dual Active Bridge (DAB) with the High Frequency Transformer and a single phase inverter. Basically any kind of DC sources with the specific DC voltage range can be used to feed the circuit for single phase AC power generation for any portable applications or grid integration.

Rationale/Statement of the Problem

Most of the Renewable Energy Resources are intermittent power sources and paves the path for the need of storage systems to store the power when in excess and deliver it on demand. There exists many kinds of storage systems in practice such as Batteries which store the electrical energy in the form of chemical energy, Ultracapacitors which store the electrical energy in the form of static electricity and other thermal energy storage systems. One such energy storage system is in the form of Hydrogen gas. Hydrogen storage has advantage over the other storage systems that the amount of stored Hydrogen will be available forever unless there is a leakage in the system, but the

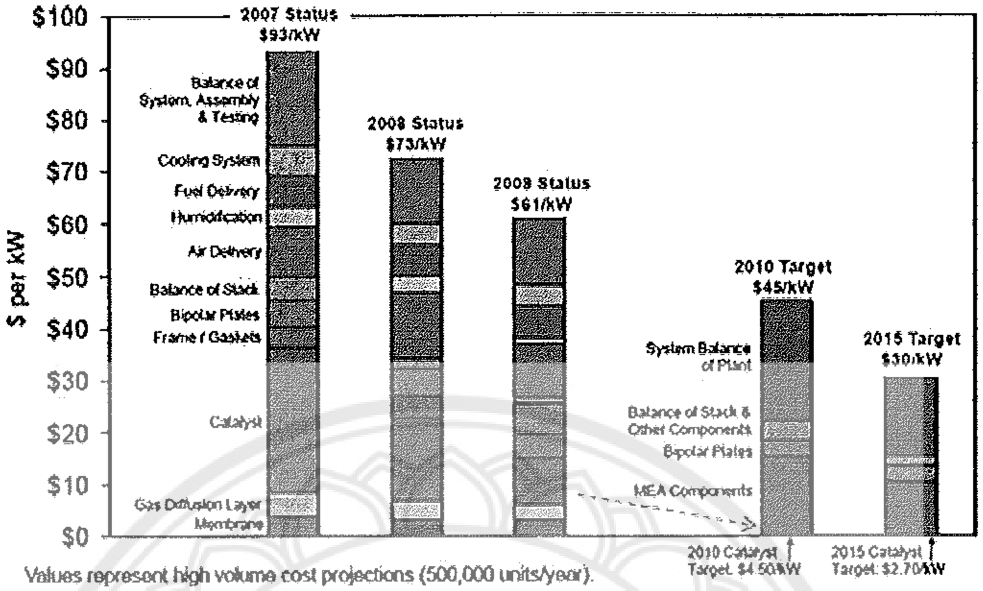

Figure 3 Production cost of fuel cells (3)

other storage systems like Batteries, Ultracapacitors etc., lose the energy stored due to unavoidable discharge. Hence systems exist in which the available renewable energy is utilized to produce hydrogen by electrolysis or to convert hydrocarbons into hydrogen gas and is stored in a better way for further usage. Hydrogen being a clean and renewable energy fuel which results with water as a by-product in power generation is one of the most suited non-conventional energy resources to meet the energy demand in small scale.

Though hydrogen is clean and can be made available easily, the use of fuel cells has not reached like any other non-conventional renewable energy resources. This may be due to the safety reasons in handling the Hydrogen gas, cost and life of the Fuel Cells which generate electricity from Hydrogen. But many attempts have been made to improvise the performance and life of the fuel cells in recent years. The production cost has been declining over years and it is targeted to be $ 30 /kW by the year 2015 as shown in the figure 3 (3).

The fuel cell polarization curve shown in figure 4, gives the typical characteristics of the PEM fuel cell. The key points to be noticed in the figure 4, which is the plot of the cell voltage against current density are (4),

1. Even the open circuit voltage is less than the theoretical value of the cell

voltage.

2. There is a rapid initial fall in voltage.

3. The voltage then falls less rapidly, and more linearly.

4. There is a region with higher current density at rapid the voltage falls.

Hence an appropriate control scheme should be implemented to ensure the fuel cell stack operation in its linear region. The low voltage DC has to be boosted to a high value before inverting it to AC. The value of the high voltage DC should be at least the peak value of the AC signal required. There are many topologies proposed in various literatures (5–11) which are mainly classified as topologies with galvanic isolation and topologies without isolation. The systems without galvanic isolation has advantage of simple in construction and can be used for low power applications. But in the case of high power handling, it is necessary to have galvanic isolation. In addition to isolation, such topologies provide ease of matching the voltage levels at different ports and bidirectional power flow. One of the topologies proposed in (5) which is shown in figure 5 has advantages with soft switching and high power density and hence is chosen as the suitable topology in this study.

To summarize, this study aims to generate the single phase AC power from the

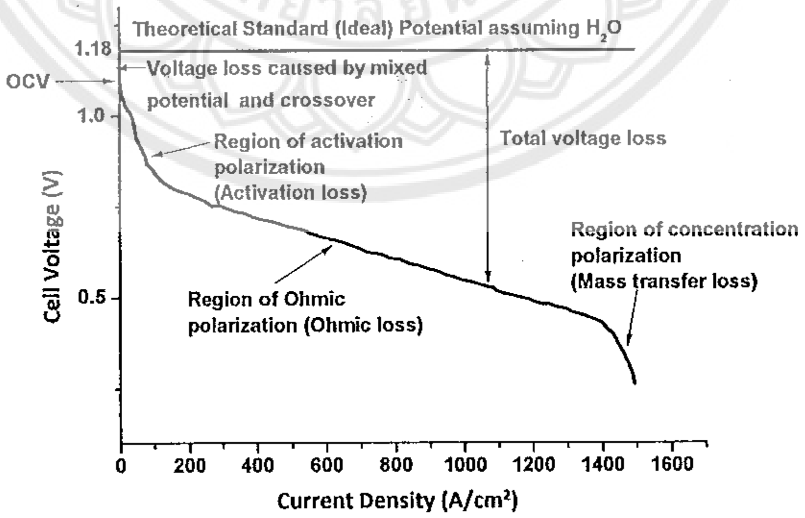

Figure 4 Typical polarization curve of PEMFCs. (4)

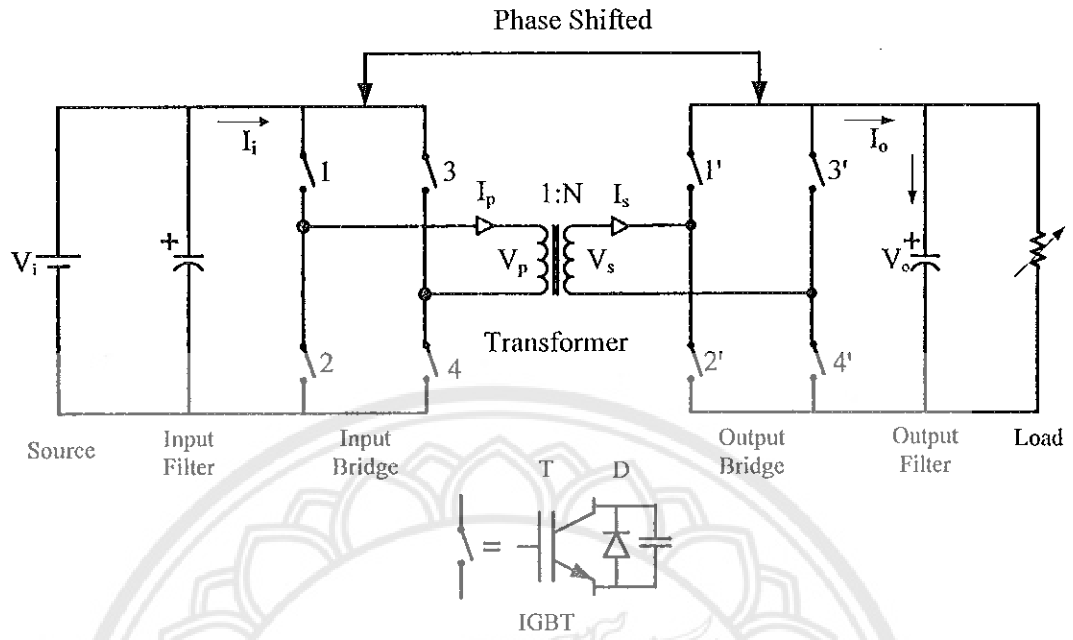

Figure 5 DAB Topology as proposed in (5)

Fuel Cell's low voltage DC power with the help of DAB and a single phase inverter with grid integration. Since the Hydrogen fuel is a stored energy, the power generation is not intermittent and as long as the fuel cell is fueled, it generates DC power. This can be a supporting system to the existing other renewable systems in case of intermittency or fluctuations. This keeps the grid to be healthy from voltage and frequency fluctuations. Hence the study involves the design of a soft switched Dual Active Bridge with high power density with compact high frequency transformer and a single phase inverter. A suitable control scheme is to be implemented in DSP to meet the needs of the grid.

Purposes of the Study

The purposes of the study are

1. To design and construct a Dual Active Bridge converter to convert a low voltage DC output of a 1 kW Proton Exchange Membrane Fuel Cell to a high voltage DC.

2. To implement a suitable control scheme for the Dual Active Bridge to regulate the output voltage and to control the power flow.

3. To design and construct a single phase inverter to convert the high voltage DC power output of Dual Active Bridge into a single phase AC power.

4. To implement a suitable control scheme to regulate the AC output of the single phase inverter.

5. To evaluate the efficiency of the Dual Active Bridge and the single phase inverter with Total Harmonic Distortion.

Scope of the Study

The scope of the study is limited to

1. Design the Dual Active Bridge to operate the 1kW PEM Fuel Cell in the linear region of polarization curve with 43V at 23.5A.

2. Generate 1kW AC power at 230V, 50Hz for the Thailand grid tied applications.

3. Choose the switching frequency of DAB at 20 kHz due to the constraints on the magnetic core materials.

Significances of the Study

The significances of the study are,

1. Designing of Dual Active Bridge with High Frequency Transformer will significantly reduce the size of the transformer with galvanic isolation.

2. DAB can be operated in ZVS resulting in high efficiency.

3. Portable power generation enables to meet the power demands in remote areas on emergency basis.

4. A substitute to the other renewable sources of energy in case of their fluctuations.

5. Being clean green fuel power generation, earns the carbon credits with zero pollution.

CHAPTER II

THEORETICAL BACKGROUND AND RELATED LITERATURES

This section describes the theoretical basics of hydrogen fuel cells, power conditioning circuits, line filters and control techniques along with related literatures.

World Energy Crisis

An estimated one billion ninety-five million people (1,095,000,000) live without electricity in this world (12). Still most of the rural and remote areas of the developing and under developed countries are in dark. A kerosene lamp emits between 3 and almost 40 times more CO_2 emissions than a grid-connected compact fluorescent lamp based on the energy mix (13). On the other hand there has been a constant increase in the energy demands both in the form of electricity and other forms like oil etc., in the urban areas of the developed countries. Despite rising energy use, global CO_2 emissions associated with energy consumption remained stable over the course of the year while the global economy grew. The landmark decoupling of economic and CO_2 growth is due in large measure to increased use of renewable resources, and efforts by countries in the OECD to promote renewable energy and energy efficiency. The energy sectors have started decoupling the emission growth from that of the economic growth by adopting measures of long term commitment to a maximum global temperature rise of 2°C by 2020 (13). The figure 6 shows the renewable energy contribution in the year 2013 in the primary energy consumption (12). There has been an considerable increase in the contribution of the energy supply by renewable sources. This increase in the renewable energy contribution needs the developments in the fields of power conditioning circuits so as to maintain the power quality at the delivery.

Alternative Energy Sources and Fuel Cell Power Generation

The conventional power stations are located geographically at different places and the power generated is to be transmitted over a long distance transmission lines to meet the load centers. The power quality is also to be continuously monitored and controlled. Due to the situation on uncertain future power demands investors are reluctant in long term capital investments in the construction of large scale power plants and also keeping away from investing in the infrastructure development for transmission and distribution (14).Recently large number of dispersed generation units are being installed with Combined Heat and Power (CHP) stations due to the wide spread use of renewable energy. Though the renewable energy sources eliminate harmful emissions, the availability of such sources depends on seasonal weather patterns. Hence it would be difficult to have a power system only with renewable power generation due to their intermittency. The better way is to integrate them with the grid, normally at distribution level (2). Power generation from fuel cells is one of the promising solutions in the form of dispersed power. Fuel cells not only find importance in dispersed power generation but also in vehicular technologies as a substitute to internal combustion engines to mitigate the global warming, the fossil fuel depletion and the energy crisis (15).

Hydrogen Fuel Cells

Basic Principles

The basic principle of fuel cell is very simple. It works under the principle of reverse electrolysis. During electrolysis the water is split into hydrogen and oxygen with the help of electricity. But in the fuel cells the electrolysis process is reversed to

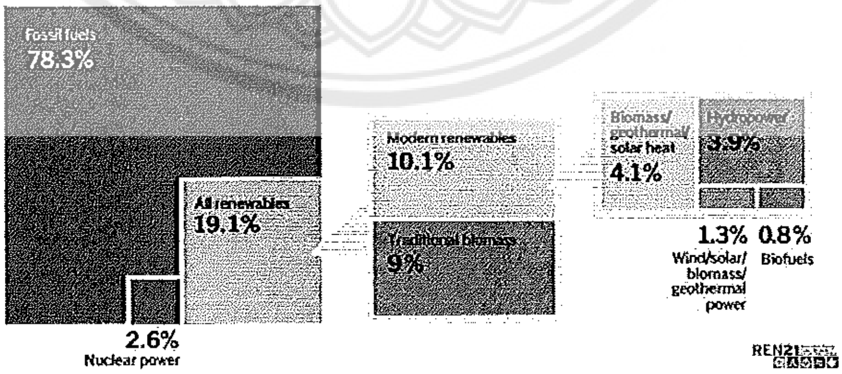

Figure 6 Estimated renewable energy share of global final energy consumption, 2013 (12)

produce electricity. In the reverse electrolysis the hydrogen and oxygen are recombined to produce electric current. It can also be seen in equation 2.1 as combustion of hydrogen in the presence of oxygen which produces electric current instead of heat liberation.

$$2H_2 + O_2 \longrightarrow 2H_2O \qquad (2.1)$$

In general the electric current produced is very small. This is due to the contact area between the gas and the electrodes being small and the distance between the electrodes is large enough to have higher resistance by the electrolyte. Flat electrodes to increase the surface area and thin layer of electrolyte to reduce the resistance as shown in the figure 7 can be a solution to increase the current production. The electrodes are porous in nature so that the gas and electrolytes penetrate from the respective sides to give maximum possible contact. The production of electrons from hydrogen and oxygen is based on the reactions which take place at the electrodes. The reaction at the electrodes varies depending on the type of fuel cells. The basic reactions in an acid electrolyte fuel cell are given in the equations 2.2 and 2.3.

At anode the hydrogen gas is ionized where electrons [e^-] are released and protons [H^+] are produced.

$$2H_2 \longrightarrow 4H^+ + 4e^- \qquad (2.2)$$

At cathode oxygen reacts with the electrons [e^-] and protons [H^+] resulting in water.

$$O_2 + 4e^- + 4H^+ \longrightarrow 2H_2O \qquad (2.3)$$

Hence as shown in the figure 8 the electrons produced should pass through an electrical circuit and the protons should pass through an electrolytic medium which has free protons. An acid which is rich is free protons or a polymer membrane which is made to have mobile protons can be used as electrolyte. In latter case it is called as *proton exchange membrane* as H^+ ions are called protons.

In alkaline electrolyte fuel cell, overall reaction is the same, but the reactions at electrodes are different. In alkaline electrolyte, hydroxyl ions are available for mobility.

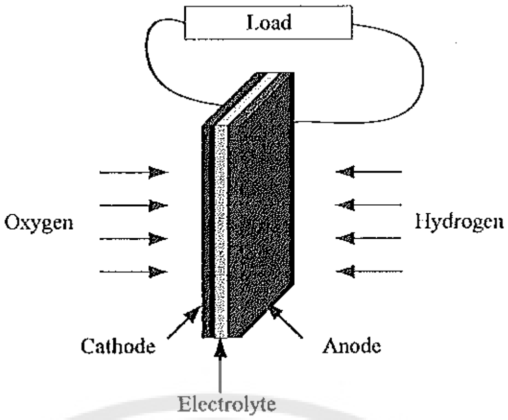

Figure 7 Basic cathode-electrolyte-anode construction of a fuel cell (4)

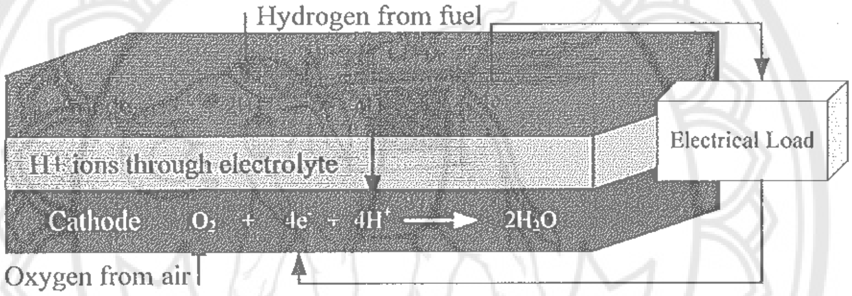

Figure 8 Reaction in acid electrolyte fuel cell (4)

These OH⁻ ions react with the hydrogen to release electrons at anode, the oxygen and water from electrolyte reacts with these electrons to form hydroxyl OH⁻ ions.

The reactions are as shown below.

At anode

$$2H_2 + OH^- \longrightarrow 4H_2O + 4e^- \tag{2.4}$$

At cathode

$$O_2 + 4e^- + 2H_2O \longrightarrow 4OH^- \tag{2.5}$$

In the case of alkaline electrolyte the OH⁻ ions pass through the electrolyte. The reaction at electrodes and the movement of ions are illustrated in figure 9.

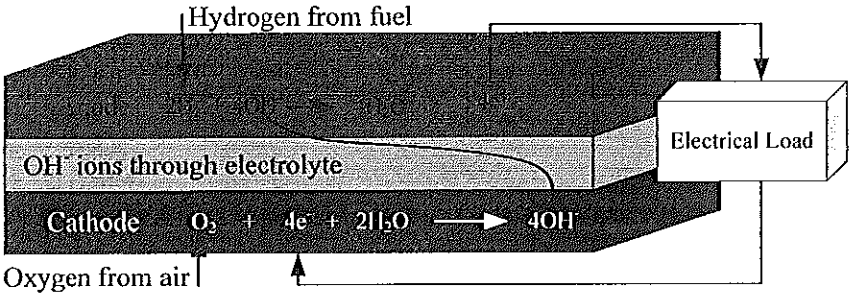

Figure 9 Reaction in alkaline electrolyte fuel cell (4)

Types of Fuel cells

The fuel cells are mainly classified into different types based on the type of electrolyte. There are six different types are available for usage as listed in the table 1.

Table 1 Different types of fuel cells

Fuel cell type	Mobile ion	Opearting temperature	Application and remarks
Basic cathode-electrolyte-anode construction of a fuel cell Alkaline (AFC)	OH^-	50-200°C	Used in space vehicles.
Proton exchange membrane (PEMFC)	H^+	30-100°C	Vehicles and mobile applications and for low power CHP systems
Direct methanol (DMFC)	H^+	20-90°C	Suitable for portable electronic systems of low power, running for long times
Phosphoric acid (PAFC)	H^+	~ 220°C	Large numbers of 200-kW CHP systems in use
Molten carbonate (MCFC)	CO_3^{2-}	~650°C	Suitable for medium to large scale CHP systems, upto MW capacity.
Solid oxide (SOFC)	O^{2-}	500-1000°C	Suitable for all sizes of CHP systems, 2kW to multi-MW.

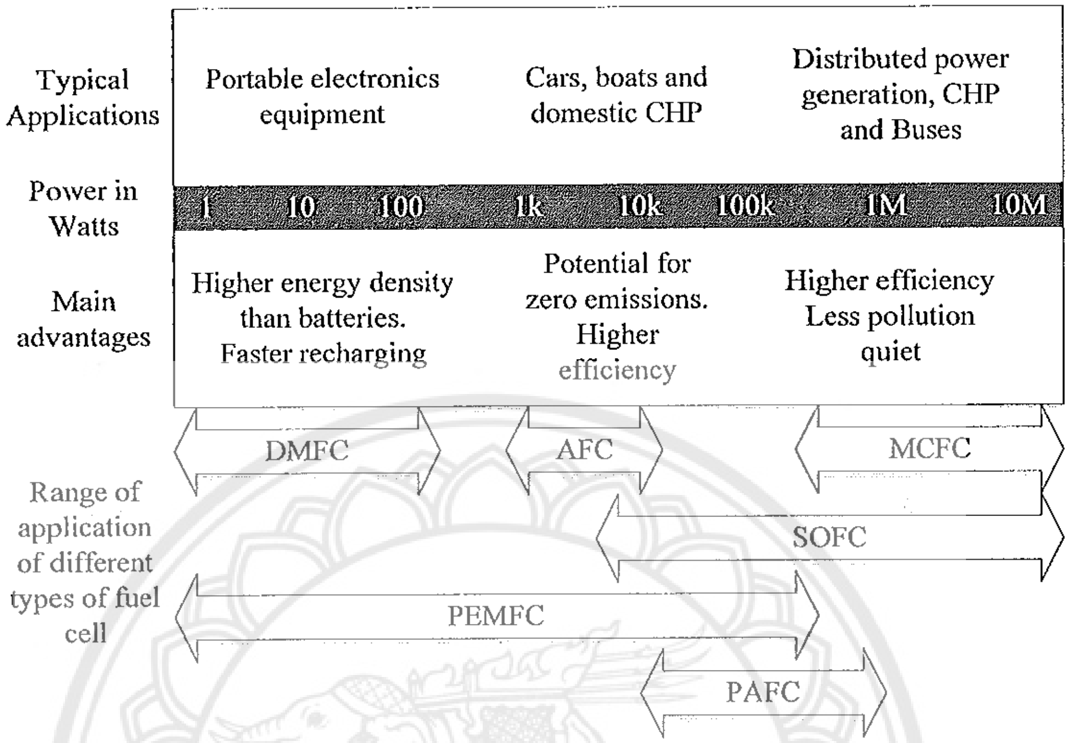

Figure 10 Summary of applications and advantages of fuel cells

The proton exchange membrane (PEM) is a simple type in which solid polymer is the electrolyte and protons pass through. It is can operate in low temperatures and in any orientation. It can be fed from a ultra-pure hydrogen source to produce electricity. Other types of fuel cells and their major applications are as listed in the table 1.

Advantages of Fuel cells

The major disadvantage of all types of fuel cells are their higher cost. However due to various other advantages and ongoing cost reduction (3), the fuel cells are increasingly employed in automobiles and distributed power generation with combined heat power (CHP) solutions. The wide range of fuel cells based on types, application are given in the figure 10. The typical advantages of using fuel cell are listed below.

1. Efficiency: Fuel cells are generally efficient than the combustion engines either piston based or turbine based. Even small capacity fuel cells are also as efficient as that of the larger ones.

2. Simplicity: These are essentially simple with few moving parts, which make them to be reliable and long lasting systems.

3. Low emissions: The only by-product of fuel cell reaction are water and heat. As the heat can be recovered it can be a "zero emission" system. This is a main advantage in using fuel cells in vehicles to mitigate the emissions, however it should also be noted that the production of hydrogen results in the emission of CO_2.

4. Silence: Fuel cells are very quiet, even those with extra fuel processing units. This is an important feature in portable systems and distributed CHP systems.

Fuel cell characteristics

The typical value of a single cell fuel cell is 1.2 V when operated below 100°C. In general, these single cells are stacked together to increase the voltage level to a required value. However, when the fuel cells are put under use, the voltage drops below the typical value as shown in the figure 4. The polarization curve of the Horizon®is as shown in the figure 11.

The characteristics of the fuel cell changes as the operating temperature. These changes in the shape of the polarization curve depend on the irreversibilities as detailed below.

1. Activation losses : This is due to the slowness of the chemical reactions at the different electrodes. Some amount of the voltage produced is utilized for the chemical

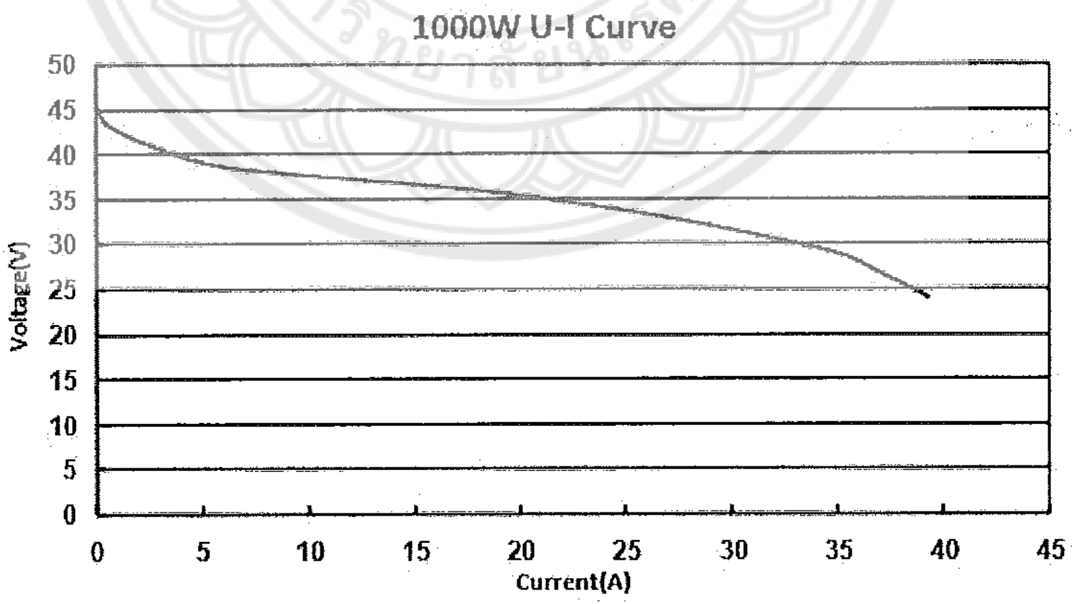

Figure 11 Characteristics of Horizon Fuel Cell H1000

reaction in order to mobilize the electrons. The voltage drop due to the activation losses is highly non-linear in nature.

2. Fuel crossover and internal currents : This energy loss is due to the waste passing of fuel and electrons through the electrolytes. Ideally only the ions should pass through the electrolytes and electrons through the electrical circuits. But practically a very few amount of fuel and electrons pass through the electrolytes. But loss is considerable in low temperature fuel cells typically in case of direct methonal cells.

3. Ohmic losses : This loss is due to the resistance offered by the electrodes and connections to the flow of electrons and the resistance offered by the electrolytes to the flow of ions. The voltage drop due to this loss is directly proportional to the current density and they are linear, hence these are called as ohmic or resistive losses.

4. Mass transportation or concentration losses : For a proper chemical reaction at the surface of the electrodes, required amount of reactants should be available as the reaction is continuous and fuel is being consumed. The loss due to the unavailability of required concentration of the reactants at the time of reaction is called concentration loss. This is due to the failure of the transportation of the required mass and hence is also called as mass transportation loss.

Selection of Fuel cell for Power Generation

Considering the advantages such as low operating temperatures, suitable for low power CHP applications, and can operate in any orientation, PEM fuel cell is selected for this study and a 1kW PEMFC from Horizon®has been used. The specification of the Horizon fuel cell is listed in the table 2. These specifications of Horizon's PEM fuel cell and its polarization curve shown in the figure 11 clearly show that the fuel cell has a low voltage DC output which varies with the current drawn. Hence the system needs a power conditioner to regulate the output and to operate in its maximum power point in the ohmic region. In this study as the fuel cell system is aimed to be a supportive system to the electrical grid in case of instability caused due to intermittent nature of renewable energy resources, the low voltage DC output voltage should be boosted to a high voltage DC for further conversion to AC for grid integration. The existing DC-DC converters to boost the low voltage DC power output to a high voltage DC power output are further studied to select the suitable converter for fuel cell applications.

Table 2 Technical specifications of 1000W Horizon®fuel cell

Description	Remarks
Type of fuel cell	PEM
Number of cells	48
Rated power	1000 W
Performance	28.8V @ 35A
H_2 Supply valve voltage	12V
Purging valve voltage	12V
Blower voltage	12V
Reactants	Hydrogen and Air
External temperature	5 to 30°C
Max. stack temperature	65°C
H_2 Pressure	0.45-0.55 bar
Hydrogen purity	$\geq$ 99.995 % dry H_2
Humidification	Self-humidified
Cooling	Air (Integrated with cooling fan)
Stack weight (with fan and casing)	4000 grams(± 100grams)
Controller weight	400 grams(±30grams)
Dimension	23.3cm x 26.8cm x 12.3cm
Flow rate at max output	13 L/min
Start up time	$\leq$30 Sec at ambient temperature
Efficiency of stack	40% @ 28.8V
Low voltage shut down	24V
Over current shut down	42A
Over temperature shut down	65 °C
External power supply	13V(±1V),8A

Fuel cell power conditioning circuits

DC-DC converters

The inherent properties of fuel cells such as low output voltage which varies with aging and current drawn, reduction in the efficiency due to higher output current ripples, slow step response, no overload capability and no reverse current acceptance have made the inevitable use of power conditioners in the fuel cell systems. Currently there are no standards to standardize the output voltage of the fuel cells, hence the available fuel cells have an output voltage range of 24-150 V_{DC}.

The fuel cell voltage can be directly converted to AC by using single stage DC/AC inverter topology or multistage DC/DC converter cascaded with DC/AC inverter topology. The cost, efficiency, galvanic isolation, ripple level and reliability are the main factors to decide the topology to be used in the fuel cell system. The efficiency of the system mainly depends on the conduction and switching losses. The conduction losses can be reduced by selecting the topology with reduced number of components with appropriate range and switching losses can be minimized by soft switching techniques such as zero voltage switching (ZVS) or zero current switching (ZCS) techniques. Soft switching techniques reduce the losses about 20-30 % over the hard switching of the devices (16).

Hence a trade off between single stage or multistage power conditioning should be made as per the points listed below.

Single stage power converters:

1. It directly converts DC to AC, component count is low and hence losses are low.
2. But it requires high cost line frequency transformers to step up the voltage to the required level (17).
3. Low frequency ripples are high and hence the bulky passive components are required.
4. Efficiency is higher due to reduced losses.
5. Suitable for low and medium power applications.

Multistage power converters:

1. It has a DC-DC boost converter as a preceding stage to the DC-AC inverter, which increases the components count and resulting losses.

2. The DC-DC converter topology can be chosen with compact, low cost high frequency transformer which avoids high cost bulky, line frequency transformer as in the case of single stage converters.

3. High frequency ripples make the smaller passive components.

4. Efficiency is slightly lower than that of single stage converters due to more number of components.

5. Suitable for medium and high power applications.

6. The single stage and multistage power conditioning systems are shown in the figure 12.

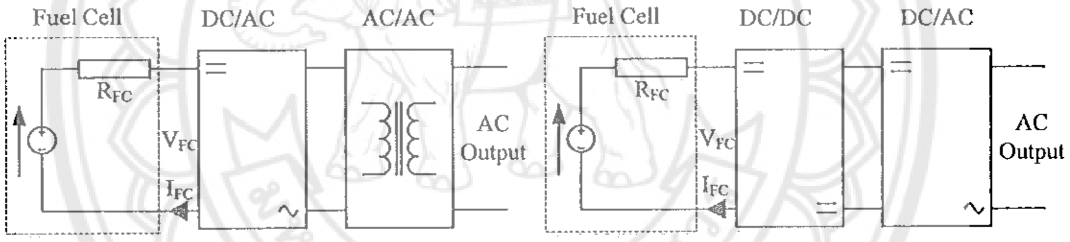

(a) Single stage DC/AC conversion

(b) Multistage DC/DC and DC/AC conversion

Figure 12 Fuel cell power conditioning systems

Compared to the single stage, multistage power conditioning systems are suited for fuel cell systems due to the various reasons listed earlier in this section. In case of multistage systems, the first stage after the fuel cell comes the DC-DC conversion stage. There are many topologies proposed in the literature which are mainly classified as isolated and non-isolated converter topologies. The simple, conventional non-isolated converter topology shown in figure 13a has higher efficiency (16) than that of others due to the reduced number of components. But if the voltage conversion ratio is higher the non isolated boost converter topology is not suited in protection view point. In the case of fuel cell power conditioning as the fuel cells generally produce low voltages, the voltage conversion ratio will be higher typically around 10 in this study, hence isolated converter topologies are preferred.

In the case of isolated converter topologies, the push-pull converter as shown in figure 13b has reduced losses as only one switch conducts at any point of time, but the possibility of transformer saturation is more in this case as the transformer used should be a center-tapped one, in which the two windings are not symmetrically wound always. This non identical winding may result in the failure of the converter. These push pull converters are suitable for low and medium power applications. The half bridge topology (11, 18, 19) shown in figure 13c is suitable for high power applications, but the voltage and current stress of the switches are more and needs high value of capacitors to avoid the transformer saturation or higher transformer ratio is needed (16) which increases the cost of the converter. The full bridge topology shown in the figure 13d has more number of components but the voltage and current stresses are less as two switches will be conducting at any point of time, hence reduced ratings of the switches can be used compared to the other topologies. Here in the full bridge topology shown in figure 13d, the influence of transformer leakage inductance with the output rectifier is problematic and the maximum switching frequency is limited due to the energy lost in the transformer leakage inductance and undesirable peak diode reverse recovery current. The transformer leakage inductance comes in series with the filter inductance added at the output of the secondary converter in the topology shown in figure 14. In this case the energy stored in the leakage inductance in series with the filter inductance will be recovered and transferred to the load in lossless manner. Hence the switching frequency in this topology can be further increased compared to other topology shown in figure 13d. In this full bridge topology A, the zero voltage switching can be ensured only when the device is turned on while the anti parallel diode is conducting. Moreover the output current ripple is more in the output filter capacitor. This topology naturally handles the diode recovery process. When these diodes are replaced with active switches as proposed full bridge topology B shown in figure 15, the converter is simple with PWM control to generate square waves that are phase shifted to control the direction and amount of power transfer by phase shift modulation. As this topology B consists of active bridges in both input and output bridges, this is called as Dual Active Bridge (DAB). The full bridge topology proposed in (5) though has more number of components, it has the advantages like reduced device current ratings, transformer ratio and also the voltage and current stress levels are lower when compared with other topologies (20–22). This topology has many other advantages such as inherent Zero Voltage Switching (ZVS), high power density, high efficiency, bidirectional capability and galvanic isolation. Moreover the full-bridge converters have small input-output current, voltage ripples and hence the full-bridge topology is a favorite topology for zero voltage switching (ZVS) (23). Due to these advantages DAB converter topology has been selected for fuel cell application as DC-DC boost converter in this study. However best suited nonlinear control methods like flatness based, are to be implemented for stable and robust operation of such systems (24). The soft switching range of these converters can be increased by increasing the leakage inductance and the phase shift to the highest possible value and the full load efficiency can be increased by choosing small value of phase shift to ensure the ZVS (25).

In the case of bidirectional power flow there exists DC bias currents due to unequal voltage-time area on the ac signal produced at primary and secondary of the transformer. This is due to the inevitable non-identical delays in the turn on and turn off times of the switching devices which causes the DC bias currents in the transformer. This may lead to saturation of the transformer producing high current pulses resulting to additional current stress, reducing converter efficiency and in turn may damage the converter too(26). These full bridge converters can be configured as interleaved full bridge DC-DC converter to have advantage with low input ripple current to meet the fuel cell demands. Paralleling the inputs shares the current and power equally by reducing the current stress and cascading the outputs reduces the voltage stress of the components. This also increases the ripple frequencies there by reducing the size of the passive components (27). Hence dual active bridge is one of the best configurations for fuel cell power conditioning applications.

Dual Active Bridge

The dual active bridge, the most promising topology with higher efficiency and reduced converter size is basically a bidirectional DC-DC Converter. It consists two full bridges with all active switches and a high frequency transformer. An external inductor

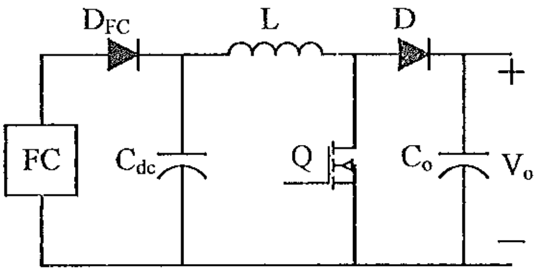

(a) Non-isolated conventional boost converter

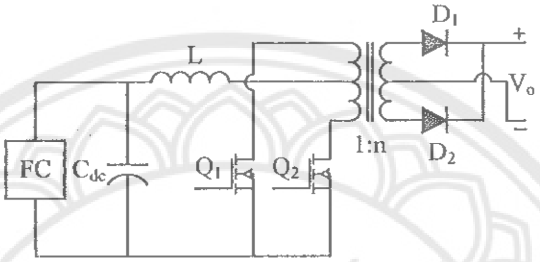

(b) Isolated push-pull converter

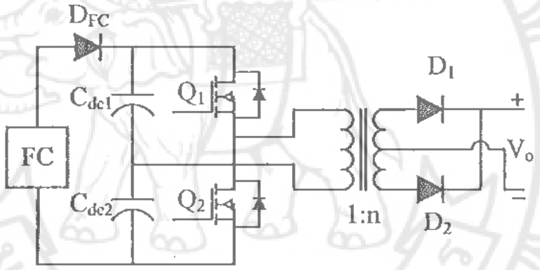

(c) Isolated half bridge converter

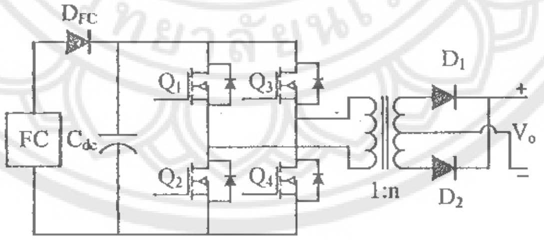

(d) Isolated full bridge converter

Figure 13 Isolated and non-isolated converter topologies

is connected to the transformer to store and transfer the energy to the gird or load.The phase shift between the two bridges control the power transfer and the power flows from the leading bridge to the lagging bridge. Hence by simply changing the value and sign of the phase shift between the gating signals, the amount and direction of power transfer

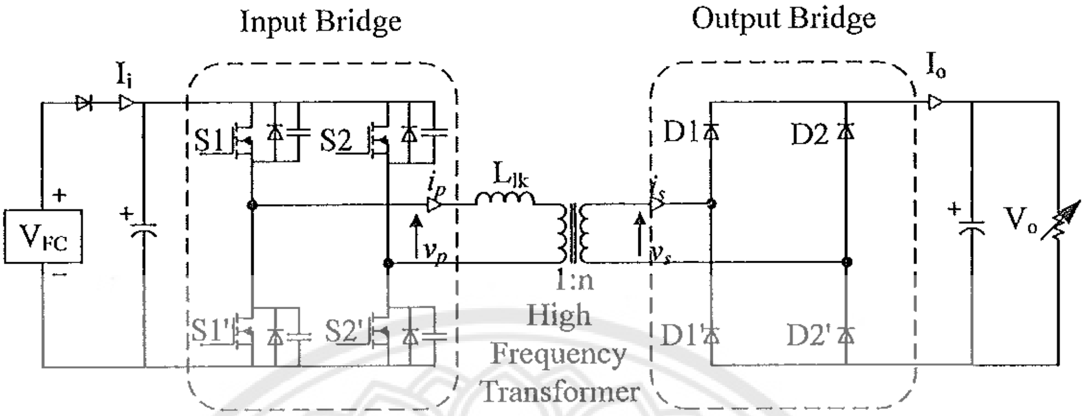

Figure 14 Isolated full bridge topology A

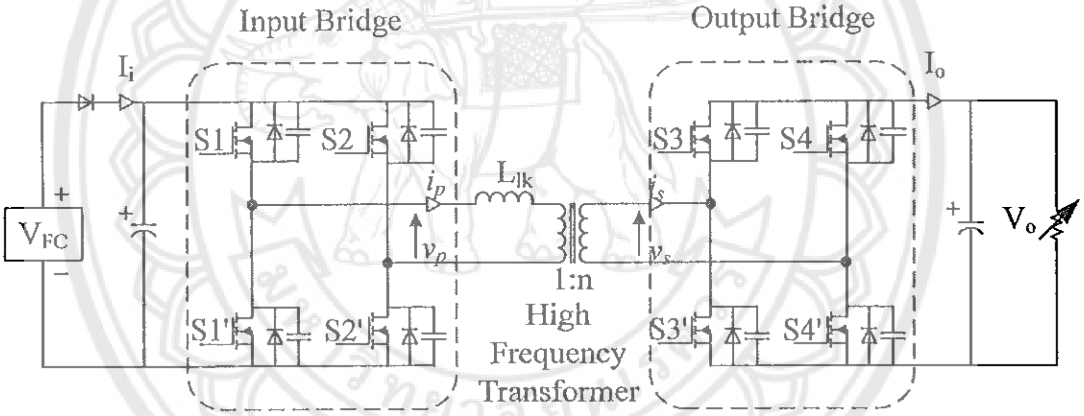

Figure 15 Isolated full bridge topology B

can be controlled. By analyzing the current and voltage waveforms, the region of zero voltage switching can be identified, which will enable the anti parallel diode to conduct at the time of turning ON of the switches. An equivalent topology referring to primary is shown in the figure 16. The various waveforms in the operation of the DAB are as shown in the figures 17 - 19 for different primary referred voltage transfer ratio *d*.

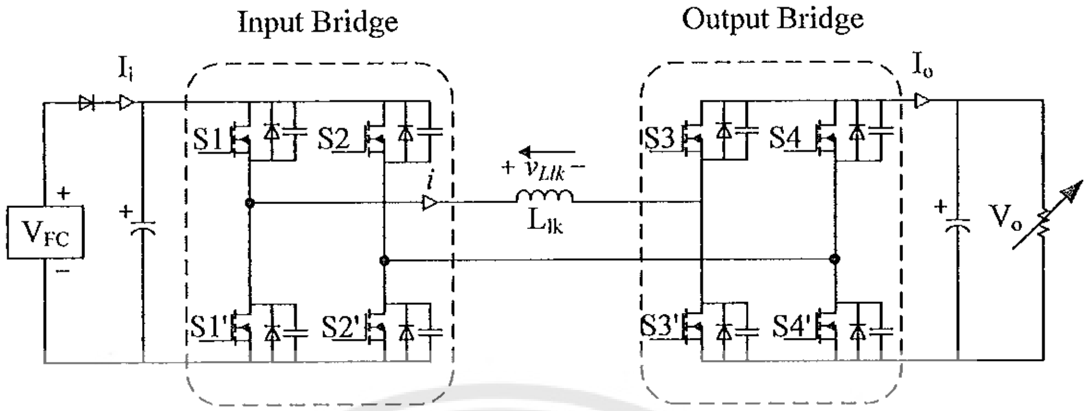

Figure 16 Primary referred equivalent circuit of topology B

Power flow calculation in Dual Active Bridge

The power flow calculation of the DAB as mentioned in (5) is described in this section. For the derivation the topology shown in figure 15 and the graph shown in figure 19 are considered. Let $i_p(\theta)$, V_{FC}, V'_{dc} be the current flown in the input side bridge of DAB, the fuel cell voltage and the primary referred output voltage in the DAB respectively. There are three different modes of operations within a period of π. Let the modes be Mode 1, Mode 2 and Mode 3, where Mode 1 is from 0 to x, Mode 2 is from x to ϕ and Mode 3 from ϕ to π as in figure 19

In the modes 1 and 2 the expression of the current $i_p(\theta)$ is the same and is given by

$$i_p(\theta) = i_p(0) + \frac{V_{FC} + V'_{dc}}{\omega L_{lk}}\theta \tag{2.6}$$

In the mode 3 from ϕ to π the current expression is given by

$$i_p(\theta) = i_p(\phi) + \frac{V_{FC} - V'_{dc}}{\omega L_{lk}}(\theta - \phi) \tag{2.7}$$

At $\omega t = \phi$; $i_p(\theta) = i_p(\phi)$ and the equation 2.6 gives

$$i_p(\phi) = i_p(0) + \frac{V_{FC} + V'_{dc}}{\omega L_{lk}}\phi \tag{2.8}$$

At $\omega t = \pi$; $i_p(\theta) = i_p(\pi)$ and from the equation 2.7

$$i_p(\pi) = i_p(\phi) + \frac{V_{FC} - V'_{dc}}{\omega L_{lk}}(\pi - \phi) \tag{2.9}$$

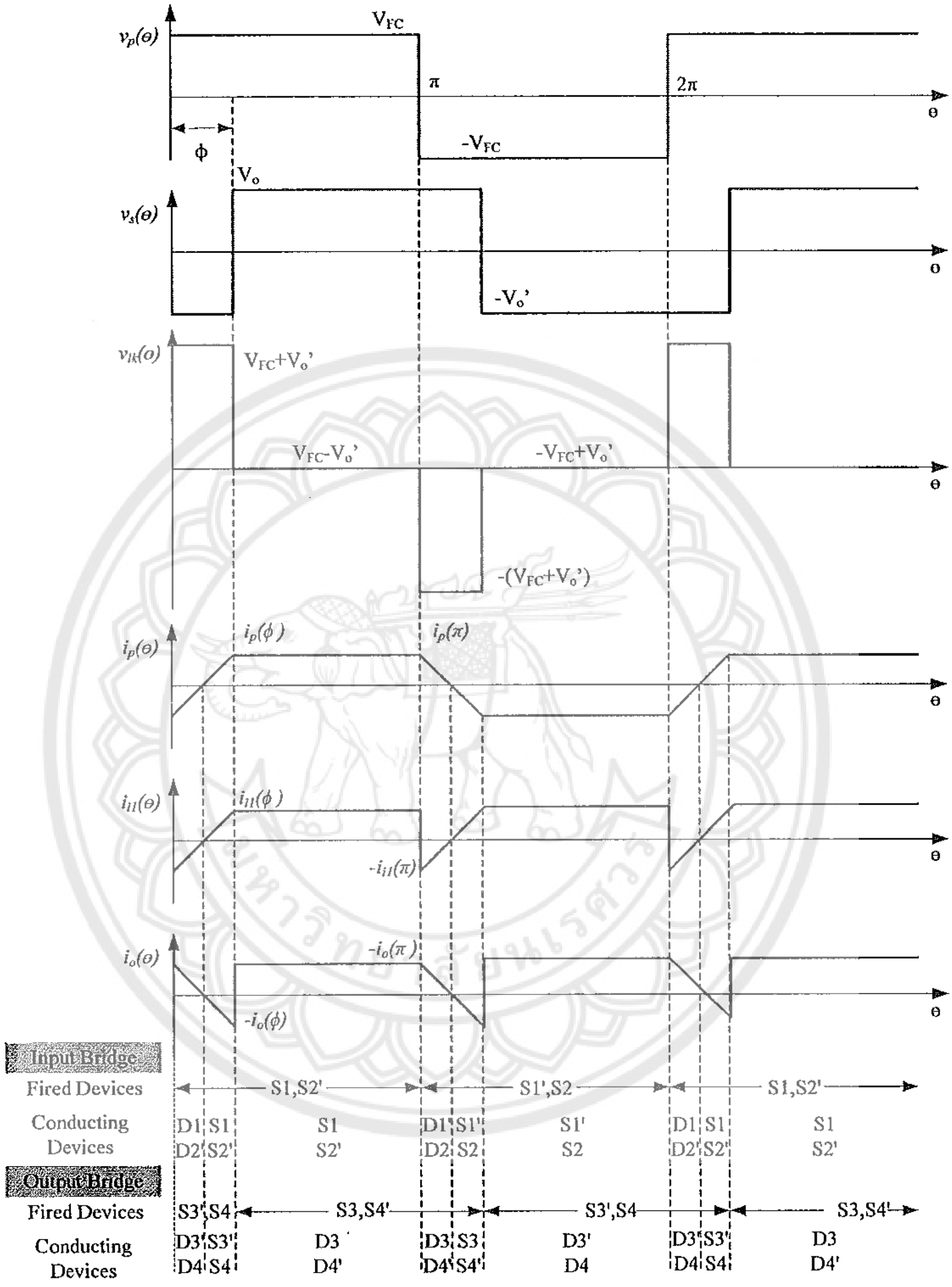

Figure 17 Voltage and current waveforms of DAB at $d = 1$

Due to the symmetry of the waveform $i_p(\pi) = -i_p(0)$ which gives

$$i_p(0) = -i_p(\pi) = -i_p(\phi) - \frac{V_{FC} - V'_{dc}}{\omega L_{lk}}(\pi - \phi) \tag{2.10}$$

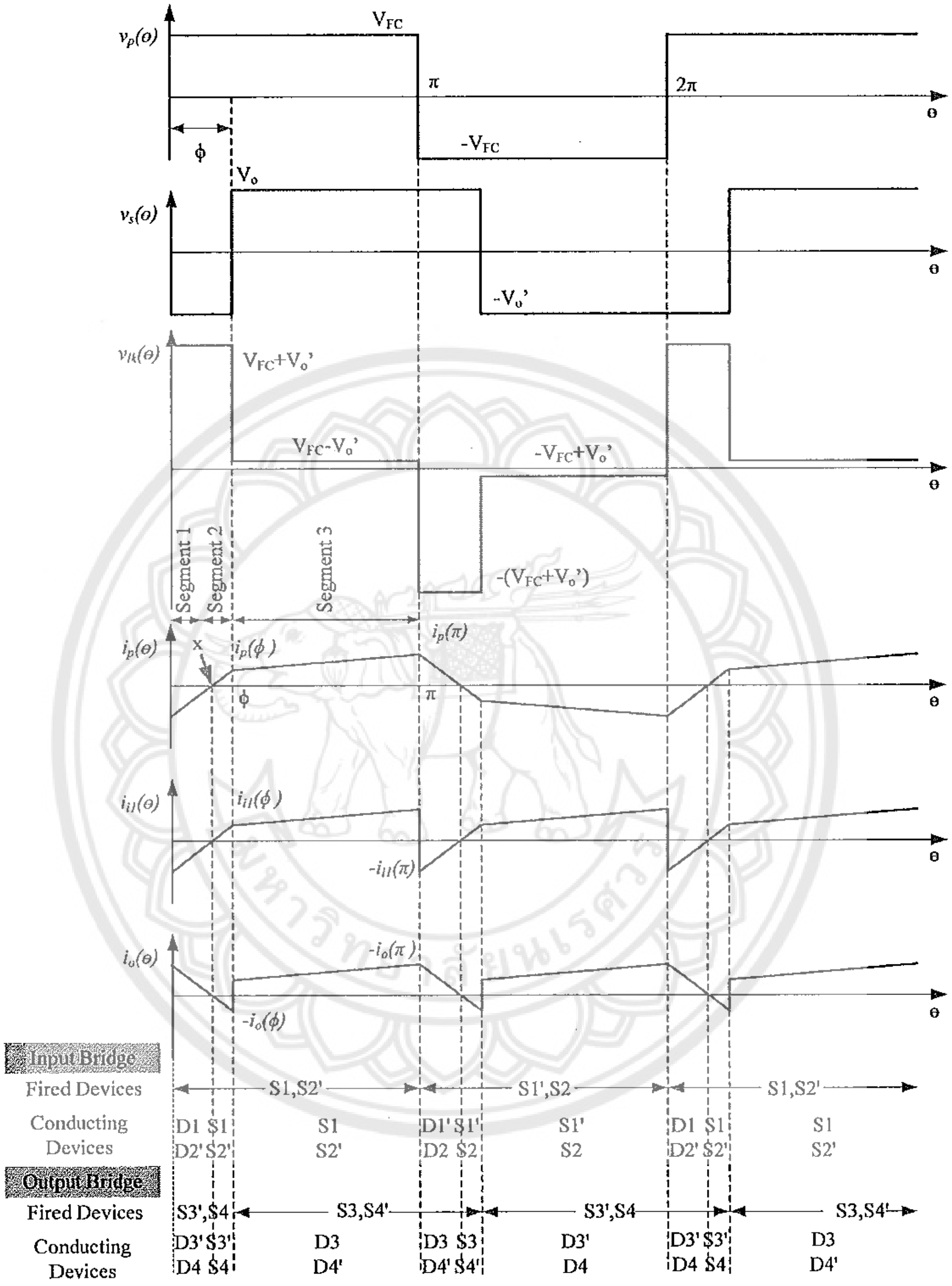

Figure 18 Voltage and current waveforms of DAB at $d > 1$

Substituting equation 2.10 in 2.8 we get

$$i_p(\phi) = -i_p(\phi) - \frac{V_{FC} - V_{dc}'}{\omega L_{lk}}(\pi - \phi) + \frac{V_{FC} + V_{dc}'}{\omega L_{lk}}\phi \qquad (2.11)$$

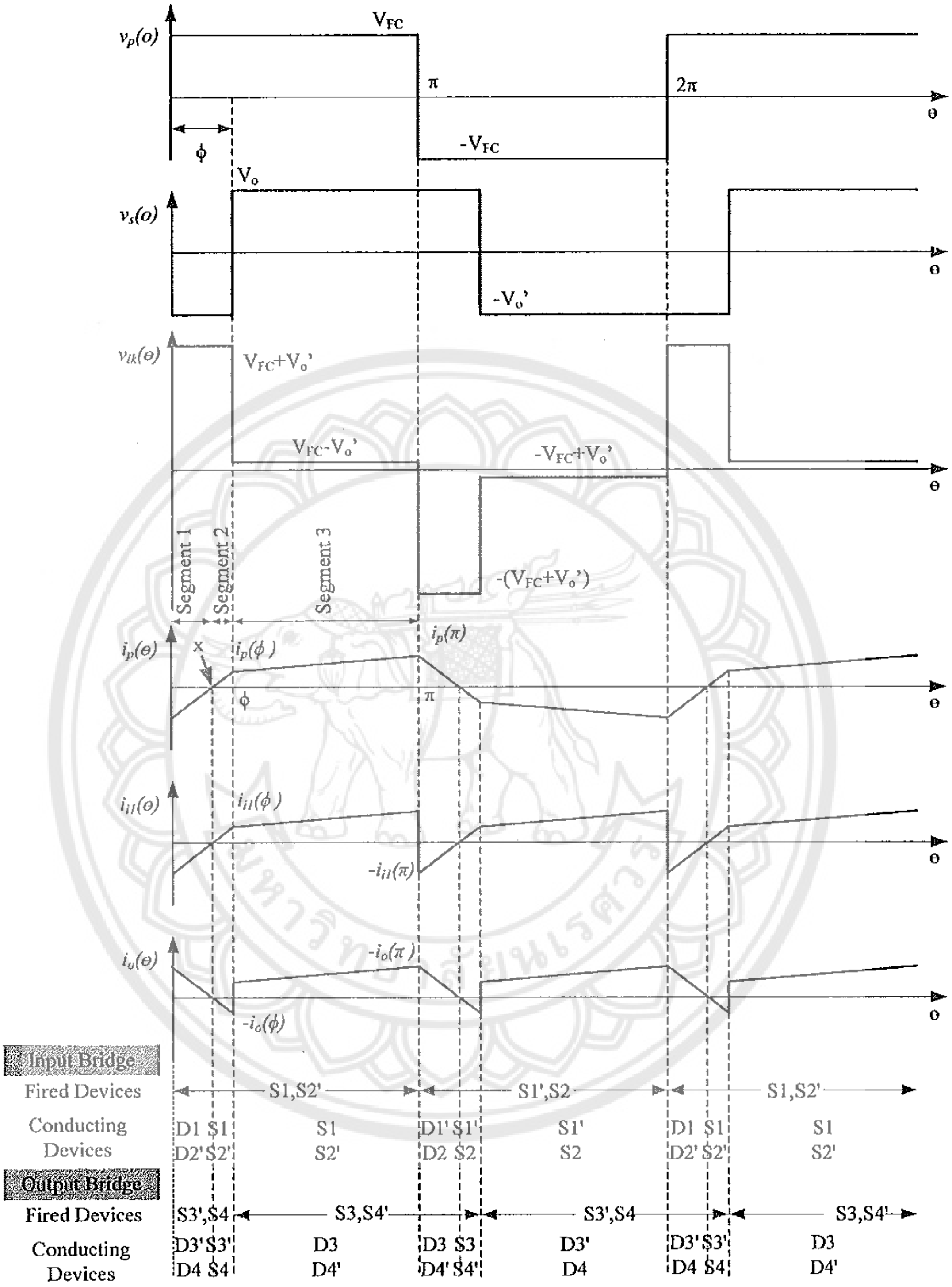

Figure 19 Voltage and current waveforms of DAB at $d < 1$

Let $d = \frac{V'_{dc}}{V_{FC}}$ which gives

$$2i_p(\phi) = \frac{V_{FC}}{\omega L_{lk}}[-(1-d)(\pi-\phi)+(1+d)\phi]$$

$$2i_p(\phi) = \frac{V_{FC}}{\omega L_{lk}}[-\pi + \phi + d\pi - d\phi + \phi + d\phi]$$

$$2i_p(\phi) = \frac{V_{FC}}{\omega L_{lk}}[2\phi - \pi + d\pi]$$

Thus the expression of the current at $\theta = \phi$ is given by

$$i_p(\phi) = \frac{V_{FC}}{\omega L_{lk}}\left[\phi - \frac{\pi(1-d)}{2}\right] \tag{2.12}$$

Substituting equation 2.12 in 2.8 we get,

$$\frac{V_{FC}}{\omega L_{lk}}\left[\phi - \frac{\pi(1-d)}{2}\right] = i_p(0) + \frac{V_{FC}+V'_{dc}}{\omega L_{lk}}\phi$$

$$i_p(0) = \frac{V_{FC}}{\omega L_{lk}}\left[\phi - \frac{\pi(1-d)}{2}\right] - \frac{V_{FC}+V'_{dc}}{\omega L_{lk}}\phi$$

$$i_p(0) = \frac{V_{FC}}{\omega L_{lk}}\left[\phi - \frac{\pi(1-d)}{2}\right] - \frac{V_{FC}(1+d)}{\omega L_{lk}}\phi$$

$$i_p(0) = \frac{V_{FC}}{\omega L_{lk}}\left[\phi - \frac{\pi(1-d)}{2} - (1+d)\phi\right]$$

$$i_p(0) = \frac{V_{FC}}{\omega L_{lk}}\left[\phi - \frac{\pi(1-d)}{2} - \phi - d\phi\right]$$

Thus the expression of the current at $\theta = 0$ is given by

$$i_p(0) = -\frac{V_{FC}}{\omega L_{lk}}\left[d\phi + \frac{\pi(1-d)}{2}\right] \tag{2.13}$$

In the modes 1 and 2 the current in the circuit increases with a slope m given by $m = \frac{V_{FC}+V'_{dc}}{\omega L_{lk}}$. Thus by the equation of a straight line $y = mx + c$ we get, [at x the y intersect is zero]

$$0 = \left[\frac{V_{FC}+V'_{dc}}{\omega L_{lk}}\right]x + \left[-\frac{V_{FC}}{\omega L_{lk}}\left[d\phi + \frac{\pi(1-d)}{2}\right]\right]$$

$$0 = \left[\frac{V_{FC}(1+d)}{\omega L_{lk}}\right]x + \left[-\frac{V_{FC}}{\omega L_{lk}}\left[d\phi + \frac{\pi(1-d)}{2}\right]\right]$$

$$0 = (1+d)x - \left[d\phi + \frac{\pi(1-d)}{2}\right]$$

$$x = \frac{\left[d\phi + \frac{\pi(1-d)}{2}\right]}{(1+d)}$$

$$x = \frac{2d\phi + \pi(1-d)}{2(1+d)} \tag{2.14}$$

Let us consider three areas under the curve A_1, A_2 and A_3 from 0 to π. The average area is given by

$$A_{ave} = \frac{A_2 + A_3 - A_1}{\pi}$$

where

A_1 is the area under the curve between 0 to x

A_2 is the area under the curve between x to ϕ

A_3 is the area under the curve between ϕ to π

A_1 is given by

$$A_1 = \frac{1}{2}\frac{V_{FC}}{\omega L_{lk}}\left[d\phi + \frac{\pi(1-d)}{2}\right]\left[\frac{2d\phi + \pi(1-d)}{2(1+d)}\right]$$

$$A_1 = \frac{1}{2}\frac{V_{FC}}{\omega L_{lk}}\frac{[2d\phi + \pi(1-d)][2d\phi + \pi(1-d)]}{4(1+d)}$$

$$A_1 = \frac{1}{8}\frac{V_{FC}}{(1+d)\omega L_{lk}}\left[4d^2\phi^2 + \pi^2(1-d)^2 + 4d\phi\pi(1-d)\right] \tag{2.15}$$

A_2 is given by

$$A_2 = \frac{1}{2}\left[\frac{V_{FC}}{\omega L_{lk}}(\phi - \frac{\pi(1-d)}{2})\right]\left[\phi - \frac{2d\phi + \pi(1-d)}{2(1+d)}\right]$$

$$A_2 = \frac{V_{FC}}{2\omega L_{lk}}\left[\frac{2\phi - \pi(1-d)}{2}\right]\left[\frac{2(1+d)\phi - 2d\phi - \pi(1-d)}{2(1+d)}\right]$$

$$A_2 = \frac{V_{FC}}{8\omega L_{lk}(1+d)}[2\phi - \pi(1-d)][2(1+d)\phi - 2d\phi - \pi(1-d)]$$

$$A_2 = \frac{V_{FC}}{8\omega L_{lk}(1+d)}[2\phi - \pi(1-d)][2\phi + 2d\phi - 2d\phi - \pi(1-d)]$$

$$A_2 = \frac{V_{FC}}{8\omega L_{lk}(1+d)}\left[4\phi^2 + \pi^2(1-d)^2 - 4\pi\phi(1-d)\right] \tag{2.16}$$

A_3 is given by

$$A_3 = \frac{1}{2}\left[\frac{V_{FC}}{\omega L_{lk}}\left[d\phi + \frac{\pi(1-d)}{2} + \phi - \frac{\pi(1-d)}{2}\right]\right](\pi - \phi)$$

$$A_3 = \frac{V_{FC}}{2\omega L_{lk}}\left[\phi(1+d)(\pi-\phi)\right] \tag{2.17}$$

Now

$$\begin{aligned}
A_3 + A_2 - A_1 = {} & \frac{V_{FC}}{2\omega L_{lk}}\left[\phi(1+d)(\pi-\phi)\right] \\
& + \frac{V_{FC}}{8\omega L_{lk}(1+d)}\left[4\phi^2 + \pi^2(1-d)^2 - 4\pi\phi(1-d)\right] \\
& - \frac{V_{FC}}{8\omega L_{lk}(1+d)}\left[4d^2\phi^2 + \pi^2(1-d)^2 + 4d\pi\phi(1-d)\right]
\end{aligned}$$

$$\begin{aligned}
= {} & \frac{V_{FC}}{8\omega L_{lk}(1+d)}[4(1+d)(1+d)\phi(\pi-\phi) + 4\phi^2 + \pi^2(1-d)^2 - 4\pi\phi(1-d) \\
& - 4d^2\phi^2 - \pi^2(1-d)^2 - 4d\pi\phi(1-d)] \\
= {} & \frac{V_{FC}}{8\omega L_{lk}(1+d)}[4(1+d^2+2d)(\pi\phi-\phi^2) + 4\phi^2 - 4\pi\phi(1-d) - 4d^2\phi^2 \\
& - 4d\pi\phi(1-d)] \\
= {} & \frac{V_{FC}}{8\omega L_{lk}(1+d)}[4\pi\phi - 4\phi^2 + 4d^2\pi\phi - 4d^2\phi^2 + 8d\pi\phi - 8d\phi^2 + 4\phi^2 - 4\pi\phi \\
& + 4d\pi\phi - 4d^2\phi^2 - 4d\pi\phi + 4d^2\pi\phi] \\
= {} & \frac{V_{FC}}{8\omega L_{lk}(1+d)}\left[8d^2\pi\phi - 8d^2\phi^2 + 8d\pi\phi - 8d\phi^2\right] \\
= {} & \frac{8dV_{FC}}{8\omega L_{lk}(1+d)}\left[d\pi\phi - d\phi^2 + \pi\phi - \phi^2\right] \\
= {} & \frac{dV_{FC}}{\omega L_{lk}(1+d)}\left[\pi\phi(1+d) - \phi^2(1+d)\right] \\
= {} & \frac{dV_{FC}}{\omega L_{lk}}\left[\pi\phi - \phi^2\right] \\
A_3 + A_2 - A_1 = {} & \frac{V_{FC}d\phi}{\omega L_{lk}}\left[\pi - \phi\right] \\
A_{ave} = {} & \frac{A_3 + A_2 - A_1}{\pi}
\end{aligned}$$

Thus the average current flown from the fuel cell is given by

$$I_{FC_{ave}} = A_{ave} = \frac{V_{FC} d\phi}{\pi \omega L_{lk}} [\pi - \phi] \tag{2.18}$$

This average current model of the DAB is used in the MATLAB®simulation. The average power transferred from the fuel cell is given by

$$\begin{aligned} P_{FC_{ave}} = V_{FC} I_{FC_{ave}} &= \frac{V_{FC}^2 d\phi}{\pi \omega L_{lk}} [\pi - \phi] \\ &= \frac{V_{FC}^2}{\omega L_{lk}} d\phi \left[1 - \frac{\phi}{\pi}\right] \end{aligned}$$

Primary RMS current of the transformer

The RMS value of the current at the primary of the transformer can be calculated as described here. The regions in the primary current waveform $i_p(\theta)$ shown in figure 19 can be divided in to three segments within the period 0 to π. Segment 1 is the period between 0 to x, segment 2 is between x to ϕ and segment 3 is between ϕ to π.

For a periodic waveform composed of n piece-wise segments, the RMS value is given by,

$$RMS = \sqrt{\sum_{k=1}^{n} D_k u_k}$$

where D_k is the duty cycle of the segment k and u_k is the contribution of the segment k. The current contributing the segment 1 is given by

$$i_p(0) = -\frac{V_{FC}}{\omega L_{lk}} \left[d\phi + \frac{\pi(1-d)}{2}\right].$$

The current contributing the segment 2 is given by

$$i_p(\phi) = \frac{V_{FC}}{\omega L_{lk}} \left[\phi - \frac{\pi(1-d)}{2}\right]$$

The current contributing the segment 3 is given by

$$i_p(\phi) = \frac{V_{FC}}{\omega L_{lk}} \left[d\phi + \frac{\pi(1-d)}{2}\right]$$

The duty cycle of the segment 1 is given by

$$D_1 = \frac{2d\phi + \pi(1-d)}{2\pi(1+d)}$$

The duty cycle of the segment 2 is given by

$$D_2 = \frac{2\phi - \pi(1-d)}{2\pi(1+d)}$$

The duty cycle of the segment 3 is given by

$$D_3 = \frac{\pi - \phi}{\pi}$$

The contribution of the current in the triangular segment 1 is given by

$$u_1 = \frac{1}{3} i_p(0)^2$$

$$u_1 = \frac{V_{FC}^2}{3(\omega L_{lk})^2} \left[d\phi + \frac{\pi(1-d)}{2} \right]^2$$

Let

$$a = d\phi + \frac{\pi(1-d)}{2}$$

hence

$$u_1 = \frac{V_{FC}^2}{3(\omega L_{lk})^2} a^2$$

The contribution of the current in the triangular segment 2 is given by

$$u_2 = \frac{1}{3} i_p(\phi)^2$$

$$u_2 = \frac{V_{FC}^2}{3(\omega L_{lk})^2} \left[\phi - \frac{\pi(1-d)}{2} \right]^2$$

Let

$$b = \phi - \frac{\pi(1-d)}{2}$$

hence

$$u_2 = \frac{V_{FC}^2}{3(\omega L_{lk})^2} b^2$$

The contribution of the current in trapezoidal segment 3 is given by

$$u_3 = \frac{1}{3}[i_p(0)^2 + i_p(0)i_p(\phi) + i_p(\phi)^2]$$

$$u_3 = \phi^2[1 + d + d^2] - \frac{\pi\phi(1-d)^2}{2}$$

Thus the RMS value of the transformer primary current is given by

$$i_{p_{rms}} = \sqrt{D_1 u_1 + D_2 u_2 + D_3 u_3}$$

$$i_{p_{rms}} = \frac{V_{FC}}{\omega L_{lk}} \sqrt{\frac{[a^2(3\pi + \pi d - 2\phi) + b^2(\pi + 3\pi d - 2\phi d) + 2ab(1+d)(\pi - \phi)]}{6\pi(1+d)}}$$

where

$$a = d\phi + \frac{\pi(1-d)}{2}$$

and

$$b = \phi - \frac{\pi(1-d)}{2}$$

Hard switching and soft switching of converters

The switching devices in the converters face hard switching conditions when the switches are forced to switch ON before they are not completely turned OFF (zero current state) or when they are forced to switch OFF before they are completely turned ON (zero voltage state). In either case there will be regions in which voltage across the device falls and current through the device rises (during turn ON) or the current through the device falls and voltage across rises (during turn OFF), which gives rise to switching power losses . This is called hard switching. Referring to the circuit in figure 20, hard switching is illustrated as in figure 21, which shows the power loss in case of hard switching. In high frequency switching circuits this results in high power switching losses. Hence this should be avoided by soft switching of the switches in the converter where the switches are turned ON when they are completely OFF and turned OFF when they are completely turned ON. This soft switching, termed as Zero Voltage Switching (ZVS) and Zero Current Switching (ZCS) are inherent in the case of dual active bridge,

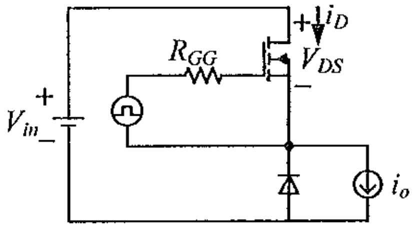

Figure 20 Hard switching of a circuit

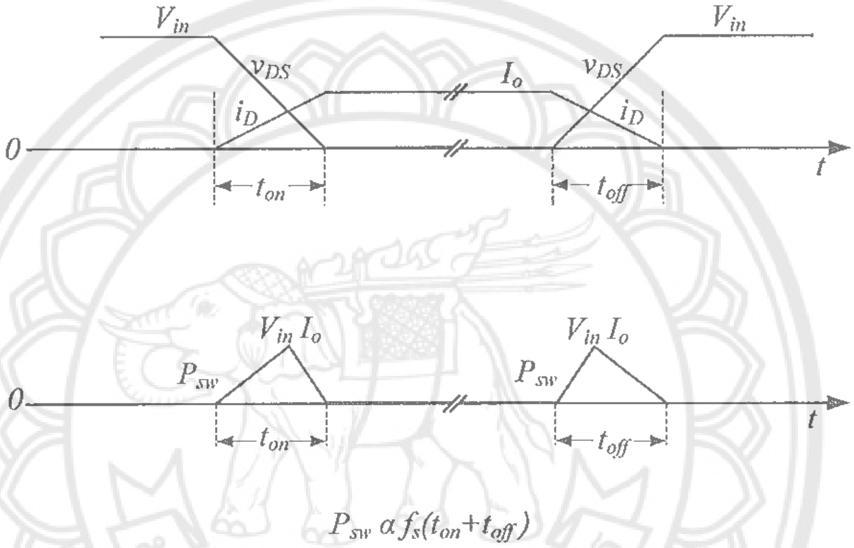

Figure 21 Hard switching waveforms

(a) Switch OFF ready for ZVS ON **(b) Switch ON ready for ZVS OFF**

Figure 22 Soft switching of switches

which reduces the high frequency switching losses. The soft switching nature of the DAB is illustrated in the figure 23.

The condition of switch in the case of soft switching is shown in the figure 22 in which the switch in figure 22a is OFF and the antiparallel diode across it conducts, making the voltage across the OFF switch to be zero, which is now ready for ZVS ON.

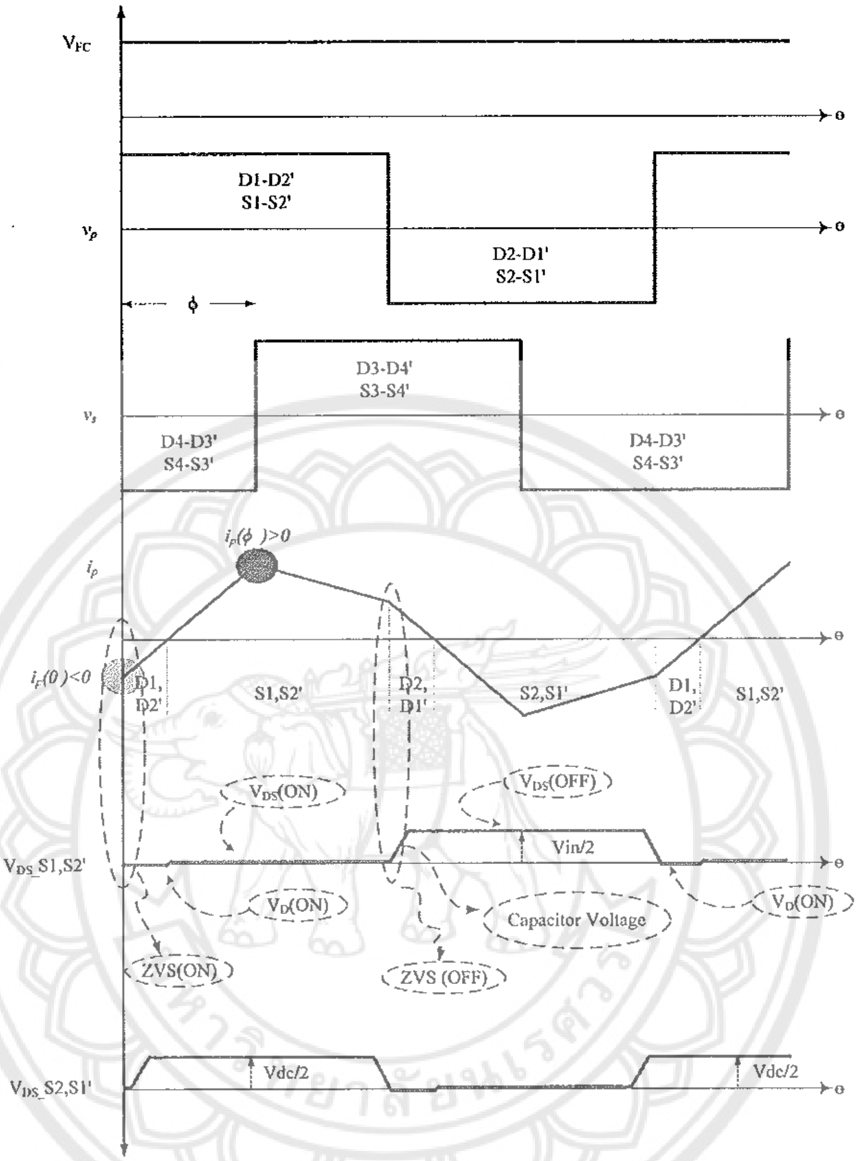

Figure 23 Soft switching of input side bridge of DAB

Similarly the condition of the switch in figure 22b is ON, the ON state voltage of the switch appears across the capacitor, which holds it during the time of ZVS OFF, as ON state voltage of the switch is almost zero.

In the case of dual active bridge converters the boundary conditions for ZVS are given to be $i_p(0) \leq 0$ for input bridge and $i_p(\phi) \geq 0$ for output bridge. Applying these conditions with the respective current expression, the figure 24 shows the regions of soft switching with the constraints on power P, phase shift ϕ and the primary referred voltage transfer ratio d. These boundary conditions are considered in the designing of DAB to

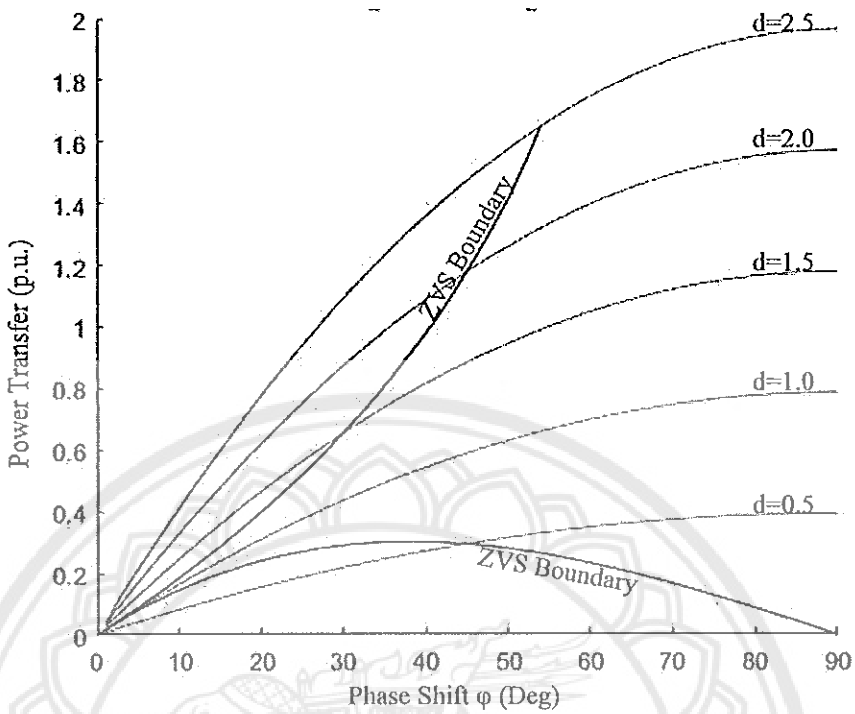

Figure 24 ZVS boundaries

have soft switching during operation.

Single phase voltage source inverter

The dual active bridge described in the previous section converts low voltage DC output from the fuel cell to a high voltage DC in order to convert it to AC as a part of multistage power converter topology. A switched mode DC-AC inverter is considered for grid connected fuel cell system in this study. The magnitude and the frequency of the sinusoidal AC output can be controlled in these inverters. The output of grid connected inverter should be matched with the magnitude, frequency and phase of the grid voltage, which is achievable in this switched mode inverter. These switched mode inverters are broadly classified as Voltage Source Inverters (VSI) where the input DC source is a voltage source and Current Source Inverters (CSI) where the input DC source is a current source. As CSIs are generally required and used in very high power applications, in this study switched mode VSI is chosen to be used.

The VSIs are further classified into the following,

1. *Pulse width modulated inverters* : For constant DC input voltage, these inverters control the magnitude and frequency of the AC output voltage. This is achieved by applying pulse width modulated control signals to the switches in the inverter. There are different PWM techniques available to get the output much closer to sine wave. The sinusoidal PWM is used in this study.

2. *Square wave inverters* : In these inverters the input DC voltage is controlled to control the magnitude of the inverter AC output, hence the inverter controls only the frequency of the AC output. These inveters can produce only square wave AC output.

In general inverters should be a four quadrant inverter, able to operate in both inverter mode and rectifier mode of operations. The inverter current may lead or lag the output voltage depending on the nature of the load. Hence in such cases the power flow may be either from DC to AC or AC to DC. Single phase full bridge inverters as shown in figure 25 are capable of operating in all four quadrants.

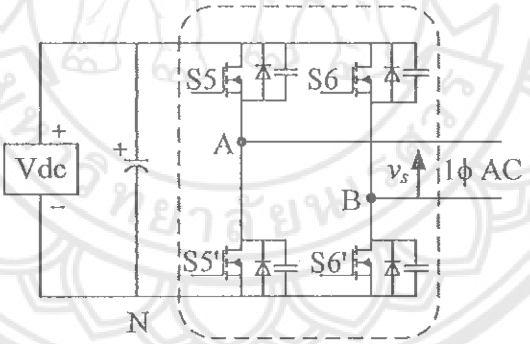

Figure 25 Single phase full bridge inverter

Pulse Width Modulation Techniques

PWM techniques are used in the inverters to produce sinusoidal AC output, with controlled magnitude and frequency. The sinusoidal wave generated is much closer to an ideal sine wave. To produce such control signals, a sinusoidal control signal at the desired frequency is compared with a triangular signal. The desired frequency of the control signal is the fundamental frequency and the frequency of the triangular wave is the switching frequency of the switches in the inverter. The magnitude of the triangular wave is kept constant.

Definitions of the terms used in PWM technique:

1. v_{tri} : Triangular waveform often called as the carrier signal.

2. f_{sw} : Frequency of the triangular waveform, called as carrier frequency or switching frequency.

$v_{control}$: Sinusoidal control signal, often called as modulating signal whose amplitude controls the amplitude of the output voltage.

3. f_1 : Frequency of the sinusoidal signal, often called as modulating frequency ,which is the desired fundamental output frequency.

4. m_a : Amplitude modulation ratio is the ratio between the magnitude of the modulating signal and the magnitude of carrier signal which is given by

$$m_a = \frac{\hat{V}_{control}}{\hat{V}_{tri}}$$

where $\hat{V}_{control}$ is the peak magnitude of the control signal and $\hat{V}_{tri}$ is the amplitude of the triangular signal. The amplitude $\hat{V}_{tri}$ is generally kept constant.

5. m_f : Frequency modulation ratio is the ratio between frequency of the triangular signal and the sinusoidal signal. It is given by

$$m_f = \frac{f_{sw}}{f_1}$$

Bipolar PWM switching technique

In the case of bipolar switching techniques diagonally opposite switch pairs (S5,S6') and (S5',S6) are switched alternately. In such case of switching, when the pair (S5,S6') is turned ON the output of the inverter $v_s = V_{dc}$ whereas when the pair of switches (S6,S5') is turned ON the $v_s = -V_{dc}$. To generate such a switching pattern, a triangular wave v_{tri} with the selected switching frequency f_{sw} is compared with a sinusoidal wave $v_{control}$ of fundamental frequency f_1. When $v_{control} > v_{tri}$ the (S5,S6') pair is turned ON, and when the $v_{tri} > v_{control}$ the pair (S6,S5') is turned ON. This gives a non sinusoidal alternating voltage $v_s = \pm V_{dc}$ which contains voltage components at the harmonic frequencies of f_1. This can be filtered out to be a waveform much closer to a sine wave with proper filtering techniques. The generation of a bipolar PWM switching pattern and corresponding output v_s waveform are shown in the figure 26.

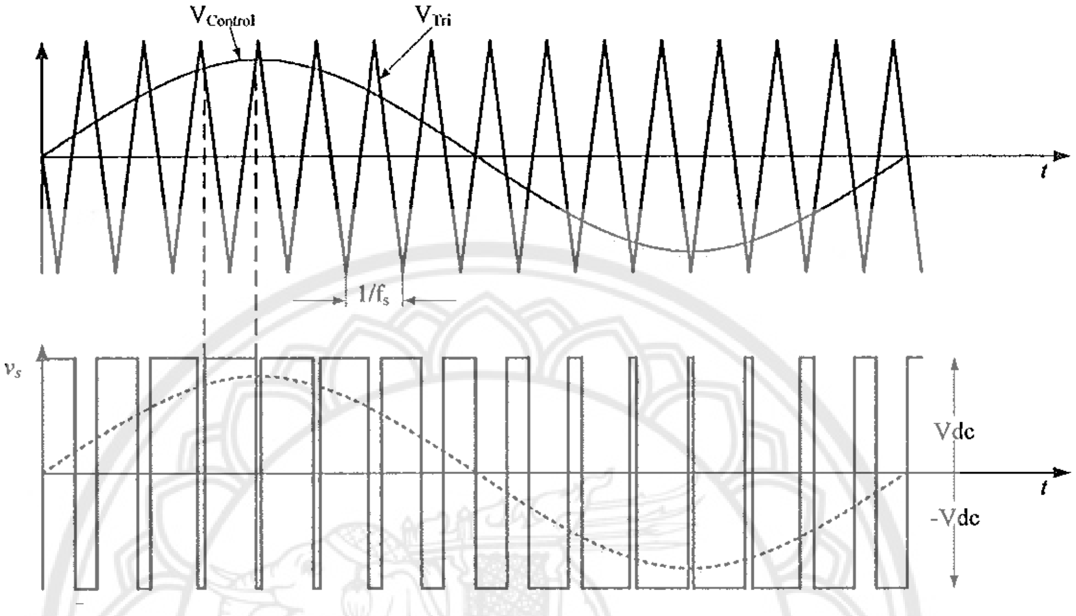

Figure 26 Bipolar PWM switching and corresponding output

Unipolar PWM switching technique

In unipolar PWM the switches in the legs of the full bridge are controlled separately. A single triangular carrier signal is compared with two sinusoidal control signals which are mutually out of phase to each other. The leg A is controlled by comparing with $v_{control}$ and leg B is controlled by comparing with $-v_{control}$. The generation of unipolar PWM signal are shown in figure 27. The following are the states of the switches, and the corresponding output voltages.

1. When switches S5 and S6' are ON : v_{AN} = V_{dc},v_{BN} = 0, v_s = V_{dc}
2. When switches S5' and S6 are ON : v_{AN} = 0,v_{BN} = V_{dc}, v_s = -V_{dc}
3. When switches S5 and S6 are ON : v_{AN} = V_{dc},v_{BN} = V_{dc}, v_s =0
4. When switches S5' and S6' are ON : v_{AN} = 0,v_{BN} =0, v_s = 0

When both the upper switches are ON, the output voltage is zero, the current circulates through one of the upper switches and the antiparallel diode across the other switch depending on the direction of the current. In such condition the input current from the fuel cell is zero as there is only the circulating current. Similarly, when both the lower switches are ON, output voltage is zero and the similar conditions exist. It can be observed that the pulsating AC output voltage changes between zero and $+V_{dc}$ or zero and $-V_{dc}$. Hence this scheme of PWM is called as unipolar where as in bipolar scheme the the output voltage changes between $+V_{dc}$ and $-V_{dc}$. This scheme changes the output voltage either between zero and $+V_{dc}$ or zero and $-V_{dc}$ twice in the same time

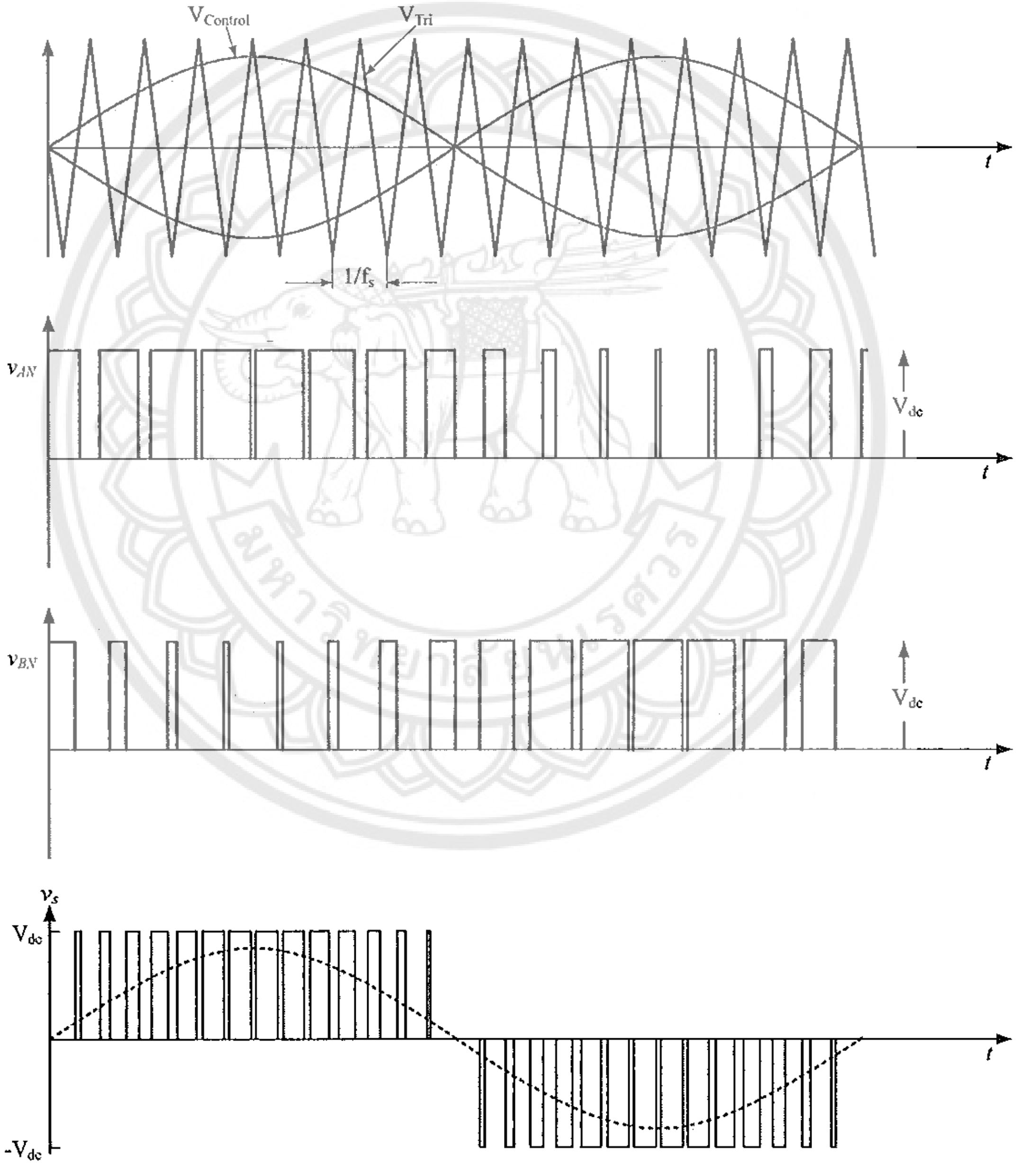

Figure 27 Unipolar PWM switching and corresponding output

period when bipolar scheme changes the output once between $+V_{dc}$ and $-V_{dc}$ or $-V_{dc}$ and $+V_{dc}$. Hence the unipolar scheme has the advantage of effectively doubling the switching frequency in the context of the harmonics content where as in bipolar scheme no such phenomenon occurs. It can be observed from the harmonic spectrum, that the voltage harmonics at the switching frequency is zero when the frequency modulation ratio is chosen to be even. The DC side current of the inverter with unipolar PWM has reduced ripples compared with bipolar PWM scheme. In unipolar scheme the output voltage switches between zero and $\pm V_{dc}$ which is V_{dc} whereas in bipolar scheme the voltage switches between $+V_{dc}$ and $-V_{dc}$ which is $2V_{dc}$. This reduced voltage jump in each switching reduces the current ripples at the DC side of the inverter. Hence an unipolar PWM scheme is implemented in this study to have reduced current ripples at the fuel cell side.

Grid connected inverters

Electrical grids are critical dynamic systems which are affected by loading and unloading of the system, harmonics in the currents, faults, mishandling of electrical equipment etc., The grid is also getting affected significantly by the frequent variations in the grid connected renewable energy sources due to their intermittent and fluctuating nature. Hence the grid variables are not constant all the times and need to be monitored and controlled continuously in order to have stability in the system. The grid connected inverters should be having interactive relationship with the grid to support the grid frequency and voltage. This implies that the grid stability and safety are seriously affected with the use of power converters, especially in the distributed energy systems based on renewable energy sources. Since this study focuses on such a fuel cell based renewable power system, the design of the inverter followed the standards (28) devised for single phase grid integration.

Grid synchronization using Phase-Locked Loop

There are different methods available to synchronize the inverter to the grid. PLL based synchronization is fast and precise compared to the others, hence in this study PLL based synchronization has been chosen. A PLL is a closed-loop system in which an internal oscillator is controlled to keep the time of some external periodical signal by using the feedback loop. If a synchronous controller rotating at the fundamental grid frequency is observed from a stationary reference, a relative difference is not expected to exist between the frequency of both the internal variables of the controller and the fundamental grid variables the effect of harmonics is neglected here. Therefore, the AC grid variables look like DC variables for a properly tuned synchronous controller. As a result, well-known DC controllers can be used to regulate AC magnitudes oscillating at the fundamental grid frequency, which makes the tuning process easier. Moreover, delays introduced by elements acting as the modulator of the power converter and sensors can be compensated by just advancing the phase-angle detected by the PLL. In addition, the PLL provides continuous information about the phase-angle and amplitude of the magnitude of interest, generally the fundamental grid voltage, which allows space vector based controllers and modulators to be implemented, even when working with single-phase signals. A basic PLL diagram is shown in the figure 28.

It contains

1. A *phase detector* (PD): This block generates an output signal proportional to the phase difference between the input signal, v, and the signal generated by the internal oscillator of the PLL, v'. Depending on the type of PD, high-frequency AC components appear together with the DC phase-angle difference signal.

2. A *loop filter* (LF): This block presents a low-pass filtering characteristic to attenuate the high-frequency AC components from the PD output. Typically, this block is constituted by a first-order low-pass filter or a PI controller.

3. A *voltage-controlled oscillator* (VCO): This block generates at its output an AC signal whose frequency is shifted with respect to a given central frequency, ω_c, as a function of the input voltage provided by the LF.

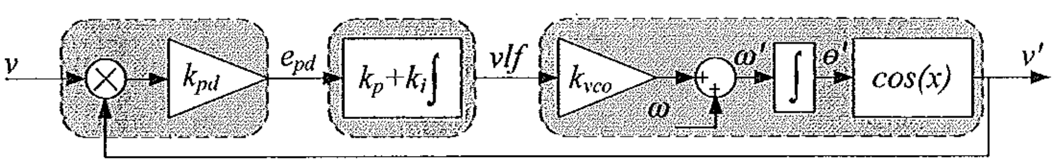

Figure 28 Basic structure of PLL

Basic equations of PLL

As shown in the figure 28, the phase detector is a simple multiplier, loop filter is a PI controller and VCO is a sinusoidal function supplied by a linear integrator.
If the input to the system is given by

$$v = Vsin(\theta) = Vsin(\omega t + \phi)$$

and the signal generated by the VCO is given by

$$v' = cos(\theta') = cos(\omega' t + \phi')$$

then the output of the phase detector can be return as

$$e_{pd} = Vk_{pd} sin(\omega t + \phi) cos(\omega' t + \phi')$$

$$e_{pd} = \frac{Vk_{pd}}{2}[sin((\omega - \omega')t + (\phi - \phi')) + sin((\omega + \omega')t + (\phi + \phi'))]$$

Since the output of the phase detector being a multiplier, contains both low frequency and high frequency components. But the loop filter being a low pass filter cancels out the high frequency components.
Hence

$$e_{pd} = \frac{Vk_{pd}}{2}[sin((\omega - \omega')t + (\phi - \phi'))]$$

If the VCO is well tuned to the input frequency so that $\omega = \omega'$ then the error term contains only DC quantity and is given by,

$$e_{pd} = \frac{Vk_{pd}}{2} sin(\phi - \phi')$$

The e_{pd} is a non linear quantity due to the sine function. But if the phase error is very small ($\phi \approx \phi'$) it can be linearized at that point. Hence at the localized operating point θ, $sin(\phi - \phi') = sin(\theta - \theta') \approx (\theta - \theta')$.
Hence once the PLL is locked, the linearized phase error is given by,

$$e_{pd} = \frac{Vk_{pd}}{2}(\theta - \theta')$$

Phase detection based on in-quadrature signals

Figure 29 shows a PD based on a of in-quadrature signals. The quadrature signal generator (QSG) is ideal, able to extract a set of in-quadrature signals without any delay at any frequency from a given distorted input signal.

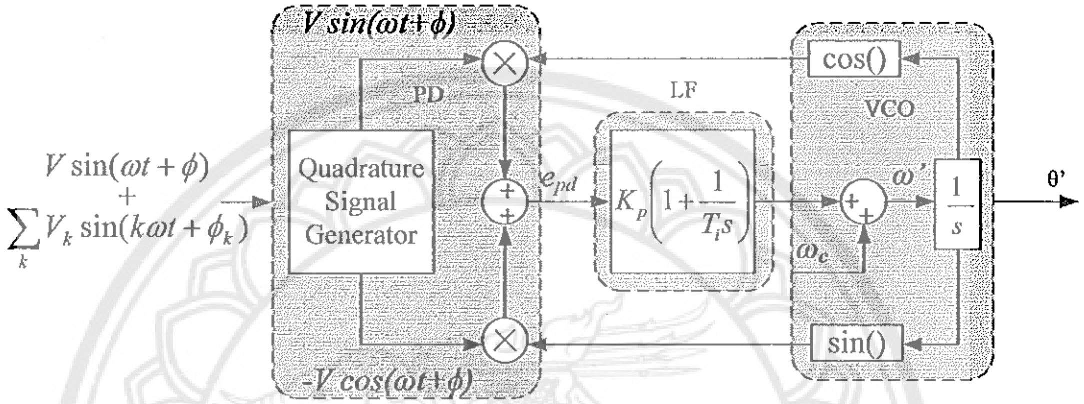

Figure 29 PLL with an ideal in-quadrature PD

The phase error with ideal in-quadrature PD is given by,

$$e_{pd} = V sin(\omega t+\phi)cos(\omega' t+\phi')V cos(\omega t+\phi)sin(\omega' t+\phi')$$

$$e_{pd} = V sin((\omega-\omega')t+(\phi-\phi'))$$

$$e_{pd} = V sin(\theta-\theta')$$

This shows, when the PLL is well synchronized, i.e. with $\omega = \omega'$, the in-quadrature PD does not generate any steady-state oscillatory term. From this expression, based on Park transformation figure 29 can be represented as in figure 30. Here the standard VCO is replaced with frequency/phase angle generator to generate phase angle for sinusoidal functions of Park transformation. This makes the phase detector as synchronized one.

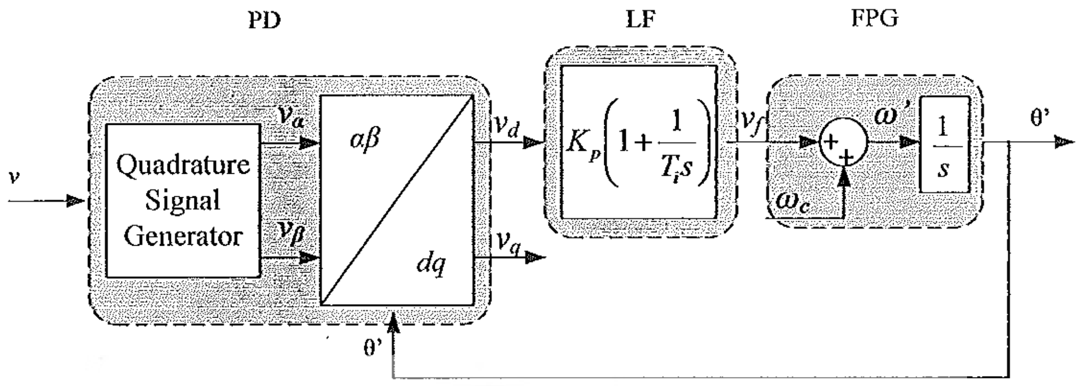

Figure 30 PD with the Park transformation

where the $\alpha\beta$ to dq transformation block is defined by the following matrix.

$$\begin{bmatrix} v_d \\ v_q \end{bmatrix} = \begin{bmatrix} cos(\theta') & sin(\theta') \\ -sin(\theta') & cos(\theta') \end{bmatrix} \begin{bmatrix} v_\alpha \\ v_\beta \end{bmatrix}$$

If the input of the PLL is given by $v = Vsin(\theta) = Vsin(\omega t + \phi)$, the output of the QSG is given by

$$v_{(\alpha\beta)} = \begin{bmatrix} v_\alpha \\ v_\beta \end{bmatrix} = V \begin{bmatrix} sin(\theta) \\ -cos(\theta) \end{bmatrix}$$

Substituting this will give

$$v_{(dq)} = \begin{bmatrix} v_d \\ v_q \end{bmatrix} = V \begin{bmatrix} sin(\theta - \theta') \\ -cos(\theta - \theta') \end{bmatrix}$$

This shows that the voltage in dq is free from oscillations. The vector interpretation of a single-phase system makes it possible the virtual current vectors to interact with the virtual grid voltage vector to control the active and reactive power delivered into a single-phase grid by a power converter. The loop filter *LF* can be connected to the v_q output as shown in the figure 31. Since the output θ' is 90° lagging the sinusoidal input voltage, it can be used for reactive power control.

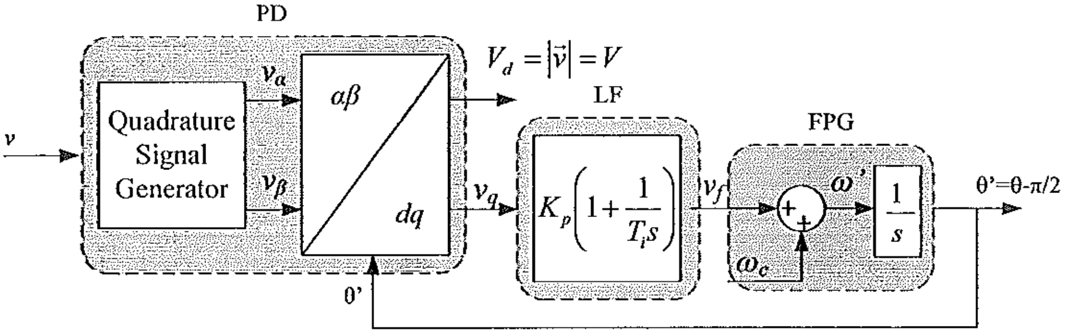

Figure 31 PLL with LF on *q* axis

Quadrature signal generation

The implementation of PLL in grid connected systems needs a Quadrature Signal Generator. There are different ways to generate quadrature signal, which are based on,

1. T/4 Transport delay : In this technique the input signal is time delayed by 1/4 of fundamental time period. If the grid voltage frequency changes, the QSG can't generate pure orthogonal signals, which will result with errors during synchronization. Due this reason this method of QSG is not used in this study.

2. Hilbert transform : Here a mathematical tool called *Hilbert transform* is used, which is basically a quadrature filter, which shifts only the phase angle of the input signal by ±90° leaving the magnitude unaffected. This transform will generate the output as given below.

$$sin(\omega t) \xrightarrow{H()} -cos(\omega t) \xrightarrow{H()} -sin(\omega t) \xrightarrow{H()} cos(\omega t) \xrightarrow{H()} sin(\omega t)$$

3. Inverse Park transform : This method of QSG uses both direct Park and inverse Park transformations as shown in the figure 32. In this case even if the PLL is well tuned with the input signal frequency, v_α and v'_β are not in perfect quadrature, hence the resultant signal will not have constant amplitude and frequency, hence v_d and v_q will have oscillations. These oscillations are attenuated by low pass filters (LPF) resulting with $\bar{v}_d$ and $\bar{v}_q$. This makes v'_α and v'_β from the inverse Park transformation of $\bar{v}_d$ and $\bar{v}_q$ to be in quadrature even if v_α and v'_α are not in phase. When the PLL is locked v_α will be in phase with v'_α and in quadrature with v'_β. Hence Park based PLL is used in this

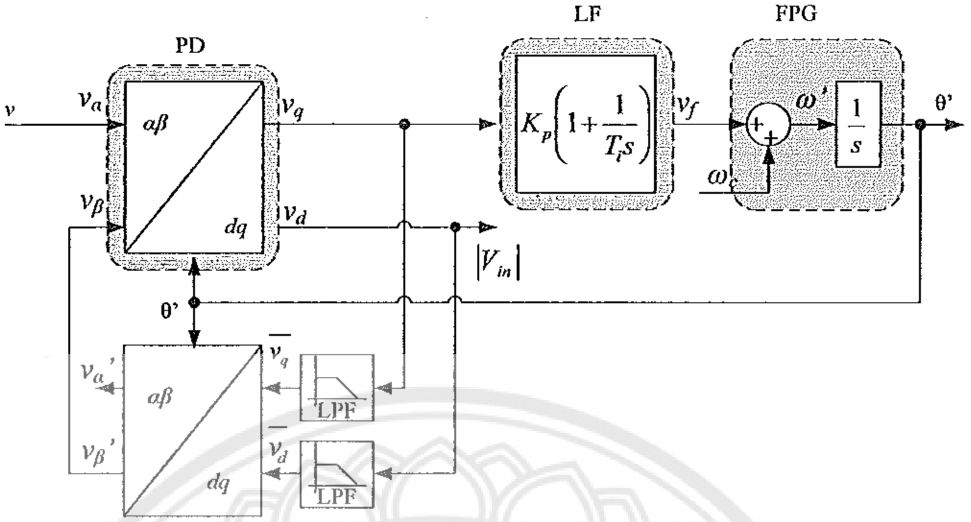

Figure 32 PLL with direct and inverse Park transformation

study for grid synchronization.

Line filter

The high frequency switching of PWM inverter results with a non sinusoidal voltage at the output with high frequency distortions. These non sinusoidal voltages cause the current to be highly distorted when connected to the load or the grid. These harmonics are to be controlled within certain limits pertaining to the standards (28) in case of grid integration. Common filters used in inverters are listed as under.

1. *L filter* : It is a simple inductor connected between the inverter output and the load or grid as shown in figure 33a. This simple filter topology avoids the resonance of the system with grid impedance in case of grid connected systems, as grid impedance is inductive below few kHz. A large value of inductance is needed to attenuate the high frequency ripples, resulting a bulky expensive filter. The voltage drop across the inductor and the higher cost make these filters to be used in high power applications such as several kW systems. These *L* filter systems provide 20dB/decade attenuation as they are first order systems.

2. *LC filter* : It is a combination of inductor and capacitor as shown in figure 33b in low pass configuration which results in a second order filter. These filters provide more attenuation than *L* filters with 40dB/decade. But still larger value of inductors

are required for attenuation. Moreover, the resonance frequency of the *LC* filter system depends on the grid impedance, making it less suitable for grid connected inverters.

3. *LCL filter* : Its a low pass T-network of *LCL* combination as in figure 33c, which forms a third order filter with an attenuation factor of 60dB/decade, which is higher than *L* and *LC* filters. It also provides a better decoupling between the filter and the grid impedance, making the resonance frequency of the system almost independent of the grid impedance with the lowest possible ripples at the grid side. The *LCL* filters have inherent resonance property, which are required to be damped to have stable interaction between the load and source impedances. These natural resonance phenomenon in *LCL* filters increases the risk of harmonic amplification at point of common coupling. These resonance can be damped either by active or passive damping methods.

There are different methods available on active and passive damping techniques.

1. *Passive damping* : Passive damping uses physical resistors either in series or in parallel to the inductors or capacitor of the filter. This method of damping is very simple and widely used. However, in high power applications of few hundred kW, the power loss in the damping resistor is higher, which reduces the efficiency of the system to a greater extent. Different configurations of passive damping techniques have been proposed in literature to minimize the losses in the passive damping methods.

2. *Active damping* : Active damping uses no physical resistor, instead control algorithms are used to minimize the effect of damping. These control techniques place the pole of the system in the optimum stable region to have stable dynamic performance. Capacitor current feedback control is also a kind of active damping, which can damp similar to resistor passive damping, which is a "virtual resistance". Capacitor voltage feedback control with a lead-lag network is another active damping method. Its a deformation of the capacitor current control. Active damping is also done by additional delay control. The main reason for instability of a third order *LCL* filter is the phase of -270° at resonance. This can be controlled by adding one-beat delay in current feedback, which is also a kind of active damping. Due to the higher ripple attenuation factor, the LCL filter has been designed for the study of grid connected fuel cell power generation system. The IEEE 1547 standard standardizes the interconnection of distributed resources with Electric Power Systems. According to (28) the allowable grid side current *THD*

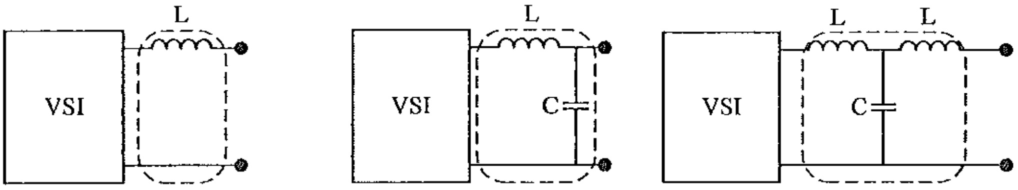

(a) L filter **(b) LC filter** **(c) LCL filter**

Figure 33 Filter topologies

is 5% to integrate the renewable power generation with the existing grid. The grid connected VSI with four different control control strategies such as direct grid side inductor current control and inverter side inductor current control, cascade inverter side inductor current control and capacitor current control are studied in (29). The simulation results have shown that the THD_i of grid injected current is the lowest in cascade control of inverter side current as inner loop when compared with the other control strategies. In (30) multi-variable control of paralleled grid connected inverters is presented with the description of coupling effect when more than one single phase inverters are paralleled to the grid. The behavior of single phase inverter is not the same when paralleled due to the coupling effect. It also deals with the actively damped *LCL* filter with capacitor current feedback control. In (31) a sensor less Kalman filter based grid connected VSI with *LCL* filter is discussed. It has been shown that the Kalman filter effectively restrains the effect of resonance in *LCL* filter by estimating the filter capacitor current. This ensures that the Kalman filter estimates the variables even in the noisy environment and with model uncertainties. The paper (32) gives an overview of various topologies for single phase inverters for distributed power generation. Single stage DC-AC conversion is of low cost but has limited input range, whereas multistage converters have wide input range and of high cost. Multistage inverters reduce the system size, boost the DC link voltage with DC-DC converters or high frequency transformers. In (33) a single phase grid connected inverter for PV power system has been studied with active power injection, reactive power compensation and harmonic suppression. An SRF based current control technique is employed in the full bridge DC-AC inverter system and the system was capable of injecting active power into the grid with low current *THD*. In (34) the DC current injection of the grid connected inverters is studied and a compensation method has been proposed. As compensation with current controllers are subjected to errors due to nonlinearity, active filter based compensation is proposed and the simulation results have shown the complete compensation of the DC components. The paper (35) investigates multi level multi-functional grid connected inverters and control techniques in photovoltaic systems. In (36) the grid connected inverter topologies with different control structures are discussed. The harmonic reduction in grid connected inverters is mainly due to the control structure implemented. PI controllers with dq control are widely used, whereas the controller with Proportional Resonance (PR) + Harmonic Compensator (HC) is found to be reliable and has the lowest harmonics with zero steady state error. The paper (37) presents a pseudodroop control structure in distributed generation, a critical case where PV power generation is more than the load demand overcharges the battery bank is controlled by an algorithm with frequency generator function. A regenerative PWM rectifier which gives back the power to the AC supply is studied in (38) to reduce the input harmonics and to improve the power factor. Different PWM techniques have been discussed in detail. In (39) a grid interactive inverter with fuzzy logic tuned PI controller is presented. This adaptive PI controller has resulted with low THD in inverter current even with different operating conditions and grid disturbances. A selection criterion of resonance frequency based on the control frequency in grid connected PWM rectifier with LCL filter is presented in (40) without passive damping for stable operation. The paper (41) gives the step by step procedure to design an LCL filter to reduce the switching frequency current ripples for a grid connected active rectifier with good dynamic response and reasonable stability margin. In (42), design procedure of LCL filters for grid connected inverters to mitigate the harmonics is described along with effect of delta and wye connected capacitors on possible grounding. The paper (43) presents a SRF current control for single phase grid connected VSC. The results have shown that the double line frequency components which were present in transient state are effectively eliminated in the steady state. In (44) a review on different current control techniques such as dq, $\alpha\beta$ and abc used in three phase grid interconnection of renewable power generation is presented. Though PI controller in dq frame is widely used, PR controller is found to be with high dynamic performance and selective harmonic compensation.

Dead beat (DB) controllers have shown superior performance during single phase grid fault. In (45), an unified structure of unbalanced SRF current control scheme is proposed and zero steady state error in line current is achieved. The paper (46) presented a new current feedback with PR controller where weighted average of two inductor currents of *LCL* filter is used as the feedback in current PR controller. This allows to choose a larger proportional gain to increase the control loop bandwidth to reduce the current harmonics within stability. The paper (47) investigated different control structures for grid connected distributed power generation system. The complexity of control structure becomes simpler if PR controller is implemented in stationary reference frame for current control than the structure in dq frame. In (48), the operation of PLL in distorted utility conditions is described along with the possible utility distortions. The PLL is completely implemented in software without any hardware filters. The paper (49), investigated the implementation of robust PLL circuit based on active and reactive (*PQ*) power theory. The system's stability during subharmonic, harmonic and negative sequence unbalance conditions are also investigated with the implemented control technique. In (50) different PLL algorithms for SRF control with different quadrature signal generation methods for grid connected single phase system are investigated. The algorithm based on inverse Park based PLL was found to be least sensitive to harmonic distortion whereas the algorithm with Hilbert transformation was most sensitive to the harmonics in the input signal. In (51) a passive damping with parallel resistor is investigated in grid connected inverters with *LCL* filters with ultra minimum extra losses and increased stability.

In (52), a new control structure with Proportional+Resonant and Harmonic Compensator has been studied, which made PR to act as a notch filter to track high frequency sinusoidal reference without increasing the gain as in classical PI controller. In (53), active damping method for grid connected voltage source converters with grid current controlled *LCL* filter is studied. It is shown that active damping with grid current feedback is equivalent to add virtual impedance in parallel with the grid side inductance which reduced the effect of transportation delay in digital systems. This study has also shows that the active damping has direct influence in the location of system poles. In (54), a comprehensive study of switching ripple filters has been made. There has been a constant increase in the use of *LCL* filters over two decades. The resonance of *LCL* filters have been controlled with different active and passive damping methods. Different improved passive damping methods were introduced to minimize the power loss in passive damping. Algorithms for lossless active damping were also developed. Though *LCL* filters are currently dominant in usage, the research on *LLCL* filters is substantially increasing over years and in future the usage of *LLCL* will be more than that of *LCL*. The paper (55) gives the design procedure for *LCL* filter for grid connected inverters with capacitor current feedback. It concludes that the active damping method with capacitor current feedback is effective in damping but affects the phase margin of the system. A design procedure has been proposed to meet the required frequency domain specifications such as phase margin, gain margin and steady state error to optimize the controller parameters. In (56), a grid current regulated three phase VSI wiht *LCL* filter is presented. An outer loop for grid current and an inner loop for capacitor current control was studied. The expressions of harmonic impedance have been derived to study the effect of supply distortion on harmonics. The paper (57) investigated the effect of inevitable delay on stability of a system in case of digital control implementations. A delay time control method has been proposed and proven that adjusting the delay time improves the stability of the system. In (58), the two current loop control of an *LCL* filter based grid connected inverter system is studied. The results have shown that the adoption of filter capacitor current control can effectively damp the resonance in the *LCL* system. In (59), a method to increase the reactive power capacity in a PV-Grid system to improve the PV penetration level is proposed. The proposed system consists of an inverter, a reactive power bank along with a PV-Grid system. This enabled the local PV distributed system to provide necessary reactive power support. It has been shown that the proposed system eliminates the switching transients and provides full range for reactive power control. In (60), reactive power control of a grid connected PV system to support the grid voltage is studied. It has been shown that the inverter can be controlled with pure active, pure reactive and mix of active and reactive powers with the help of independent control to support the grid.

Summary

To summarize, the substantial growth in every field such as automotive, electronics and medical etc., the power demand is of prime concern. Due to the green house effect and global warming, the investors are reluctant to invest in the conventional power plants and in turn on the transmission and distribution infrastructures. On the other hand, Distributed Generation has become as an attractive alternate solution, which has several benefits, like mitigating global warming, preserving fossil fuels from depletion and other such environment friendly nature. The rapid growth in the developments of the PV technology, Fuel Cell technology (3), Wind Energy technology and other such renewable energy technologies has proven that the renewable clean green energy sources are the future power sources. The development of Distributed Generation has always been aided with the recent advancements in battery, ultracapacitor, fuel cell and semiconductor technologies. The study has aimed at fuel cell based power generation system with gird integration. The basic theory related to all components of the proposed system has been reviewed in detail. The research articles related to DC-DC converter topologies, DC-AC inverter topologies, switching ripple filters, control techniques have been reviewed. The IEEE 1547 standard related to the grid connected distributed power generation system has been reviewed.

Due to the above mentioned advantages Dual Active Bridge topologies has been identified as one of the best suited DC-DC converter topology for fuel cell applications. Park based PLL synchronized full bridge inverter with unipolar PWM control under unbalanced SRF has been found to be a suitable system to have independent control on active and reactive power of the system. An *LCL* filter with grid current feedback control without damping is to be used as grid interface system due to its high ripple attenuation factor. Hence the system under the study should have lowest double line ripples ($< 15\%$) injected in to the fuel cell system and to have lowest *THD* ($< 5\%$) on the grid side current as per the standards given by US Department of Energy and IEEE 1547 respectively.

CHAPTER III

RESEARCH METHODOLOGY

Introduction

The fuel cell systems' construction, operation and characteristics are studied for better understanding the behavior of the system under no load and full load conditions. Based on the literature review the converter suitable to convert the low output DC voltage of the fuel cell in to a high voltage DC for its further conversion into AC is chosen. The Dual Active Bridge (DAB) has been identified as the suitable boost converter due to its high efficiency, high power density, Zero Voltage Switching (ZVS) capability and bidirectional power flow facility with galvanic isolation (5). Being a DC-DC converter, the DAB is designed as a boost converter to convert the low output DC voltage from the fuel cell to a bare minimum value of required AC voltage's peak value. A phase shift modulation is implemented to control the direction and amount of power flow and a high frequency transformer is designed for stepping up the voltage level to a minimum required value. The boosted DC voltage is further converted to a single phase AC for grid connection by a PWM controlled single phase inverter. An *LCL* filter is designed to have high ripple attenuation. The entire system is implemented as shown in the figure 34. Necessary control circuits are designed and implemented to meet the varying grid requirements. The entire system is tested with grid integration. The overall methodology followed is as shown in the figure 35.

This chapter describes,

1. Modeling and controlling of dual active bridge.
2. Modeling and controlling of grid connected inverter.
3. Design and construction of high frequency transformer.
4. Design and construction of leakage inductor (L_{lk}) filter.
5. Design and construction of *LCL* filter.

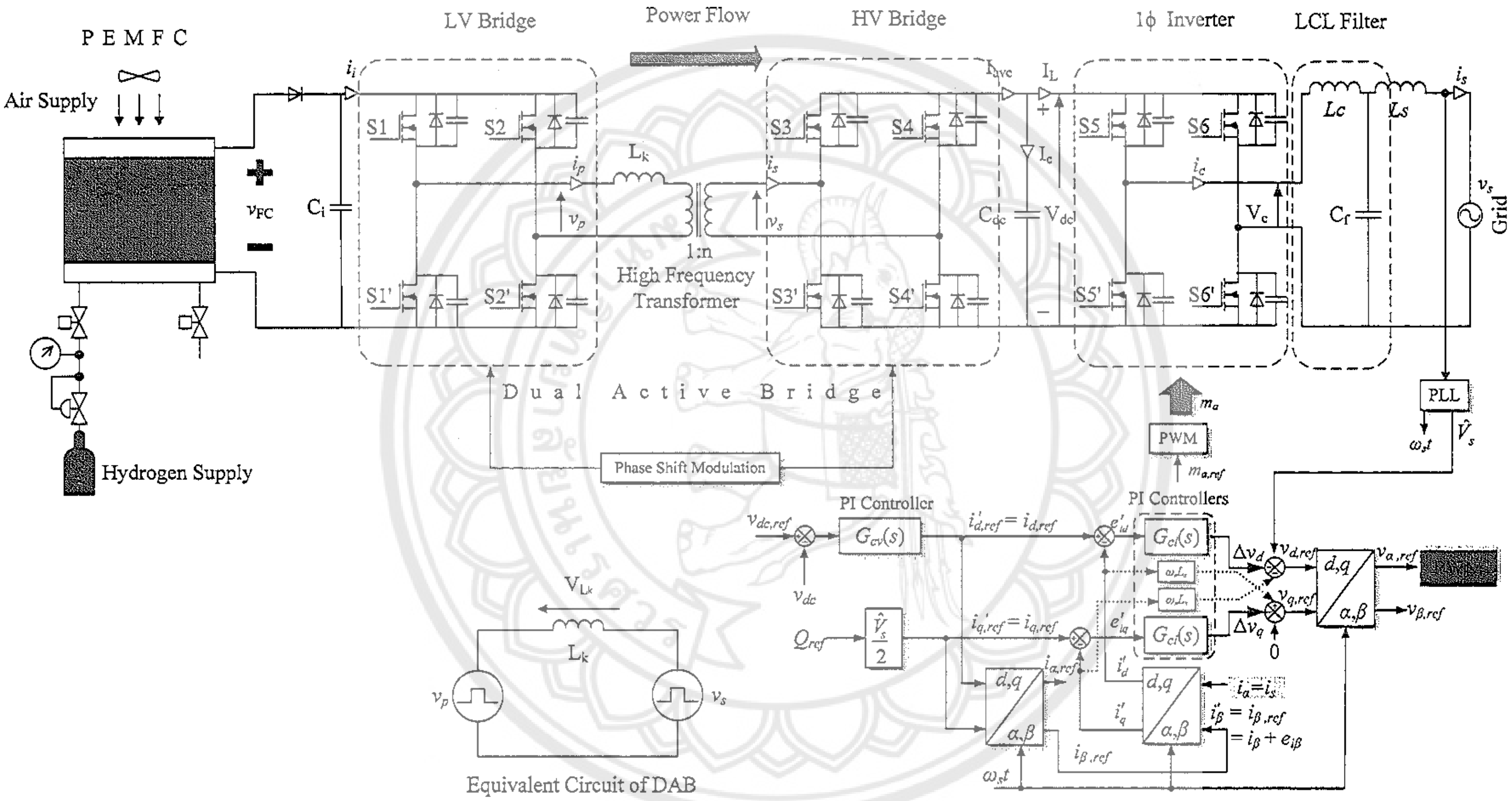

Figure 34 Fuel Cell Power Generation

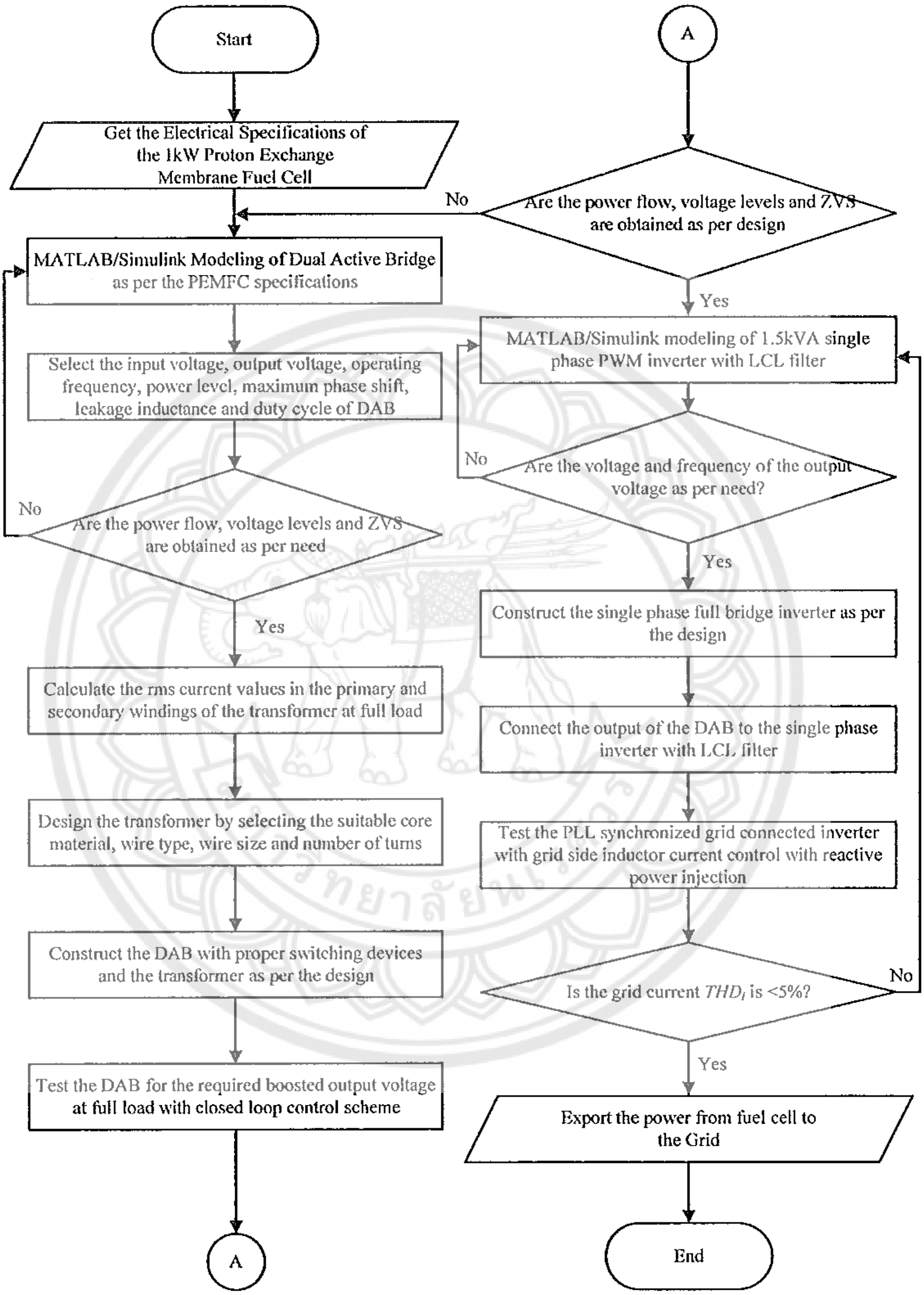

Figure 35 Flow Chart for the Methodology

Modeling and controlling

Modeling - Dual Active Bridge

The dual active bridge is modeled in MATLAB®/ Simulink using power system block sets. The input and output full bridges are constructed with the help of MOSFETs. A linear two winding transformer with 20kHz operating frequency is connected between the bridges with a series external leakage inductor L_{lk} needed for the required power transfer. The gate signals are generated with 50% duty cycle and with phase shift modulation between the input and output bridge. As the power will be transferred from the bridge with leading gate signal to the bridge with lagging gate signals, the input bridge at the fuel cell side is given with leading gate signals. The average power transfer from the fuel cell is given by,

$$\begin{aligned} P_{FC} &= \frac{1}{\pi}\int_0^{\pi} v_p(\theta)i_p(\theta)d\theta \\ &= \frac{V_{FC}}{\pi}\int_0^{\pi} i_p(\theta)d\theta \\ &= V_{FC}I_{ave} \end{aligned}$$

where

$$I_{ave} = \frac{V_{FC}d\phi(\pi-\phi)}{\pi\omega L_{lk}}$$

which gives

$$P_{FC} = \frac{V_{FC}^2 d\phi(\pi-\phi)}{\pi\omega L_{lk}} \tag{3.19}$$

The average current I_{ave} is used to model the DAB, which is a non linear function of the phase shift ϕ between the gate signals of the two bridges as given in 3.20

$$I_{ave} = \frac{V_{FC}d\phi}{\omega L_{lk}}K_{\phi} \tag{3.20}$$

where $K_{\phi} = \frac{(\pi-\phi)}{\pi}$ and hence $\phi K_{\phi} = \phi\frac{(\pi-\phi)}{\pi}$. The average current model of DAB is as shown in the figure 36 in which the figure 36b gives the open loop transfer function of

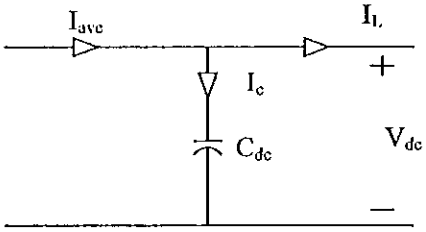

(a) Circuit model

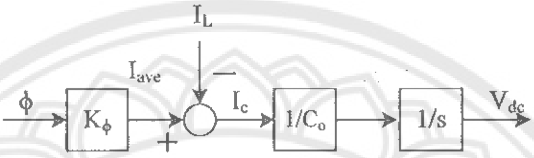

(b) Block diagram

Figure 36 DAB average current model

the system as below,

$$G_{DAB}(s) = \frac{K_\phi}{C_o}\frac{1}{s}$$

Controller design - Dual Active Bridge

The output of the dual active bridge is connected to a single phase inverter. The output of the inverter contains double line frequency signal. This double line frequency is reflected back to the dual active bridge and further to the fuel cell system as shown in the figure 37. As fuel cell current ripples are limited to be within 15% (61) to safe guard the life of the fuel cell, the controller of dual active bridge should limit the ripples which are injected to the fuel cell system within the permissible limits. The dual active bridge voltage control loop is implemented as shown in the figure 38 with a PI controller. From the voltage control loop, the open loop transfer function of the system is given by,

$$G_{OL}(s) = \frac{K_pK_c(1+T_cs)}{s^2(1+T_Fs)}$$

where $K_p = \frac{K_\phi}{C_o}$, which shows the plant is of variable gain nature as $K_\phi = \frac{(\pi-\phi)}{\pi}$ where ϕ is a variable. Hence the symmetrical optimum method (62) of tuning the controller

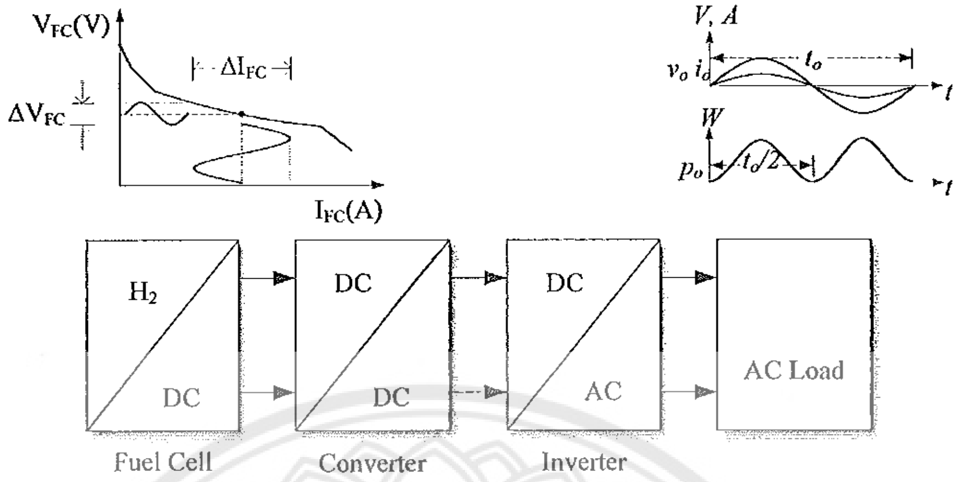

Figure 37 Double line frequency in a fuel cell system

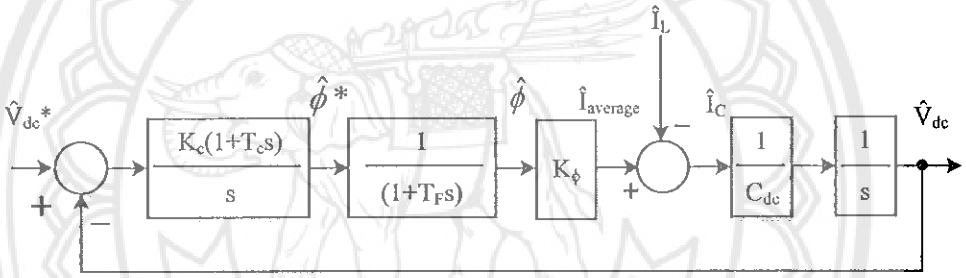

Figure 38 DC link voltage control loop

is used to calculate the controller parameters. This gives the values of K_c and T_c at the median of K_ϕ so that maximum phase margin is ensured at the gain cross over frequency ω_c even if K_ϕ is varied which is shown in figure 39. According to Symmetrical Optimum method, the values of K_c and T_c are given by,

$$K_p K_c = \frac{1}{\beta\sqrt{\beta}T_F^2}$$

$$T_c = \beta T_F$$

The β is a parameter in SO method, which takes the value between 4 and 16 and decides the phase margin of the system. Hence by adjusting β, the phase margin of the system can be adjusted. If the $\beta < 4$, the phase margin is $< 36°$ and if $\beta > 16$, the phase margin is $> 60°$, which are not desirable for a stable system. In this study, the

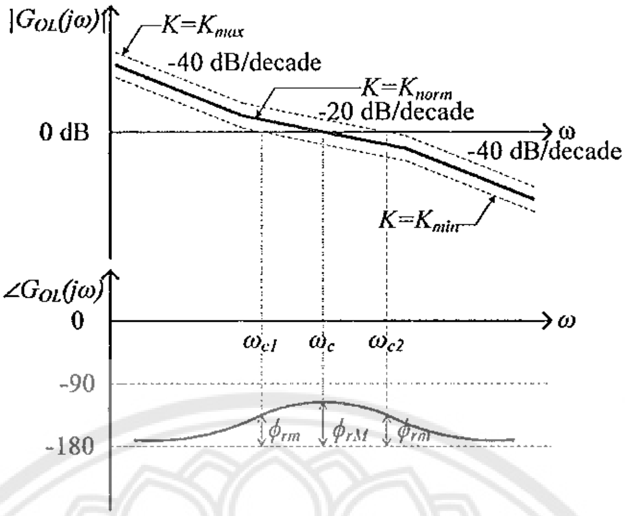

Figure 39 Frequency response of a SO tuned system

$\beta = 6$ was chosen for a required phase margin of 45°.

The optimal closed transfer function of the DAB system is given by,

$$G_{CL}(s) = \frac{1+\beta T_F s}{\beta\sqrt{\beta}T_F^3 s^3 + \beta\sqrt{\beta}T_F^2 s^2 + \beta T_F s + 1}$$

The cut frequency ω_c of the DC bus voltage control loop is selected by,

$$\omega_c = \frac{1}{\sqrt{\beta}T_F}$$

The open loop and closed loop Bode diagrams of the DAB system is shown in figure 40

Modeling - Grid connected VSC with LCL filter

The grid connected VSC with *LCL* filter is shown in the figure 41. The differential equations governing the system with the state variables, such as the voltage across the capacitors and current through the inductors are written to represent the system.

$$C_{dc}\frac{dv_{dc}(t)}{dt} = i_{average}(t) - mi_c(t) \tag{3.21}$$

$$L_c\frac{di_c(t)}{dt} + R_c i_c(t) = mv_{dc}(t) - v_{cf}(t) \tag{3.22}$$

$$C_f\frac{dv_{cf}(t)}{dt} = i_c(t) - i_s(t) \tag{3.23}$$

$$L_s\frac{di_s(t)}{dt} + R_s i_s(t) = v_{cf}(t) - v_s(t) \tag{3.24}$$

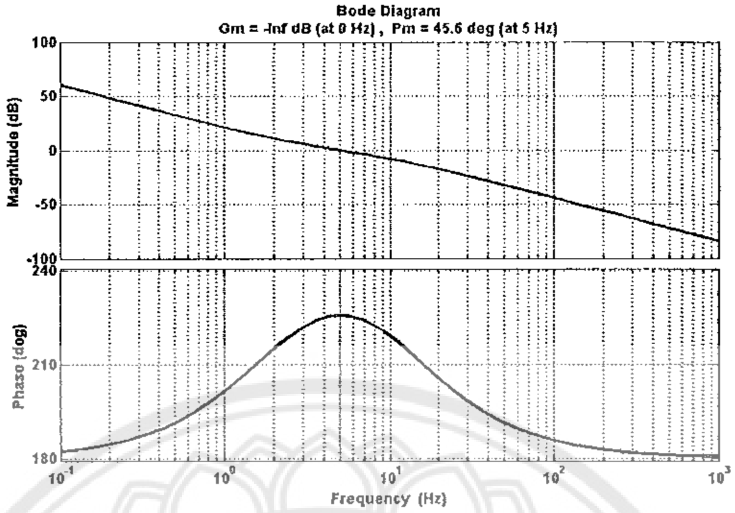

(a) Open loop DAB

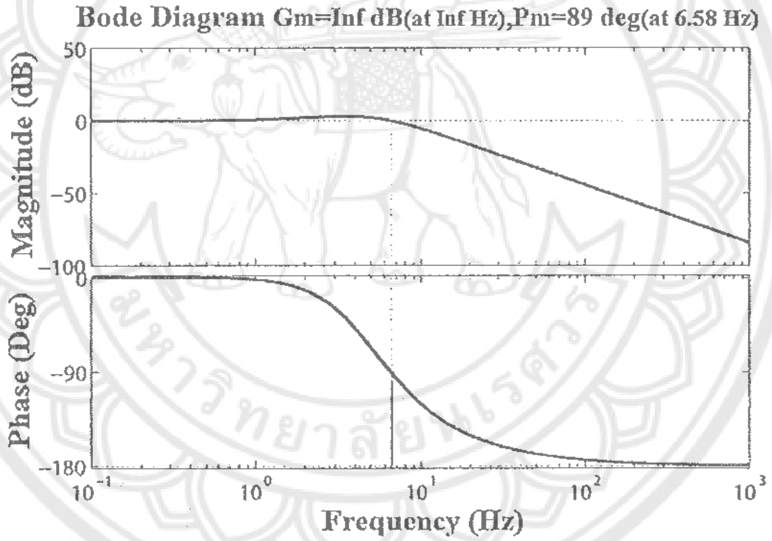

(b) Closed loop DAB

Figure 40 Bode diagram of DAB system

From these differential equations, the state variables can be extracted as,

$$v_{dc}(t) = \frac{1}{C_{dc}} \int (i_{average}(t) - m i_c(t))dt$$

$$i_c(t) = \frac{1}{L_c} \int (m v_{dc}(t) - v_{cf}(t))dt$$

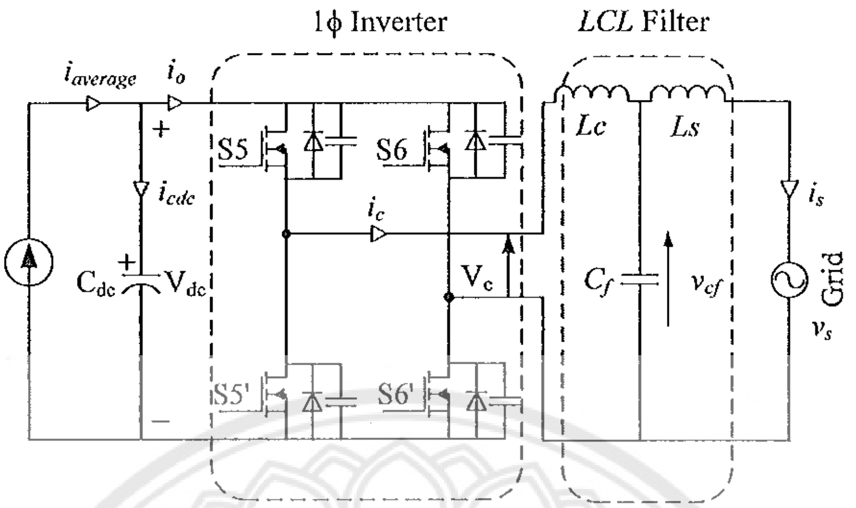

Figure 41 Grid connected VSC with LCL filter

$$v_{cf}(t) = \frac{1}{C_f}\int (i_c(t) - i_s(t))dt$$

$$i_s(t) = \frac{1}{Ls}\int (v_{cf}(t) - v_s(t))dt$$

These sets of equations are used and the VSI with *LCL* is modeled using MATLAB®/ Simulink.

Controller design - Grid connected VSC

The inverter in this study is a PWM controlled Voltage Source Inverter (VSI). A synchronous reference frame current control is implemented to limit the current ripples within the standards.

Let $v_s(t) = \hat{V}_s cos\omega_s t$ be the grid voltage, then the line current which is to be controlled is given by,

$$\begin{aligned} i_s(t) &= \hat{I}_s cos(\omega_s t + \phi) \\ &= \hat{I}_P cos\omega_s t - \hat{I}_Q sin\omega_s t \end{aligned}$$

where

$\hat{I}_P cos\omega_s t$ - the active power current

$\hat{I}_Q sin\omega_s t$ - the reactive power current.

By controlling these currents, the active and reactive powers in the inverter can be controlled. The set of differential equations described in 3.21 to 3.24 are considered in the controller design (45). The actual current components $i_c(t)$ and $i_s(t)$ through the converter side inductor (L_c) and inverter side inductor (L_s) can be represented in $\alpha\beta$ axis by a vector $\vec{x}^s = x_\alpha(t) + jx_\beta(t)$. This is done by letting $x_\alpha = x_s(t)$ and $x_\beta = x_s(t)e^{-j\frac{\pi}{2}}$ which gives,

$$L_c\frac{d\vec{i_c}^s(t)}{dt} + R_c\vec{i_c}^s(t) = \vec{m}^s(t)v_{dc}(t) - \vec{v}^s_{cf}(t) = \vec{v}^s_c(t) - \vec{v}^s_{cf}(t)$$

$$L_s\frac{d\vec{i_s}^s(t)}{dt} + R_s\vec{i_s}^s(t) = \vec{v}^s_{cf}(t) - \vec{v_s}^s(t)$$

where the "s" denotes stationary reference frame. By neglecting the effect of C_f in the current control design as its influence is less, it can be considered as a simple L filter design in which $L = L_c + L_s$ with winding resistance $R = R_c + R_s$ and $i_c = i_s = i$. Hence the inverter system equations in stationary reference frame get reduced to,

$$L\frac{d\vec{i}^s(t)}{dt} + R\vec{i}^s(t) = \vec{m}^s(t)v_{dc}(t) - \vec{v_s}^s(t)$$

which can then be transformed to rotational reference frame by Park transformation as given under,

$$L\frac{i_d(t)}{dt} + Ri_d(t) = m_d(t)v_{dc}(t) + \omega_s Li_q(t) - \hat{V}_s$$

$$L\frac{i_q(t)}{dt} + Ri_q(t) = m_q(t)v_{dc}(t) - \omega_s Li_d(t)$$

The inverse park transformation of above dq frame gives the current $i_\alpha(t)$ in $\alpha\beta$ frame as $i_\alpha(t) = i_d(t)cos\omega_s t - i_q(t)sin\omega_s(t)$. This indicates that the dq currents $i_d(t)$ and $i_q(t)$ controls the real and reactive powers. The β axis current can be obtained by phase shifting the measured current or else by a fictive axis emulator as given by,

$$L\frac{i_\beta(t)}{dt} + Ri_\beta(t) = m_{\beta,ref}(t)V_{dc,ref} - \hat{V}_s sin\omega_s t$$

The real and reactive powers can be independently controlled by controlling dq axis currents $i_d(t)$ and $i_q(t)$. The d-axis reference current $i_{d,ref}(t)$ is obtained from the DC bus voltage and q-axis reference current $i_{q,ref}(t)$ is obtained from the required reactive power to be injected whenever needed.

The general structure of VSI under synchronous reference frame (SRF) control is as shown in the figure 42. The modulating signal $m_{\alpha,ref}$ controls the inverter output voltage $v_c(t)$ in accordance with the required real (P) and reactive (Q) powers. The Park based PLL is used to extract the magnitude ($\hat{V}_s$) and the phase ($\omega_s t$) of the grid voltage. The structure shown in figure 42 is under unbalanced SRF. In this structure, the $i_{d,ref}(t)$ and $i_{q,ref}(t)$ obtained based on the required real and reactive power control is transformed into respective $\alpha\beta$ axis quantities by inverse Park transformation resulting with $i_{\alpha,ref}(t)$ and $i_{\beta,ref}(t)$. This $i_{\alpha,ref}(t)$ is considered as required $i_{s,ref}(t)$ as command signal and the actual measured grid side current $i_s(t)$ is fed as a feedback signal for the calculation of current error in dq axis. The Park transformation is used to transform the $\alpha\beta$ to dq before the error calculation. During Park transformation an arbitrary β axis current i_β^* is used.

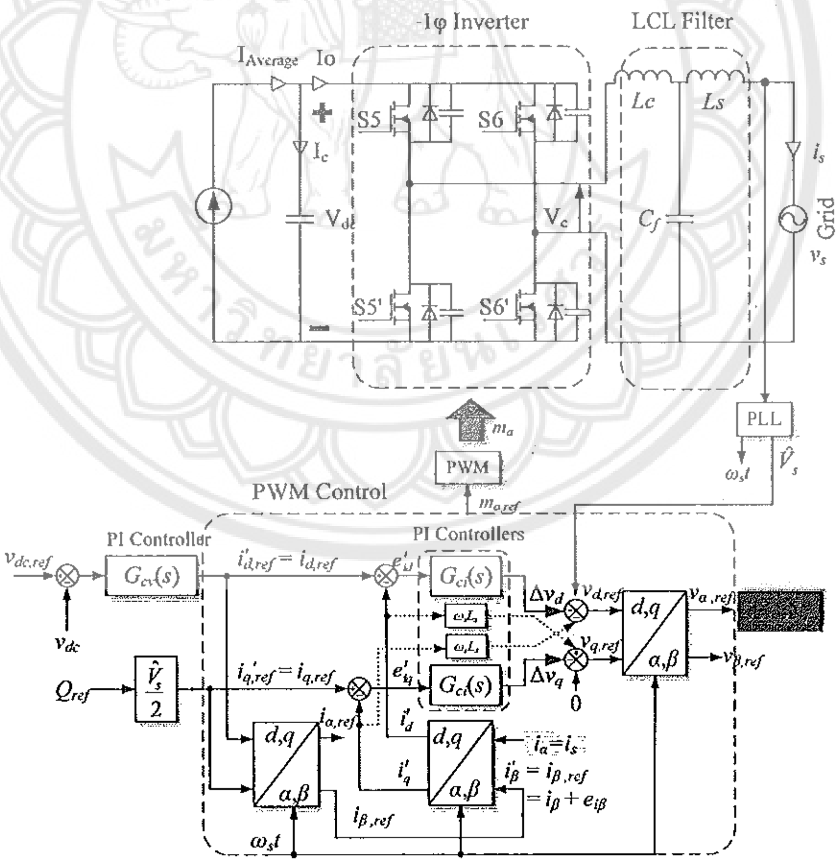

Figure 42 VSI under unbalanced synchronous reference frame current control

These signals are obtained as given under,

$$\begin{bmatrix} i'_{d,ref} \\ i'_{q,ref} \end{bmatrix} = \begin{bmatrix} cos\omega_s t & sin\omega_s t \\ -sin\omega_s t & cos\omega_s t \end{bmatrix} \begin{bmatrix} i_{\alpha,ref} \\ i^*_\beta \end{bmatrix} \tag{3.25}$$

and

$$\begin{bmatrix} i'_d \\ i'_q \end{bmatrix} = \begin{bmatrix} cos\omega_s t & sin\omega_s t \\ -sin\omega_s t & cos\omega_s t \end{bmatrix} \begin{bmatrix} i_\alpha \\ i^*_\beta \end{bmatrix} \tag{3.26}$$

The notation “’” is given for unbalanced reference frame. The currents in 3.26 are subtracted from 3.25 to get their respective error signals as given under,

$$\begin{bmatrix} e'_{id} \\ e'_{iq} \end{bmatrix} = (i_{\alpha,ref} - i_\alpha) \begin{bmatrix} cos\omega_s t \\ -sin\omega_s t \end{bmatrix} = e_{i\alpha} \begin{bmatrix} cos\omega_s t \\ -sin\omega_s t \end{bmatrix} \tag{3.27}$$

Since i^*_β is given as a common signal in both Park transformations, the related error signal $e_{i\beta} = 0$, which is making unbalance in the dq axis error components. By inverse Park transformation, the grid current error $e_{i\alpha}$ is given by

$$e_{i\alpha} = e_{id} cos\omega_s t - e_{iq} sin\omega_s t \tag{3.28}$$

where e_{id} and e_{iq} are the current error components in balanced SRF. Substituting 3.28 in 3.27 gives,

$$\begin{bmatrix} e'_{id} \\ e'_{iq} \end{bmatrix} = \frac{1}{2} \begin{bmatrix} (1 + cos2\omega_s t) & -sin2\omega_s t \\ -sin2\omega_s t & (1 - cos2\omega_s t \end{bmatrix} \begin{bmatrix} e_{id} \\ e_{iq} \end{bmatrix} \tag{3.29}$$

Though the orthogonal signal $i^*_\beta(t)$ can be arbitrary, its generation should be a controlled one. In the structure shown in figure 42 the dq axis reference currents $i_{d,ref}(t)$ and $i_{q,ref}(t)$ are directly given to the error detector, and an inverse Park transformation is done to obtain the required $i_{\beta,ref}(t)$. This $i_{\beta,ref}(t)$ further undergoes Park transformation to get unbalanced SRF current components $i'_d(t)$ and $i'_q(t)$ for error calculations $e'_{id}(t)$

and $e'_{iq}(t)$. The orthogonal reference current can also be written as,

$$i_{\beta,ref}(t) = i_\beta(t) + e_{i\beta}(t)$$

where $i_\beta(t)$ and $e_{i\beta}(t)$ are virtual orthogonal current and current error in the balanced SRF. From this the unbalanced dq currents are given by,

$$\begin{bmatrix} i'_d \\ i'_q \end{bmatrix} = \begin{bmatrix} i_d \\ i_q \end{bmatrix} + e_{i\beta} \begin{bmatrix} sin\omega_s t \\ cos\omega_s t \end{bmatrix} \tag{3.30}$$

By replacing $e_{i\beta} = e_{id} sin\omega_s t + e_{iq} cos\omega_s t$ in 3.30 we get,

$$\begin{bmatrix} i'_d \\ i'_q \end{bmatrix} = \begin{bmatrix} i_d \\ i_q \end{bmatrix} + \frac{1}{2} \begin{bmatrix} (1 - cos\omega_s t) & sin2\omega_s t \\ sin2\omega_s t & (1 + cos2\omega_s t) \end{bmatrix} \begin{bmatrix} e_{id} \\ e_{iq} \end{bmatrix} \tag{3.31}$$

The error signals can be obtained subtracting the unbalanced dq currents from balanced dq reference currents, we get the same expression for the error signals as in 3.29. These unbalanced dq current components which are obtained from reference current signals are used to control the real and reactive powers in the inverter system.

The transfer function of an LCL filter connected to the inverter is given by,

$$\frac{i_s}{v_c} = \frac{1}{s^3(L_c L_s C_f) + s(L_c + L_s)} \tag{3.32}$$

The LCL filter is approximated as L filter for the controller design by neglecting the effects of C_f. Hence the transfer function gets deduced to,

$$\frac{i_s}{v_c} = \frac{1}{s(L_c + L_s)} = \frac{1}{sL} \tag{3.33}$$

Considering the winding resistances R_c and R_s of the inductors L_c and L_s, the transfer function becomes

$$\frac{i_s}{v_c} = \frac{1}{(R_c + R_s) + s(L_c + L_s)} = \frac{1}{R + sL} \tag{3.34}$$

where the inductors L_c, L_s and R_c , R_s are taken as lumped parameters L and R. The grid current control loop is as shown in the figure 43. A PI controller is introduced in the loop

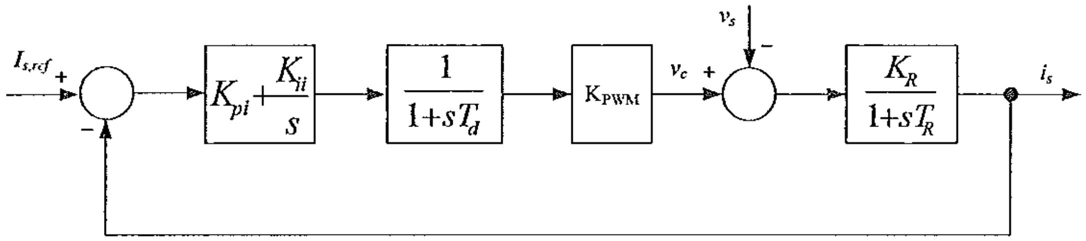

Figure 43 Grid current control loop in SRF

with a delay time of T_d considering the delay in the digital implementation of the control loop. Normally T_d is assumed to be $1.5T_s$, where T_s is the switching time. Hence the open loop transfer function of the grid current control loop is given by,

$$G_{OL,i} = \left(K_{pi} + \frac{K_{ii}}{s}\right)\left(\frac{1}{1+sT_d}\right)\left(\frac{K_R}{1+sT_R}\right) \tag{3.35}$$

where $K_R = \frac{V_{dc}}{R}$ and $T_R = \frac{L}{R}$. This gives the closed loop transfer function as,

$$G_{CL,i} = \frac{K_{pi}K_R s + K_{ii}K_R}{T_R T_d s^3 + T_R s^2 + K_{pi}K_R s + K_{ii}K_R} \tag{3.36}$$

The extended Symmetrical Optimum method is chosen for tuning of the PI controller. Which gives the K_p and Ki of the controller as,

$$K_{pi} = \frac{T_R}{2K_R T_d}$$

$$K_{ii} = \frac{T_R}{8K_R T_d^2}$$

The block diagram of the DC bus voltage control loop for single-phase grid-connected VSI is as depicted in figure 44. A first order low pass filter (LF) is added in series with the PI regulator for the voltage control loop. The PI is tuned by the extended SO method in selecting the LF time constant T_f as well as parameters of the PI controller. The DC bus ripples are mainly due to the grid oscillating power $\tilde{p}_s(t)$. The LF helps in attenuating the ripple power further down to -40 dB/Decade. The bandwidth of the voltage loop is selected as 10 Hz to attenuate the double line frequency ripple components in the DC link voltage, while the high bandwidth of the line current loop $G_{CL,i}$ is approximated to be unity gain.

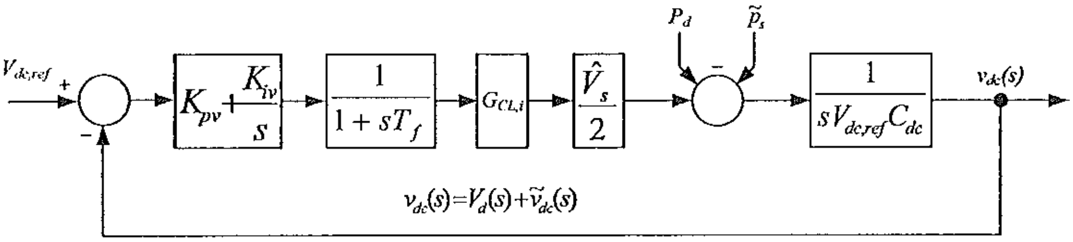

Figure 44 DC bus voltage control loop

Design and construction of High Frequency Transformer

This section describes the step by step procedure to design a high frequency transformer for the desired specifications.

Design Specifications

The transformer is designed to meet the specifications of Horizon - **H1000** : PEMFC as given below.

Rated power :1000W

Rated performance :28.8V@35A

Output voltage range :30V-45V

Hence in designing the transformer, $V_{in} = 38V$, $V_{out} = 400V$, $f_s = 20kHz$, $P_o = 1kW$ were chosen as the values of various required parameters. The switching frequency is assumed to be $20kHz$ due to the limitation on the magnetic core materials and the value of V_{dc} was chosen based on the AC voltage required during inversion. The DC input of an inverter should be at least the peak value of the AC voltage required.

Design Procedure

1. *Calculation of the Primary Volt-Seconds* (λ_1): The primary *volt-sec* is calculated using the relation 3.37.

$$\lambda_1 = dT_sV_{in} \tag{3.37}$$

where

d - Duty cycle

T_s - Switching time

V_{in} - Input voltage.

2. *Calculation of primary RMS current (I_1)*: The primary RMS current can be calculated graphically from the waveform obtained by MATLAB®modeling. The generalized expression for the primary RMS current has been deduced as in ??.

3. *Calculation of secondary RMS current (I_2)*: The secondary RMS current can be calculated from the calculated primary RMS current from

$$I_2 = nI_1A$$

where n is the turns ratio given by

$$n = \frac{V_{in}}{V_{out}}$$

4. *Calculation of total RMS current referred to primary (I_{tot})*: The total current in the DAB referred to primary winding is calculated from the primary RMS and secondary RMS currents as given below.

$$I_{tot} = I_1 + \frac{I_2}{n}$$

5. *Calculation of core size (K_{gfe})*: From the required electrical quantities the $Kgfe_{elect}$ is calculated from

$$K_{gfe_{elec}} = \frac{\rho(\lambda_1)^2(I_{tot})^2(K_{fe})^{\frac{2}{\beta}}}{4K_u(P_{tot})^{\frac{(\beta+2)}{\beta}}}10^8 \tag{3.38}$$

where

ρ is the wire effective resistivity in $(\Omega - cm)$

K_{fe} is the core loss coefficient in (W/cm^3T^{β})

K_u is the winding fill factor

P_{tot} is the allowed total power dissipation in (W)

β is the core loss exponent

The value of K_{fe} is calculated from $K_{fe} = \frac{P_{fe}}{(B_{max})^{\beta}}$. The values of B_{max} and P_{fe} are obtained from the graph from $N87$ ferrite material data sheet as shown in the figure 45. Substituting these values in the expression (3.38) we get,$K_{gfe_{elec}}$. The ferrite core can

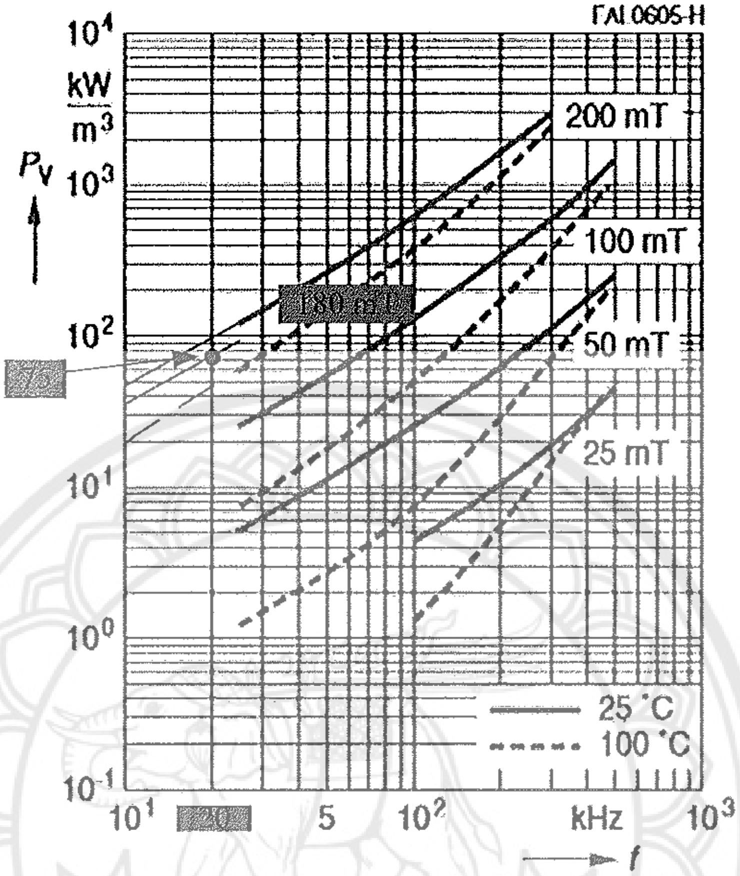

Figure 45 Relative core losses versus frequency of *N*87 ferrite material

be chosen from the core geometry by calculating K_{gfe} of the core to meet the required specifications as given by $K_{gfe_{elec}}$. The core whose K_{gfe} is just greater than $K_{gfe_{elec}}$ is chosen. To calculate K_{gfe} of the core, the following expression is used.

$$K_{gfe_{core}} = \frac{W_A(A_c)^{2(\beta-1)/\beta}}{MLT(l_m)^{2/\beta}} \left[\frac{\beta}{2}^{-\left(\frac{\beta}{\beta+2}\right)} + \frac{\beta}{2}^{\left(\frac{2}{\beta+2}\right)} \right]^{-\left(\frac{\beta+2}{\beta}\right)} \tag{3.39}$$

where

W_A is core window area in cm^2

MLT is Mean Length per Turn in cm

A_c is Core cross sectional area in cm^2

l_m is Magnetic path length in cm

By substituting the required parameters from the data sheet of E65 core, we get the value of $k_{gfe_{core}}$. Since the required $K_{gfe_{elec}}$ is approximately equal to $K_{gfe_{core}}$ of E65, this core is chosen for the design.

6. *Calculation of peak flux density* (ΔB): The peak flux density is calculated based on the core geometry from the expression (3.40).

$$\Delta B_{geo} = \left[10^8 \frac{\rho(\lambda_1)^2(I_{tot})^2(MLT)}{2K_u W_A A_c^3 l_m \beta K_{fe}}\right]^{\frac{1}{\beta+2}} \tag{3.40}$$

7. *Calculation of primary turns* (n_1): The number of turns in the primary winding is calculated from the expression (3.41)

$$n_1 = \frac{\lambda_1}{2\Delta B_{geo} A_c} 10^4 \tag{3.41}$$

If n_1 is found to be a fractional value, it can be rounded to the nearest integer.

8. *Calculation of secondary turns* (n_2): The number of turns in the secondary is calculated by,

$$n_2 = \frac{n_1}{n} \tag{3.42}$$

If n_2 is found to be a fractional value, it can be rounded to a nearest integer.

9. *Calculation of window area for primary and secondary winding* (α_1, α_2): The window areas are calculated from the expressions (3.43) and (3.44).

$$\alpha_1 = \frac{I_1}{I_{tot}} \tag{3.43}$$

$$\alpha_2 = \frac{n_2 I_2}{n_1 I_{tot}} \tag{3.44}$$

10. *Calculation of wire sizes for primary and secondary winding*(A_{w1}, A_{w2}): The wire size calculations are given by the relations,

$$A_{w1} \leq \frac{\alpha_1 K_u W_A}{n_1} \tag{3.45}$$

$$A_{w2} \leq \frac{\alpha_2 K_u W_A}{n_2} \tag{3.46}$$

From these the diameters of the wires are calculated from

$$D_{w1} = 10\sqrt{\frac{4A_{w1}}{\pi}}(mm)$$

$$D_{w2} = 10\sqrt{\frac{4A_{w2}}{\pi}}(mm)$$

11. *Peak ac flux density after turn adjustment*: The peak AC flux density after turns adjustment is given by,

$$\Delta B_{adj} = \frac{\lambda_1 10^4}{2n_1 A_c}$$

It should to be less than the maximum flux density of the selected core (in this design E65).

12. *Power loss calculations*: The core loss is calculated from

$$P_{fe} = K_{fe}(\Delta B_{adj})^{\beta} A_c l_m$$

The copper loss is Calculated from

$$P_{cu} = \left[\frac{\rho(\lambda_1)^2(I_{tot})^2}{4K_u}\right]\left[\frac{(MLT)}{W_A(A_c)^2}\right]\left[\frac{1}{\Delta B}\right]^2$$

13. *Calculation of wire length*: The total wire length required for primary and secondary winding shall be obtained by,

$$L_{w1} = n_1 MLT$$

$$L_{w2} = n_2 MLT$$

The calculated transformer design parameters are listed in the table 3.

The high frequency transformer is constructed with the help of two E65 cores stacked together to meet the required core size. Served *Litz* wires of $265 * 0.1266e^{-3}$ and $40 * 0.1266e{-}3$ are used to wind the primary and secondary windings respectively with respective turns.

Table 3 High frequency transformer design paramters

Parameter	Values
Duty cycle, d	0.5
Switching time, T_s	$50\mu s$
Input voltage, V_{in}	$38V$
Primary Volt-Sec, λ_1	$9.5e^{-4}$
Primary RMS current, I_1	$40.23A$
Secondary RMS current, I_2	$3.82A$
Primary turns, n_1	5
Secondary turns, n_2	53
Turns ratio, $1:n$	$1:10.6$
Total RMS current referred to primary, I_{tot}	$80.45A$
Wire effective resistivity, ρ	$1.724e^{-6}\Omega cm$
Core power loss, P_{fe}	$0.075W/cm^3$
Copper power loss, P_{cu}	3.94W
Maximum flux density, B_{max}	$0.18T$
Peak flux density after turns adjustment, ΔB_{adj}	0.0898T
Core loss exponent, β	2.7
Core loss coefficient, K_{fe}	7.6882
Winding fill factor, K_u	0.4
Total allowable power loss, P_{tot}	$7W$
Core size from electrical parameters, $K_{gfe_{elect}}$	0.0964
Core size from E65 geometry, $K_{gfe_{core}}$	0.1437

Design and construction of Leakage inductor (L_{lk})

The following is the step by step procedure to design the leakage inductor required for the power transfer. The required value of the leakage inductor L_{lk} is found from the power expression 3.19. The design is considered to connect the leakage inductor on the high voltage winding of the transformer. The K_g method is followed to design the leakage inductor.

1. *Determination of core size*: The required core size of the leakage inductor to meet the required electrical specifications is calculated as given in the equation 3.47.

$$K_{gfe_{elect}} = \frac{\rho \lambda^2 I^2 K_{fe}^{\left(\frac{2}{\beta}\right)}}{2K_u (P_{tot})^{\left(\frac{\beta+2}{\beta}\right)}} 10^8 \tag{3.47}$$

where $K_{fe} = \frac{P_{fe}}{B_{max}^{\beta}}$.

The core size $K_{gfe_{core}}$ suitable to meet the required $K_{gfe_{elect}}$ can be found from 3.39. In this design the $K_{gfe_{core}}$ of ETD49 core has met the required $K_{gfe_{elect}}$. The core losses can be minimized by selecting the core with lower value of K_{fe}.

2. *Evaluation of AC peak flux density*: The AC peak flux density ΔB is calculated using the relation 3.48.

$$\Delta B = \left[10^8 \frac{\rho \lambda^2 I^2}{2K_u} \frac{(MLT)}{W_A A_c^3 l_m} \frac{1}{\beta K_{fe}}\right]^{\left(\frac{1}{\beta+2}\right)} \tag{3.48}$$

3. *Number of turns*: The number of turns required is calculated as under

$$n = \frac{\lambda}{2\Delta B A_c} 10^4 \tag{3.49}$$

The value of n can be rounded off to a nearest integer.

4. *Air gap length*: The required air gap in the core is calculated from the equation 3.50.

$$l_g = \frac{\mu_o A_c n^2}{L} 10^{-4} \tag{3.50}$$

where

A_c - in cm^2

l_m - in m

The air gap can also be expressed in terms of A_L in $mH/1000$ turns as

$$A_L = \frac{L}{n^2} 10^9 \tag{3.51}$$

5. *Evaluation of wire size*: The size of the wire to be wound is found from the

equation 3.52

$$A_w = \frac{K_u W_A}{n} \tag{3.52}$$

6. *Power loss*: The copper, iron and total losses in the inductor are found by the following expressions.

$$P_{cu} = \frac{\rho n(MLT)}{A_w} I^2 \tag{3.53}$$

$$P_{fe} = K_{fe}(\Delta B)^{\beta} A_c l_m \tag{3.54}$$

$$P_{tot} = P_{cu} + P_{fe} \tag{3.55}$$

Table 4 Leakage inductor L_{lk} design parameters

Parameter	Values
Leakage inductance, L_{lk}	$890\mu H$
RMS current, I	$3.36A$
The wire effective resistivity, ρ	$1.724e^{-6}$
Core loss exponent, β	2.7
Maximum flux density, B_{max}	$0.29T$
Power loss, P_{fe}	$0.2W/cm^3$
Winding fill factor, K_u	0.35
Total allowable power loss, P_{tot}	$7W$
Core size from electrical parameters, $K_{gfe_{elect}}$	0.0339
Core size from ETD49 geometry, $K_{gfe_{core}}$	0.0410
Number of turns, n	118
Air gap length, l_g	$0.0041m$
Wire size, A_w	0.008

Hence the leakage inductor is wound as per the design parameters listed in the table 4. Served *Litz* wire of $40 * 0.1266e^{-3}$ is used with ETD49 core to construct the leakage inductor with 118 turns.

Design and construction of *LCL* filter

To design *LCL* filter, it is approximated as *L* filter by neglecting C_f as it behaves similar to *L* filter till the resonance frequency. The design of *LCL* filter depends on the required level of ripple attenuation, switching frequency, applied PWM technique and the reactive power requirement.The inverter system is designed to have a rated voltage of $v_s = 230V$, rated apparent power $Sn = 1.5kVA$, DC link voltage $V_dc = 400V$, the grid frequency $f_g = 50Hz$ with the switching frequency $f_{sw} = 10kHz$. The base impedance Z_b and base capacitance C_b of the system required per unit conversion are calculated as given in equations 3.56 and 3.57 respectively.

$$Z_b = \frac{V_{rms}^2}{S_n} \tag{3.56}$$

$$C_b = \frac{1}{\omega_g z_b} \tag{3.57}$$

To design the inverter side inductance L_c, the maximum allowable ripples at the inverter side is calculated from the rated current using the relation given in Equation 3.58 and inductance L_c is calculated by the Equation 3.59 for unipolar PWM control.

$$\Delta I_{L_c,max} = \%Ripples\left(\frac{kVA\sqrt{2}}{V_{rms}}\right) \tag{3.58}$$

$$L_c = \frac{V_{dc}}{8(\Delta I_{L_c,max})f_{sw}} \tag{3.59}$$

The filter capacitance C_f decides the amount of reactive power absorption and is given by $C_f = xC_b$, where x is the percentage of reactive power absorbed. The value of x is limited to be less than 5% for unity power factor. For stable operation of the *LCL* filter, the resonance frequency f_r of the filter is chosen from the criterion given by $\frac{f_{sw}}{2} > f_r > \frac{f_{sw}}{4}$. The grid side inductance L_s is calculated from Equation 3.60.

$$L_s = \frac{L_c}{(\omega_r^2 L_c C_f) - 1} \tag{3.60}$$

where ω_r is the resonance frequency. The base impedance Z_b and base capacitance C_b are calculated from the equations 3.56 and 3.57 respectively. By choosing the switching frequency f_{sw} as $10kHz$, the resonance frequency f_r as $6kHz$, the maximum allowable current ripples on inverter side as 16% and the percentage of reactive power absorption x as 2.5% , the inverter side inductance L_c, grid side inductance L_s and filter capacitance C_f are calculated as listed in the table 5.

Table 5 *LCL* parameters

Parameter	Value
Grid side inductance, L_s	$0.35mH$
Inverter side inductance, L_c	$3.4mH$
Filter capacitance, C_f	$2.25\mu F$
Resonance frequency, f_r	$6kHz$

To construct the inductors, proper magnetic core, wire size and number of turns are chosen as per calculated values of inductors L_c and L_s. The current factor k_i, window utilization factor k_u and temperature rise ΔT are chosen accordingly. The area product A_p, of the required cores for L_c and L_s helps in the selection of the core sizes. The maximum flux density B_{max} is limited by the saturation flux density B_{sat} for the core material and is selected to be 0.35 T as given in (63). The converter side inductor L_c was constructed from a T300-26 iron powder core stacked together with a T300-26D, with 120 turns of a 1.9 mm diameter enameled copper wire. For the grid side inductor L_s, 46 turns of 1.7 mm diameter enameled copper wire were wound on a T184-26 iron powder core.

CHAPTER IV

RESULTS AND DISCUSSION

This chapter describes the simulation and experimental results of dual active bridge and grid connected single phase inverter with *LCL* filter.

Simulation results of Dual Active Bridge

The detailed modeling of dual active bridge is done as described in the previous section with the help of voltage and current waveforms obtained from the MATLAB®/ Simulink modeling. The average current model of the DAB obtained mathematically from graph is used for the controller design. A DC voltage source with an internal resistance of 0.333Ω is used to emulate the dynamic nature of fuel cell. This 0.333Ω is equivalent to the dynamic resistance of the Horizon®fuel cell. The MOSFETs are used to construct the bridges of DAB and the inverter. A linear transformer with the required turns ratio has been connected between the input and output bridges. An external inductor is connected in series with the primary winding of the transformer as the leakage inductor (L_{lk}) required for the proper power transfer. The DAB was connected to a PWM controlled 1ϕ inverter as the load. The resistive load is applied in steps of 100W and 1000W at the output of the inverter. This injected a double line frequency ripples at the DC side input of the DAB. The bandwidth of the DAB voltage control loop was varied from $1Hz$ to $25Hz$ in steps. This change in the bandwidth had an effect on the amount of fuel cell voltage and current ripples. The parameters of PI controller in the DC link voltage control loop are obtained by extended Symmetrical Optimum method of tuning to ensure the minimum phase margin of 45° with the parameter β of value 6. The PI controller in the loop generates the required phase shift ϕ between the leading input bridge and the lagging output bridge under phase shift modulation to regulate the DC link voltage constant at $V_{dc,ref}$ even when the load changes.

The set point tracking and the disturbance rejection can be observed from the figure 46 where there is an initial load of 100W and a 1000W load is applied at 0.5s.

The control loop has responded and the DC link voltage is regulated at 400V within 0.1*s*. At the 0.7*s* instant a 900W load was removed and a 100W load was maintained at the inverter side. Due to the disturbance at 0.7*s* there is overshoot of 25*V* in the DC link voltage and is regulated at 400V in 0.2*s*.

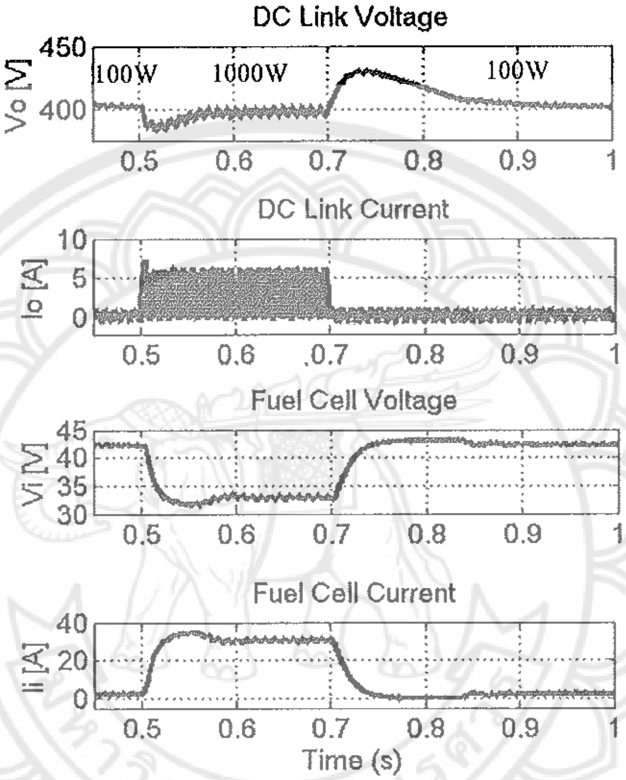

Figure 46 DAB simulation results with a step load change of 100 W and 1000 W vice versa.

The figure 47 shows the inverter load voltage and current for the step changes in the load. The DAB with an inverter as a load has experienced double line frequency ripples as shown in the figure 48. These ripples are introduced into the fuel cell system due to the AC load connected to the DAB. The ripples shown here are with a controller bandwidth of 5*Hz*. When the controller bandwidth is varied and it has been found that there is a significant increase in the ripple content as there is an increase in bandwidth. The increase in the ripples as the increase in the controller bandwidth is shown in the figure 49. The system had the lowest ripples at a bandwidth of 1*Hz* but in such case

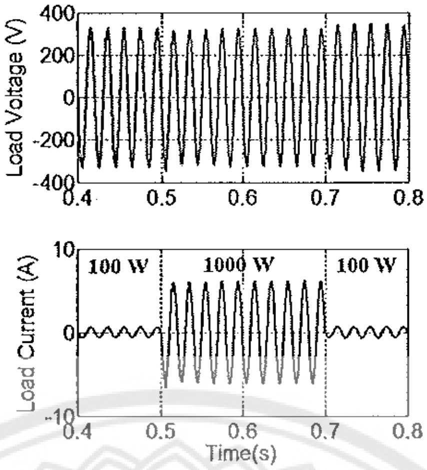

Figure 47 Inverter simulation results with a step load change of 100 W and 1000 W vice versa.

the system was very much sluggish. At a bandwidth of 5*Hz* it has been found that the system responded quickly as shown in the figure 46 with lower voltage ripples of 1.74% and current ripples of 4.29% which are well within the permissible limits. Hence by adjusting the voltage control loop bandwidth of the PI controller, the ripple content can be controlled at the fuel cell system.

Simulation results of Grid Connected Inverter

The mathematical model with the differential equations described in the earlier section is used to simulate the results of a single phase grid tied inverter in MATLAB®/ Simulink platform. A PLL based synchronization is used for grid integration to extract the grid voltage and phase angle. An unbalanced SRF grid current control is employed to reduce the amount of current ripples into the system. The *LCL* filter designed to have higher ripple attenuation factor has reduced the current ripples within the permissible limits. An unipolar PWM control is employed to the inverter as it is advantageous over that of the bipolar PWM. It has lower harmonics and has effective switching frequency as double that of the actual switching frequency. In this simulation the actual switching frequency of 10*kHz* has been used to have an effective switching of 20*kHz*. The system parameters used to simulate are as listed in the table 6. The figure 50 illustrates the related waveforms of voltage source converter, with and without the injection of reactive

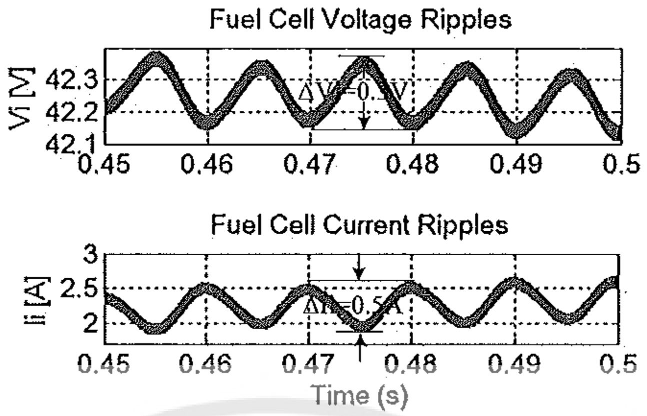

(a) Ripples at 100W load

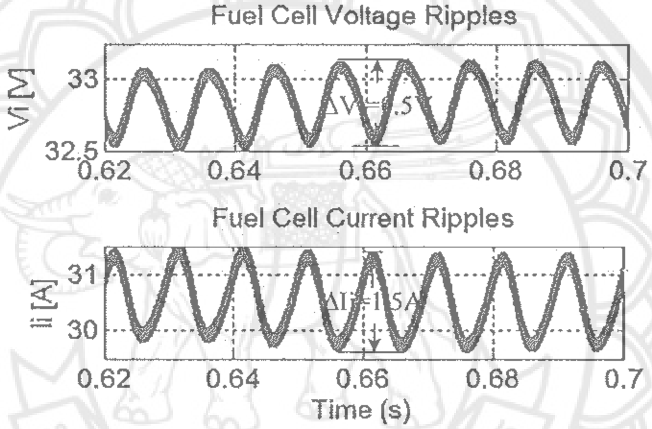

(b) Ripples at 1000W

Figure 48 Voltage and current ripples at fuel cell system

power with a $1kW$ resistive load. At $0.12s$ the current responsible for reactive power $i_{q,ref}(t)$ for a $1kVAR$ is applied. This made the VSC to absorb the reactive power which is shown as an increase in the current with a lagging power factor. The figure 50 shows the grid voltage $v_s(t)$, converter current $i_c(t)$ and the grid current $i_s(t)$ along with the reactive current injection. It has been observed that the current ripples have been increased after the injection of the reactive power. The ripples in the grid current before the injection of Q is found to be 1.6% and after the injection it increased to 3.2%. The simulated results of the VSC with $1kW$ real power is shown in the figure 51.

It is also observed that the ripples in the converter side current $\Delta i_c = 1.5A$ which is the 16% of the rated current for which the LCL is designed for. The inverter system

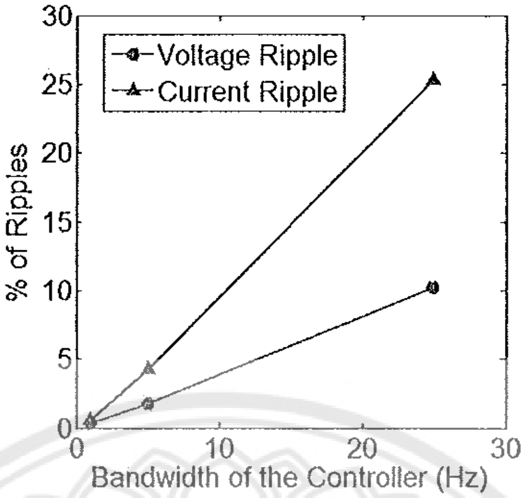

Figure 49 Percentage of ripples vs controller bandwidth

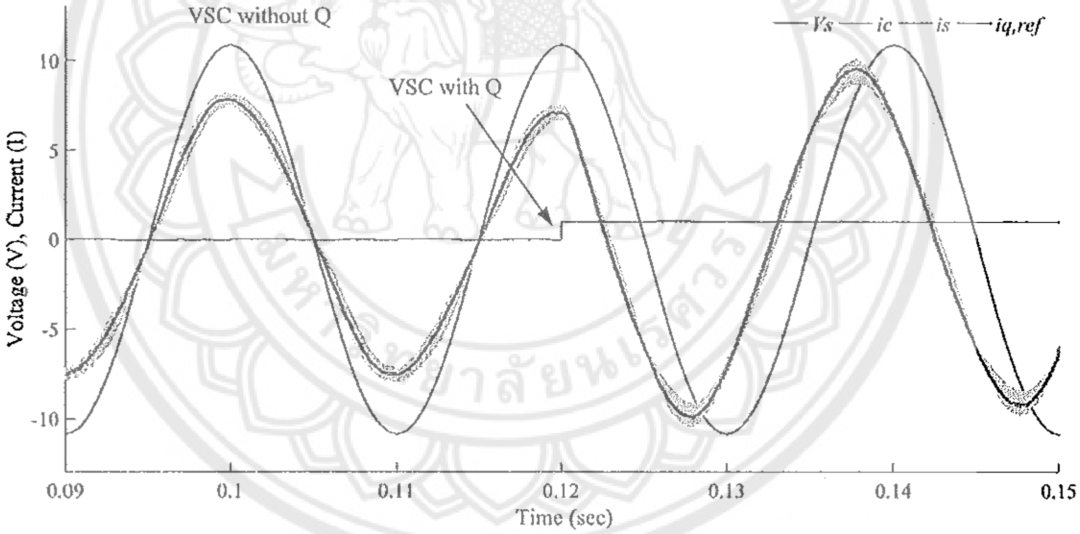

Figure 50 Simulated VSC waveforms before and after "Q" injection

with *LCL* is found to be stable with the required ripple reduction on the grid current. The grid current ripples of 1.6% without Q injection and 3.6% with Q injection are well within the permissible standards of 5% (28). Hence the simulated results of VSC with resistive load and *LCL* filter behaved as per the design considerations to meet the standards.

Table 6 Grid connected inverter system parameters

Parameter	Values
RMS line voltage, v_s	$230V$
Nominal grid frequency, f_g	$50Hz$
DC link voltage, V_{dc}	$400V$
Apparent power, S_n	$1.5kVA$
Delay time, T_d	$100\mu s$
Converter side inductance, L_c	$3.4mH$
Grid side inductance, L_s	$0.35mH$
Inductor winding resistance-converter side, R_c	0.111Ω
Inductor winding resistance-grid side, R_s	0.029Ω
Filter capacitance, C_f	$2.25\mu F$
LCL resonance frequency, f_r	$6kHz$
DC link capacitance, C_{dc}	$1100\mu F$
Switching frequency, f_s	$20kHz$
Proportional gain, Kp	0.154
Integral gain, K_i	109.8
Damping ratio, ζ	1.4

Experimental results of Dual Active Bridge

A $1kW$ DAB was constructed with the design specifications as given in the table 7. The output of the DAB was connected to a $1.5kVAR$ single phase grid connected VSC. A $1kW$ PEM fuel cell was connected to the DAB as the renewable energy source. The grid connected VSC was initially operated to charge the DC link capacitor to $380-400V$ to avoid the inrush current at the time of starting, from the fuel cell. Once the DC bus is charged, the fuel cell is started and allowed to reach the open circuit voltage of $\approx 45V$ which is about $30s$. The DAB is applied with the phase shifted control signals with 50% duty cycle. The low voltage bridge is given with leading gate signals and the high voltage bridge with lagging signals for the power transfer from the fuel cell to the grid. The sign and magnitude of the phase difference decide the amount and direction of power transfer.

Here the low voltage bridge is connected to the low voltage output of the fuel cell and the high voltage bridge is connected to the DC link capacitor. The AC link between these two bridges is provided by a $1kW$ high frequency transformer which provides the stepping up of high frequency low voltage output to high voltage along with galvanic isolation. An external inductor L_{lk} which serves as the leakage inductor for the required power transfer is connected at the high voltage side of the transformer. Though the DAB is capable of bidirectional power flow, in this study it is controlled in unidirectional flow as the source is not bidirectional.

An experimenter kit of C2000 Piccolo 32-bit microcontroller from *Texas Instruments* is used to generate the control signals required for the DAB operation. The phase shift modulation is done in open loop mode by manually adjusting the phase shift ϕ. The phase shift ϕ is gradually increased and the power transfer from the fuel cell to the grid is observed. Figure 52 shows the voltages and currents measured at the primary and secondary winding of the high frequency transformer with a phase shift of $\phi = 60°$.

The transformer is wound with a turns ratio of 1:10.6 for an input voltage of $V_{FC} = 38V$ to give an output voltage of $V_{dc} = 400V$. Due to the dynamic nature of the fuel cell, the output voltage of the fuel cell V_{FC} is not constant at $38V$ and decreases as the load increases. Hence at the operating point for $\phi = 60°$, the V_{FC} is $26V$. Hence the DAB works in boost mode and the voltage transfer ratio referred to primary $d > 1$ and is 1.46.

The ZVS nature of the DAB can be observed from the experimental result shown

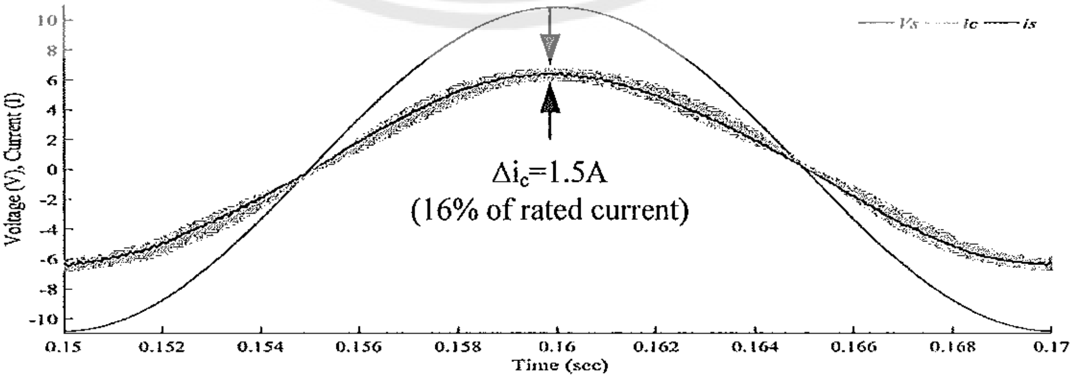

Figure 51 Simulated VSC waveform with $1kW$ resistive load

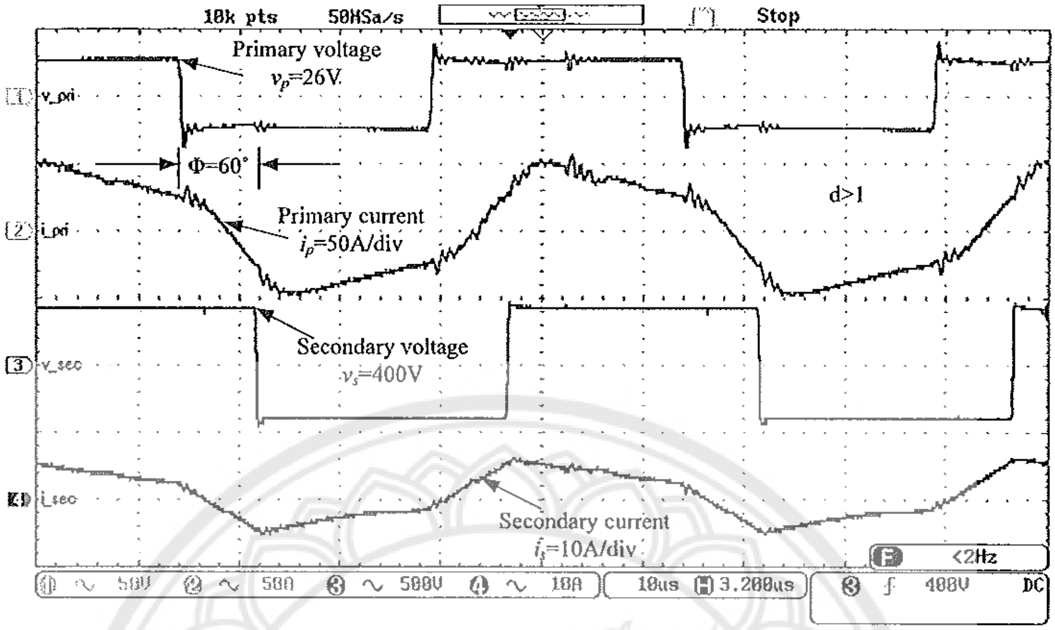

Figure 52 DAB experimental waveform with $\phi = 60°$

in figure 52 that, the input bridge is turned ON when the current negative($i_p(t) < 0$) and the output bridge is turned ON when the current is positive($i_p(t) > 0$).

Table 7 DAB system parameters

Parameter	Values
DAB ratings	$1kW$
Input voltage,V_{FC}	$38V$
Output voltage,V_{dc}	$400V$
Switching frequency,$f_{s_{DAB}}$	$20kHz$
Primary referred voltage transfer ratio, d	1 at $V_{FC} = 38V$
Turns ratio,1 : n	1 : 10.6

The figure 53 shows the DAB waveforms with the current drawn from the fuel cell. The figure 54 shows the transient response of the fuel cell voltage and current when the grid connected inverter load of the DAB is turned on and a power of 650W is exported

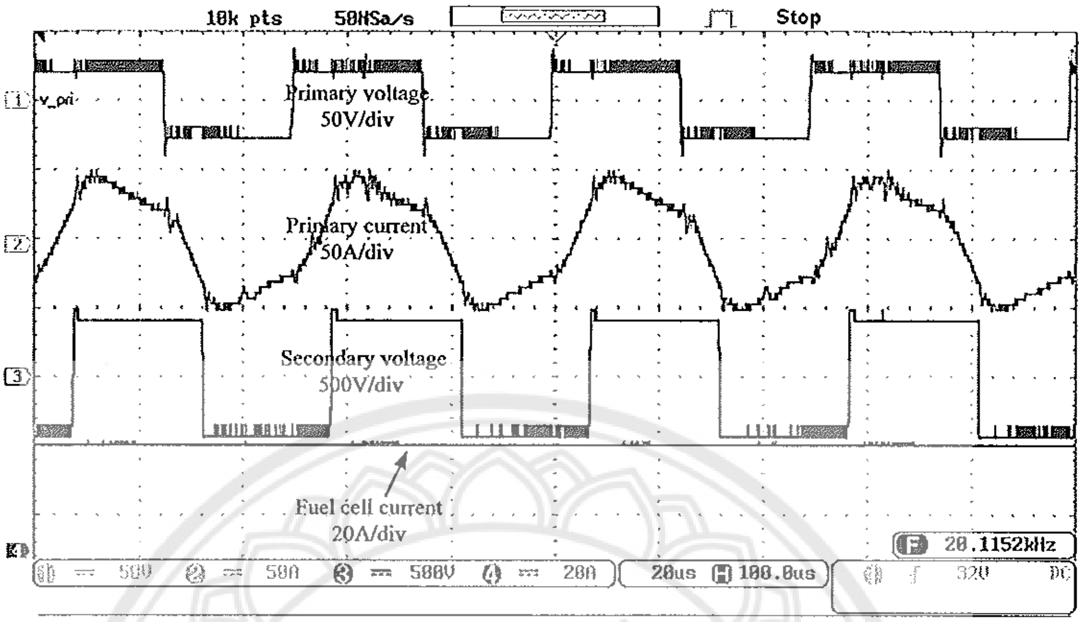

Figure 53 DAB experimental waveform with the current drawn from the fuel cell

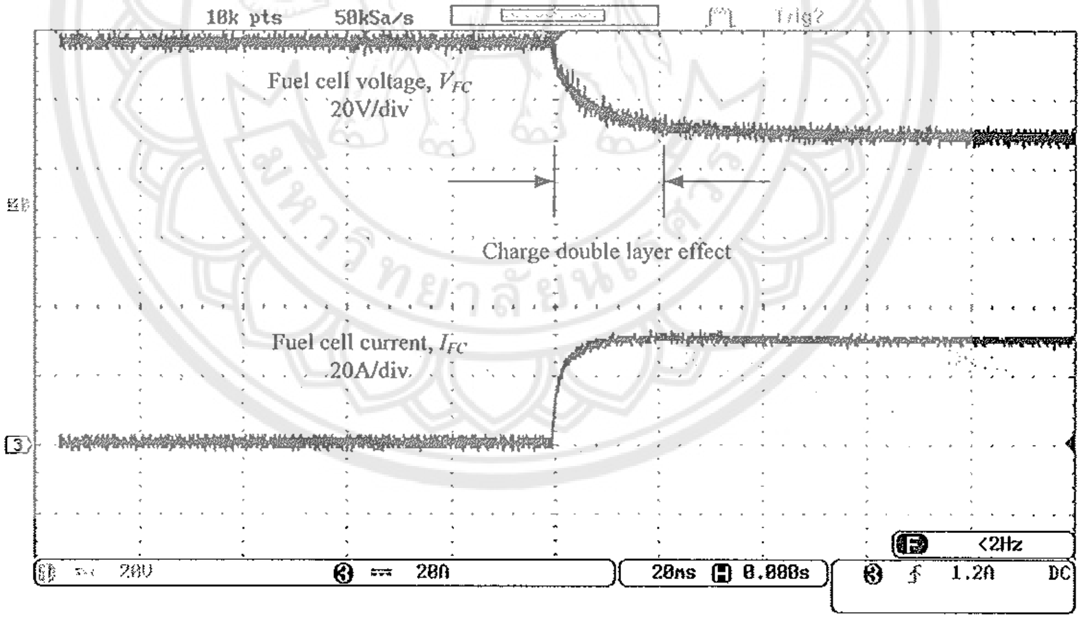

Figure 54 Fuel cell voltage and current at 650W power export to the grid

to the grid with reactive power injection.

Double layer capacitance effect can be observed from the dynamic nature of the fuel cell, the delayed change in the fuel cell voltage with respect to change in the current is due to *charge double layer* effect. This is a common phenomenon which occurs when two different materials such as electrode and electrolyte are made in physical contact. In such cases the charge from one material diffuse into the other and making a double layer of charges on the surface of the materials. In case of fuel cells electrons from electrodes and H^+ ions from electrolyte form a charge double layer with a potential difference called "activation overvoltage". These charges form a capacitive effect between the materials which takes some time to change the voltage whenever there is a change in current. The figure 54 shows the time taken for the change in the fuel cell voltage when there is a change in the current. This is due to the time required for the charge to either dissipate or to build up. The activation overvoltage does not immediately follow the current as the ohmic voltage follows. In general this charge double layer effect of this capacitance gives a smooth dynamic performance when there is a change in the current demand.

Experimental results of Grid Connected Inverter

The bidirectional VSC is initially operated in rectifier mode to charge the DC link capacitor to $400V$. Once the DC bus is charged to $400V$, the fuel cell is turned ON to reach the open circuit voltage of $45V$. When these conditions are met, the DAB is turned ON with the minimum phase shift $\phi = 18°$. After ensuring the stable operation of fuel cell, DAB and inverter, the power export is increased by phase shift modulation. The figure 55 shows the measured grid voltage and current with a reactive power injection. A phase lag in the grid current can be observed due to the reactive power injection.

Figure 55 shows the transient time response of the DC bus voltage along with the grid voltage and current at the time of 650W power export to the grid with reactive power injection.

The power was exported to the grid in controlling the DAB in open loop mode, where the phase shift is manually adjusted and the the DC bus voltage was regulated by the voltage control loop of the gird connected inverter. The figure 56 shows the dynamic response of the DC bus voltage, grid voltage and current when the power export to the grid is withdrawn.

The figure 57 is the measured grid voltage and current with reactive power injection at a load of $650W$. The figure 58 shows the ripple content THD_i in the grid current after the injection of reactive power "Q" which is measured to be 1.7% which was 5% without the injection of "Q".

The US Department of Energy standardizes the $100Hz$ ripples of the fuel cell within 15% and the THD within 5% at the output of the fuel cell inverter (61). The grid current THD_i is limited within 2% which is well below the standards which in turn reduces the double line frequency ripples injected back to the fuel cell system. This increases the reliability of the fuel cell system.

The figure 59 shows the efficiency of the overall DAB and inverter system with and without the injection of the reactive power. The power export to the grid was varied by varying the phase shift ϕ under phase shift modulation. The figure 59 illustrates that the efficiency of the system with reactive power injection as in figure 59b is lower than that of the system without reactive power injection as in figure 59a. Moreover the efficiency is lower at light loads due to higher switching losses as the DAB system operates in the boundaries of ZVS. As the power export increases, the efficiency also increases, but after certain load conditions again the efficiency decreases due to the higher voltage transfer ratio d, which makes higher voltage drop across the leakage inductor L_{lk}.

The figure 60 shows variation in THD_i at different power transfer with and without the injection of the reactive power "Q" in figures 60b and 60a respectively. The injection of the reactive power has reduced the grid current THD_i well within the

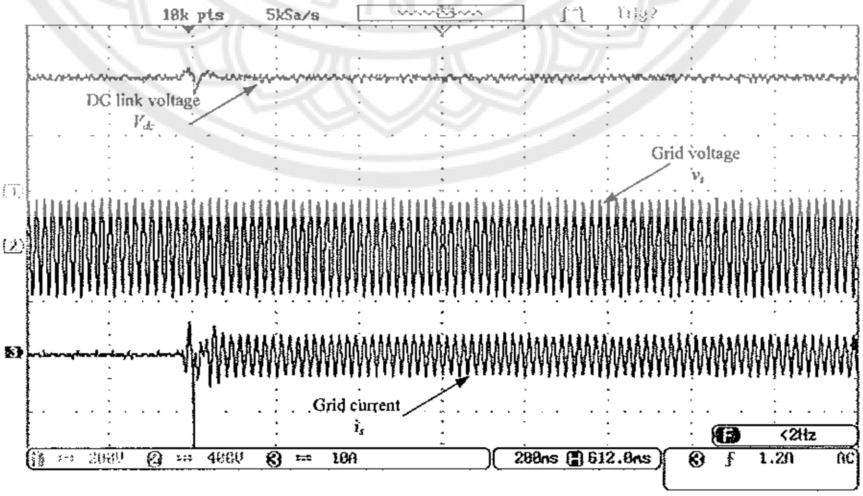

Figure 55 Experimental DC bus voltage, grid voltage and grid current with $1kVAR$ injection

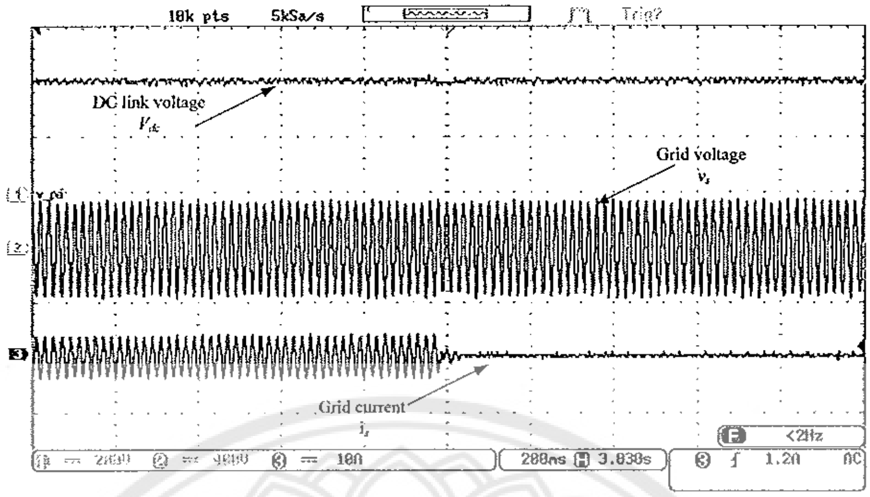

Figure 56 Experimental DC bus voltage, grid voltage and grid current upon the removal of power export to the grid

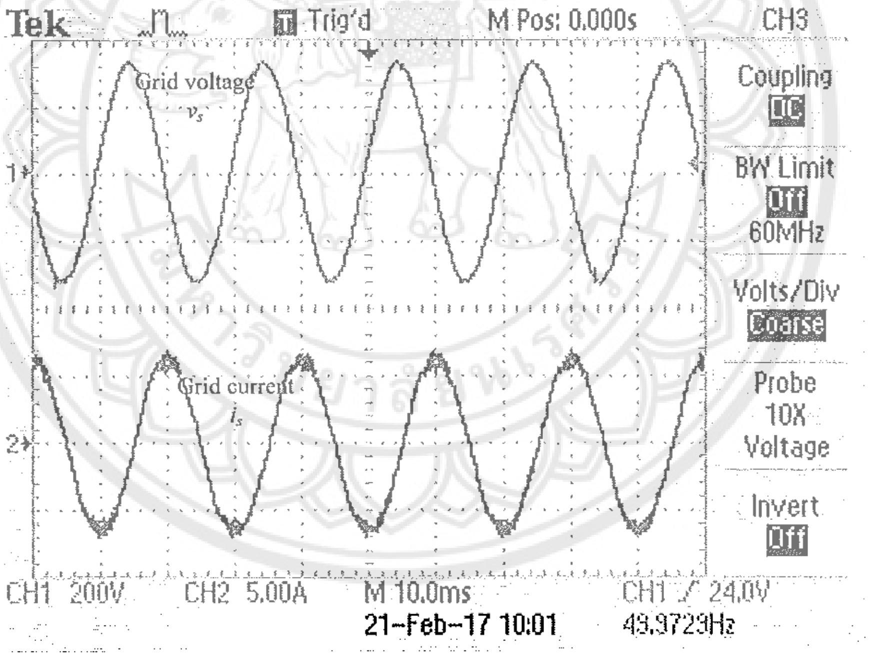

Figure 57 Measured grid side voltage and current

standards of < 5% (28).

The maximum efficiency of the DAB and inverter system is measured to be 86% with a possible grid current THD_i of 1.7% as shown in the figures 59 and 60 respectively.

The FFT analysis of the measured fuel cell current has been carried out. The raw

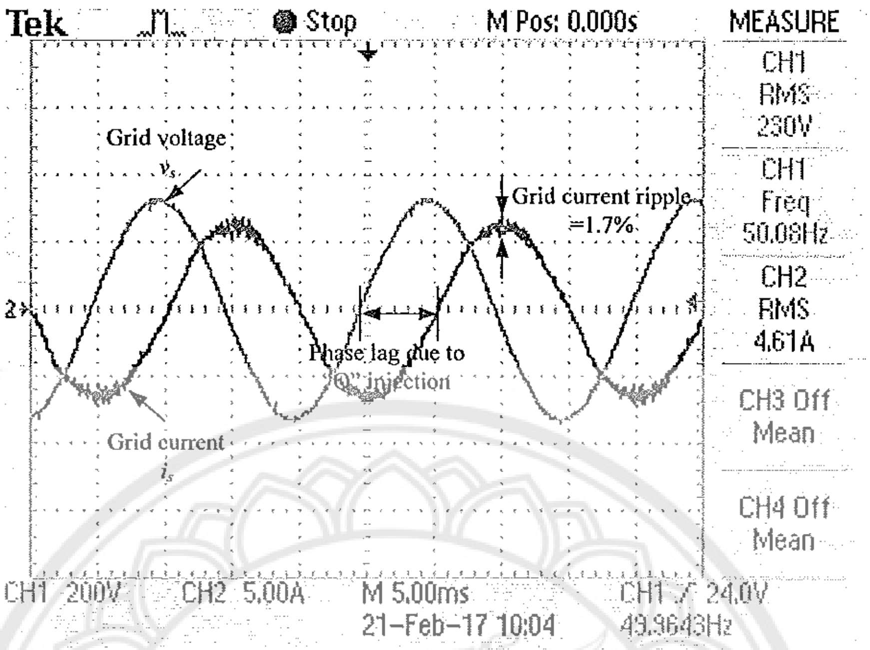

Figure 58 Measured grid side voltage and current with ripples % after "Q" injection

data has been filtered out using a digital low pass FIR filter with a pass band of $150Hz$ and a stop band of $200Hz$ to filter out the high frequency noises. The figure 61 shows the FFT of fuel cell current at 225W power export to the grid, which measured a ripple level $< 1\%$ which is well within the allowable $< 15\%$ (61)

Results comparison with the commercial products

The table 8 gives a comparison between the system under study and the commercially available single phase grid connected inverters in the similar power range. Most of the commercial products have higher efficiency due to single stage power conversion and they need higher DC input voltage range. The system under study has significantly low DC input voltage range and used multistage topology with two stage conversions. This enabled the system to be used even in the lower DC input voltage range with lower efficiency than others with lowest grid current THD_i.

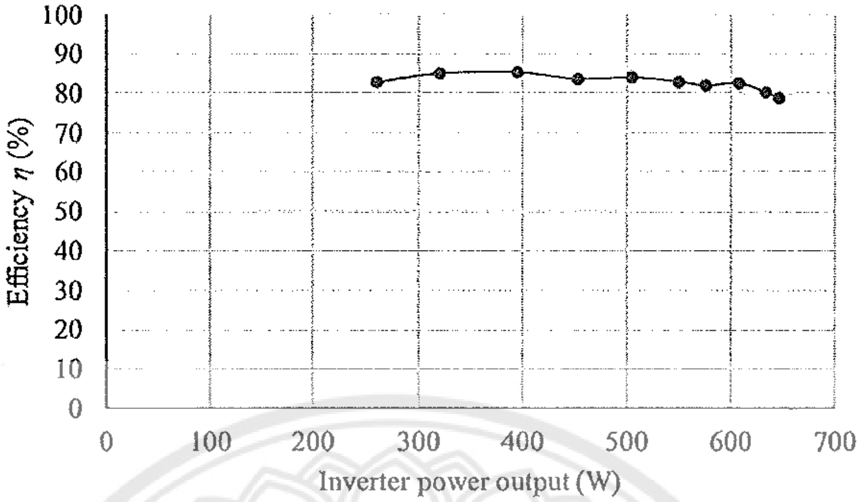

(a) Before reactive power (*Q*) injection

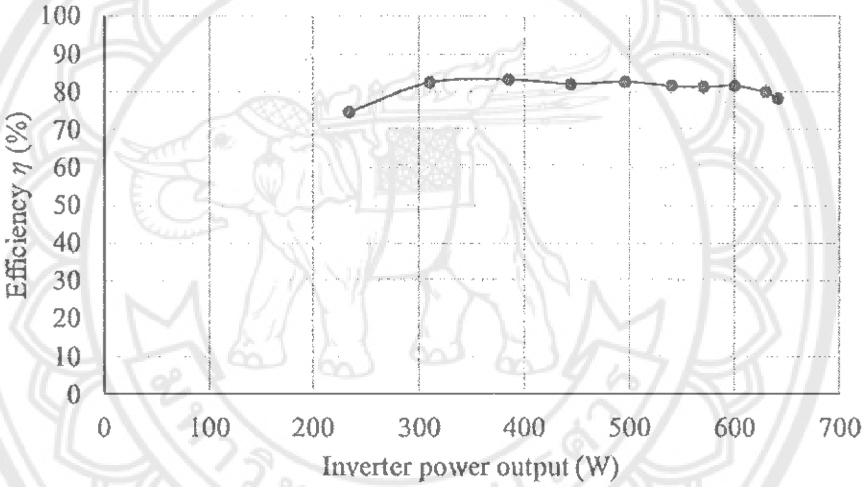

(b) After reactive power (*Q*) injection

Figure 59 Measured overall efficiency of DAB and grid connected inverter system

The figure 62 shows the experimental setup of the grid connected fuel cell power generation system. Its an integration of dual active bridge with high frequency transformer and leakage inductor, single phase grid connected inverter with *LCL* filter as shown.

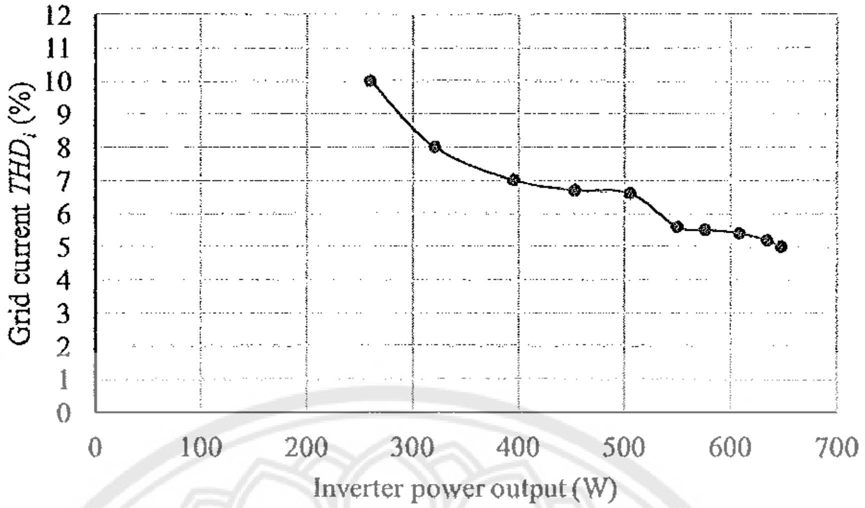

(a) Before reactive power (Q) injection

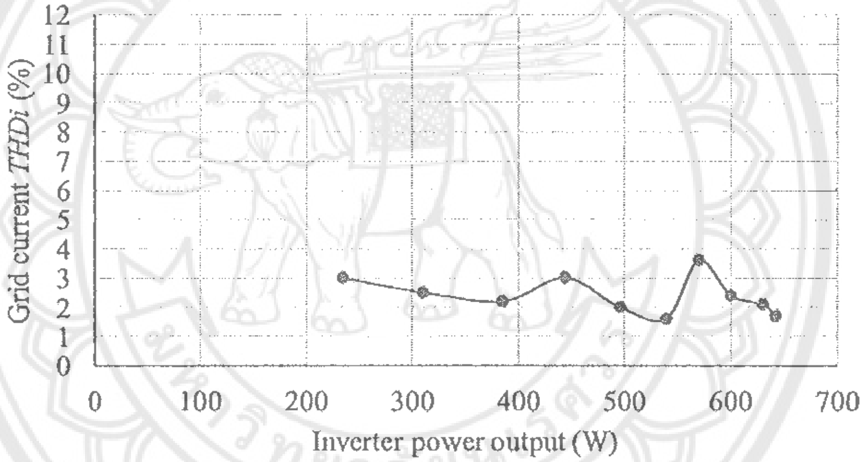

(b) After reactive power (Q) injection

Figure 60 Grid current THD_i

Table 8 Comparison of system under study with commercial products

Brand	Rated power	Rated DC input voltage	Peak efficiency	Grid current THD_i
ABB (64)	1.2kVA	185 V	94.8%	< 3.5%
Schneider (65)	2.8kW	195 - 550 V	95.2%	< 3%
Leonics (66)	1.5kW	200 - 420 V	94.3%	< 4%
System under study	1kW	30 - 38 V	86%	< 2%

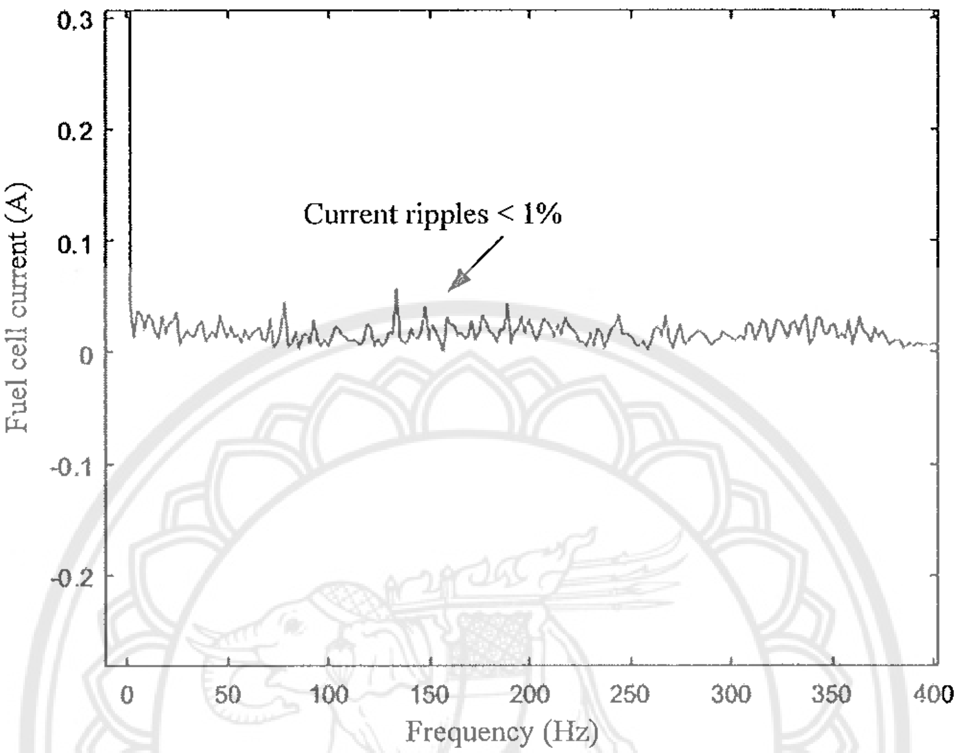

Figure 61 FFT of fuel cell current at 225W power export to the grid

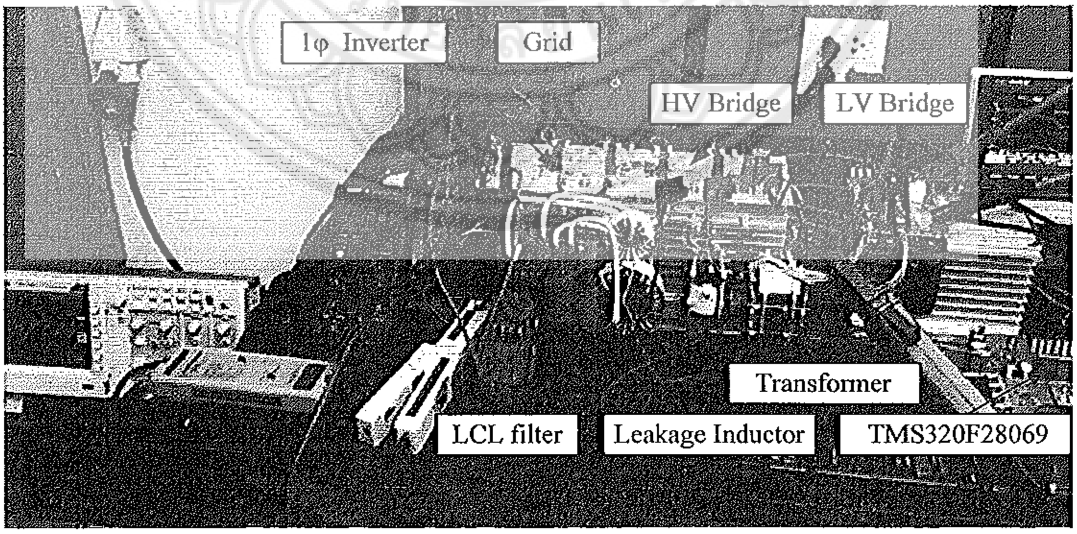

Figure 62 Experimental setup of grid connected fuel cell power generation system

CHAPTER V

CONCLUSION

This study successfully attempted to model, simulate,design and experiment a $1kW$ grid connected single phase fuel cell power generation system with higher efficiency and lower grid current THD_i. The dual active bridge DC-DC converter topology used in this study to boost the low voltage output of the fuel cell is better suited from that of the other topologies available as it has the advantages such as high efficiency, high power density, ZVS capability, galvanic isolation and simple phase shift modulation control. The simulation results have shown that the double line frequency ripples injected to the fuel cell system are reduced by controlling the bandwidth of PI controller of the DAB's voltage control loop. The external leakage inductor and the high frequency transformer designed for the power and voltage transfer could transfer the power with low switching losses due to ZVS operation with simple phase shift modulation. Usage of *Litz* wires for $20kHz$ operation reduced the losses in the magnetic components by minimizing the *skin effect*. The higher switching frequency has significantly reduced the size of the leakage inductor and the transformer. The observed shape and value of the currents in the primary and secondary of the high frequency transformer ensured the ZVS operation of the dual active bridge. The galvanic isolation by DAB enabled the system to have higher voltage transfer ratio which is primarily required for low voltage high power fuel cell systems. The external leakage inductor which is connected in series with the high frequency transformer is influenced by the leakage inductance of the transformer itself. This inevitably increases the total leakage inductance there by reduces the power transfer capability. Hence the transformer leakage inductance should be measured and considered in the design of external leakage inductor. Due to the simple phase shift modulation the power from the fuel cell is effectively transferred to single phase inverter.

The output from the DAB ranges from $325V - 400V$ due to the dynamic nature of the fuel cell making the it to operate in *buck* or *boost* mode depending on the amount of power transfer to the grid. An $1.5kVAR$ PWM controlled grid connected inverter is connected to the output DC bus of the DAB to convert and transfer the AC power

power to the grid. An *LCL* filter was designed to have higher ripple attenuation factor allowing 16% current ripples at the converter side. PLL based grid synchronization with unbalanced synchronous reference frame grid current control was effective in controlling the grid current THD_i. This enabled the independent control of the real and reactive powers in the system with their respective current component commands. The measured THD_i has proven that the grid current ripples are reduced with the injection of reactive power into the system. An injection of $1kVAR$ has reduced the grid current ripples from 5% to 1.7% for a $650W$ power transfer to the grid. Extended Symmetrical Optimum method of tuning of the PI controller with a first order low pass filter in series enabled to control the bandwidth of the controller for stable operation of the system. An overall efficiency of the grid connected inverter with Dual Active Bridge DC-DC converter for fuel cell power generation has been measured to be 86%.

The linear grid current control technique using unbalanced synchronous reference frame with PI controller has behaved as a PR controller with zero steady state error. The reduction in grid current *THDi* can be further achieved by other linear current control techniques such as Repetitive Controllers like sliding mode, odd-harmonic and dual mode repetitive controllers which nullify the steady state error by periodic control of the components there by reducing the harmonics significantly. These controllers better eliminate the harmonics but with slow dynamic behavior. The non-linear control techniques such as Predictive Control, Dead-Beat Control and Hysteresis Control reduce the harmonics with good transient response. The Predictive Controller predicts the next value of current from the present value and generates the switching states using quality function based on the error between the present and predicted current values. In such case it is possible to introduce the system non-linearities in the predictive model. The Dead-Beat controller is a simple non-linear controller with quick settling time as $n+1$ samples where n is the order of the controller. The Hysteresis Controller forces the grid current to follow the reference current within the specified Hysteresis band and the amount of current ripples can be limited by controlling the Hysteresis band.

The efficiency of the system under study can be increased further by minimizing the switching loss and conduction loss in the system. The switching loss can be reduced by fast switching devices and by ensuring ZVS operation of the DAB. The conduction loss can be reduced by *SiC* switches with low on-state losses and by minimizing the voltage drop across the leakage inductor.

Hence the clean green power from the fuel cell can be effectively integrated to the grid in support of instability due to the integration of other intermittent renewable resources in the distributed generation systems.

Recommendations

For the further research the following factors are being recommended for consideration.

1. The DAB can be controlled in closed loop to control the DC bus voltage and the fuel cell current.

2. The switching frequency of DAB can be further increased from 20*kHz* for further reduction in the size of reactive components.

3. High efficient, low loss power switches made of *Silicon Carbide* (*SiC*) can be used to improve the efficiency.

4. Other control techniques such as *Proportional Resonant* (*PR*) controllers, *Repetitive*, *Dead-Beat* and *Hysteresis* controllers can be implemented to further improve the system performance.

REFERENCES

REFERENCES

1. Dudley B. BP statistical review of world energy 2015. London, UK; 2015.

2. Blaabjerg F, Zhe C, Kjaer SB. Power electronics as efficient interface in dispersed power generation systems. IEEE Transactions on Power Electronics. 2004;19(5):1184-1194.

3. Wang Y, Chen KS, Mishler J, Cho SC, Adroher XC. A review of polymer electrolyte membrane fuel cells: Technology, applications, and needs on fundamental research. Applied Energy.2011;88(4):981-1007.

4. Larminie J, Dicks A, McDonald MS. Fuel cell systems explained: J. Wiley Chichester, UK; 2003.

5. De Doncker RWAA, Divan DM, Kheraluwala MH. A Three-Phase Soft-Switched High-Power-Density DC/DC Converter for High-Power Applications. IEEE Transactions on Industry Applications.1991;27(1):63-73.

6. Ngo T, Won J, Nam K, editors. A single-phase bidirectional dual active half-bridge converter. 27th Annual IEEE Applied Power Electronics Conference and Exposition, APEC 2012; 2012; Orlando, FL.

7. Tao H, Kotsopoulos A, Duarte JL, Hendrix MAM. Family of multiport bidirectional DC-DC converters. IEE Proc Electr Power Appl.2006;153(3):451-458.

8. Tao H, Duarte JL, Hendrix MAM. Three-port triple-half-bridge bidirectional converter with zero-voltage switching. IEEE Transactions on Power Electronics.2008;23(2):782-792.

9. Nan C, Ayyanar R, editors. Dual active bridge converter with PWM control for solid state transformer application. 5th Annual IEEE Energy Conversion Congress and Exhibition, ECCE 2013; 2013; Denver, CO.

10. Tao H, Kotsopoulos A, Duarte JL, Hendrix MAM. Transformer-coupled multiport ZVS bidirectional DC-DC converter with wide input range. IEEE Transactions on Power Electronics.2008;23(2):771-781.

11. Tao H, Kotsopoulos A, Duarte JL, Hendrix MAM, editors. Multi-input bidirectional DC-DC converter combining DC-link and magnetic-coupling for fuel cell systems. 2005 IEEE Industry Applications Conference, 40th IAS Annual Meeting; 2005; Kowloon, Hong Kong.

12. Ren P. Renewables 2015 global status report. REN21 Secretariat: Paris, France. 2015.

13. Fatih B. World energy outlook 2015. Organisation for Economic Co-Operation and Development (OECD): Paris, France. 2015.

14. Arai J, Iba K, Funabashi T, Nakanishi Y, Koyanagi K, Yokoyama R. Power electronics and its applications to renewable energy in Japan. IEEE Circuits Syst Mag.2008;8(3):52-66.

15. Bauman J, Kazerani M. A comparative study of fuel-cell-battery, fuel-cell-ultracapacitor, and fuel-cell-battery-ultracapacitor vehicles. IEEE Trans Veh Technol. 2008;57(2):760-769.

16. Kirubakaran A, Jain S, Nema RK. A review on fuel cell technologies and power electronic interface. Renewable Sustainable Energy Rev.2009;13(9):2430-2440.

17. Kirubakaran A, Jain S, Nema RK. DSP-controlled power electronic interface for fuel-cell-based distributed generation. IEEE Transactions on Power Electronics.2011;26(12):3853-3864.

18. Peng FZ, Li H, Su GJ, Lawler JS. A new ZVS bidirectional DC-DC converter for fuel cell and battery application. IEEE Transactions on Power Electronics. 2004;19(1):54-65.

19. Wu H, Xing Y, Chen R, Zhang J, Sun K, Ge H, editors. A three-port half-bridge converter with synchronous rectification for renewable energy application. 3rd Annual IEEE Energy Conversion Congress and Exposition, ECCE 2011; 2011; Phoenix, AZ.

20. Xu H, Kong L, Wen X. Fuel cell power system and high power DC-DC converter. IEEE Transactions on Power Electronics.2004;19(5):1250-1255.

21. Xin K, Khambadkone AM, editors. Dynamic modelling of fuel cell with power electronic current and performance analysis. 5th International Conference on Power Electronics and Drive Systems, PEDS 2003; 2003: Institute of Electrical and Electronics Engineers Inc.

22. Jiang W, Fahimi B. Multiport power electronic interface-concept, modeling, and design. IEEE Transactions on Power Electronics.2011;26(7):1890-1990.

23. Yu X, Starke MR, Tolbert LM, Ozpineci B. Fuel cell power conditioning for electric power applications: A summary. IET Electr Power Appl.2007;1(5):643-656.

24. Thounthong P, Tricoli P, Davat B. Performance investigation of linear and nonlinear controls for a fuel cell/supercapacitor hybrid power plant. Int J Electr Power Energy Syst. 2014;54:454-464.

25. Rodríguez A, Vázquez A, Lamar DG, Hernando MM, Sebastián J. Different purpose design strategies and techniques to improve the performance of a dual active bridge with phase-shift control. IEEE Transactions on Power Electronics.2015;30(2):790-804.

26. Tan NML, Abe T, Akagi H. Design and performance of a bidirectional isolated DC-DC converter for a battery energy storage system. IEEE Transactions on Power Electronics. 2012;27(3):1237-1248.

27. Kong X, Khambadkone AM. Analysis and implementation of a high efficiency, interleaved current-fed full bridge converter for fuel cell system. IEEE Transactions on Power Electronics.2007;22(2):543-550.

28. Basso T. IEEE 1547 Interconnection Standards. IEEE Std. 2003;1547.

29. Mahlooji MH, Mohammadi HR, Rahimi M. A review on modeling and control of grid-connected photovoltaic inverters with LCL filter. Renewable Sustainable Energy Rev. 2018;81:563-578.

30. Akhavan A, Mohammadi HR, Guerrero JM. Modeling and design of a multivariable control system for multi-paralleled grid-connected inverters with LCL filter. Int J Electr Power Energy Syst. 2018;94:354-362.

31. Eldeeb H, Massoud A, Abdel-Khalik AS, Ahmed S. A sensorless Kalman filter-based active damping technique for grid-tied VSI with LCL filter. Int J Electr Power Energy Syst. 2017;93:146-155.

32. Xue Y, Chang L, Kjær SB, Bordonau J, Shimizu T. Topologies of single-phase inverters for small distributed power generators: An overview. IEEE Transactions on Power Electronics. 2004;19(5):1305-1314.

33. Campanhol LBG, Oliveira Da Silva SA, Sampaio LP, Azauri AO, editors. A grid-connected photovoltaic power system with active power injection, reactive power compensation and harmonic filtering. 2013 12th Brazilian Power Electronics Conference, COBEP 2013; 2013; Gramado, RS: IEEE Computer Society.

34. Menniti D, Pinnarelli A, editors. A novel compensation approach for DC current component in a grid-connected photovoltaic generation system. 2012 IEEE Power and Energy Society General Meeting, PES 2012; 2012; San Diego, CA.

35. Barghi Latran M, Teke A. Investigation of multilevel multifunctional grid connected inverter topologies and control strategies used in photovoltaic systems. Renewable Sustainable Energy Rev.2015;42:361-376.

36. Hassaine L, Olias E, Quintero J, Salas V. Overview of power inverter topologies and control structures for grid connected photovoltaic systems. Renewable Sustainable Energy Rev. 2014;30:796-807.

37. Serban E, Serban H. A control strategy for a distributed power generation microgrid application with voltage- and current-controlled source converter. IEEE Transactions on Power Electronics.2010;25(12):2981-2992.

38. Rodríguez JR, Dixon JW, Espinoza JR, Pontt J, Lezana P. PWM regenerative rectifiers: State of the art. IEEE Trans Ind Electron.2005;52(1):5-22.

39. Sefa I, Altin N, Ozdemir S, Kaplan O. Fuzzy PI controlled inverter for grid interactive renewable energy systems. IET Renew Power Gener.2015;9(7):729-738.

40. Dannehl J, Wessels C, Fuchs FW. Limitations of voltage-oriented PI current control of grid-connected PWM rectifiers with LCL filters. IEEE Trans Ind Electron.2009;56(2):380-388.

41. Liserre M, Blaabjerg F, Hansen S. Design and control of an LCL-filter-based three-phase active rectifier. IEEE Transactions on Industry Applications.2005;41(5):1281-1291.

42. Reznik A, Simoes MG, Al-Durra A, Muyeen SM. LCL Filter design and performance analysis for grid-interconnected systems. IEEE Transactions on Industry Applications. 2014;50(2):1225-1232.

43. Somkun S, Chunkag V, editors. Simple and fast synchronous reference frame current control for single-phase grid-connnected votage souce converters. 41st Annual Conference of the IEEE Industrial Electronics Society, IECON 2015; 2015: Institute of Electrical and Electronics Engineers Inc.

44. Parvez M, Elias MFM, Rahim NA, Osman N. Current control techniques for three-phase grid interconnection of renewable power generation systems: A review. Sol Energy. 2016;135:29-42.

45. Somkun S, Chunkag V. Unified Unbalanced Synchronous Reference Frame Current Control for Single-Phase Grid-Connected Voltage-Source Converters. IEEE Trans Ind Electron. 2016;63(9):5425-5436.

46. Shen G, Zhu X, Chen M, Xu D, editors. A new current feedback PR control strategy for grid-connected VSI with an LCL filter. 24th Annual IEEE Applied Power Electronics Conference and Exposition, APEC 2009; 2009; Washington, DC.

47. Blaabjerg F, Teodorescu R, Liserre M, Timbus AV. Overview of control and grid synchronization for distributed power generation systems. IEEE Trans Ind Electron. 2006;53(5):1398-409.

48. Kaura V, Blasko V. Operation of a phase locked loop system under distorted utility conditions. IEEE Transactions on Industry Applications.1997;33(1):58-63.

49. Rolim LGB, Da Costa Jr DR, Aredes M. Analysis and software implementation of a robust synchronizing PLL circuit based on the pq theory. IEEE Trans Ind Electron. 2006;53(6):1919-1926.

50. Silva SM, Lopes BM, Filho BJC, Campana RP, Boaventura WC, editors. Performance evaluation of PLL algorithms for single-phase grid-connected systems. Conference Record of the 2004 IEEE Industry Applications Conference; 39th IAS Annual Meeting; 2004; Seattle, WA.

51. Guo XQ, Wu WY, Gu HR. Modeling and simulation of direct output current control for LCL-interfaced grid-connected inverters with parallel passive damping. Simul Model Pract Theory.2010;18(7):946-956.

52. Teodorescu R, Blaabjerg F, Borup U, Liserre M, editors. A new control structure for grid-connected LCL PV inverters with zero steady-state error and selective harmonic compensation. 19th Annual IEEE Applied Power Electronics Conference and Exposition - APEC 2004; 2004; Anaheim, CA.

53. Wang X, Blaabjerg F, Loh PC. Grid-current-feedback active damping for LCL resonance in grid-connected voltage-source converters. IEEE Transactions on Power Electronics.2016;31(1):213-223.

54. Büyük M, Tan A, Tümay M, Bayindir KÇ. Topologies, generalized designs, passive and active damping methods of switching ripple filters for voltage source inverter: A comprehensive review. Renewable Sustainable Energy Rev.2016;62:46-69.

55. Bao C, Ruan X, Wang X, Li W, Pan D, Weng K. Step-by-step controller design for LCL-Type Grid-Connected inverter with capacitor-current-feedback active-damping. IEEE Transactions on Power Electronics.2014;29(3):1239-1253.

56. Twining E, Holmes DG. Grid current regulation of a three-phase voltage source inverter with an LCL input filter. IEEE Transactions on Power Electronics.2003;18(3):888-895.

57. Zou C, Liu B, Duan S, Li R. Influence of delay on system stability and delay optimization of grid-connected inverters with LCL filter. IEEE Trans Ind Inf.2014;10(3):1775-1784.

58. Liu F, Zhou Y, Duan S, Yin J, Liu B. Parameter design of a two-current-loop controller used in a grid-connected inverter system with LCL filter. IEEE Trans Ind Electron. 2009;56(11):4483-4491.

59. Wandhare RG, Agarwal V. Reactive power capacity enhancement of a PV-grid system to increase PV penetration level in smart grid scenario. IEEE Trans Smart Grid. 2014;5(4):1845-1854.

60. Zong X, Lehn PW, editors. Reactive power control of single phase grid tied Voltage Sourced Inverters for residential PV application. 38th Annual Conference on IEEE Industrial Electronics Society, IECON 2012; 2012; Montreal, QC.

61. Handbook FC. EG&G technical services. Inc, Albuquerque, NM, DOE/NETL-2004/1206. 2004.

62. Preitl S, Precup RE. An extension of tuning relations after symmetrical optimum method for PI and PID controllers. Automatica.1999;35(10):1731-1736.

63. Hurley WG, Wölfle WH. Transformers and inductors for power electronics: theory, design and applications: John Wiley & Sons; 2013.

64. ABB string inverters. Available from: http://new.abb.com/power-converters-inverters/solar/string/single-phase/uno-dm-1-2kw-2-0kw-3-3kw-4-0kw-4-6kw-5-0kw-tl-plus.

65. Single phase grid-tie solar inverter. Available from: https://www.schneider-electric.com/en/product/878-2801/conext---single-phase-grid-tie-solar-inverter-tx-2800-na---2800-w-output/.

66. Grid connected inverter with isolation transformer. Available from: http://www.leonics.com/product/renewable/inverter/dl/G-4000-176.pdf.

APPENDIX

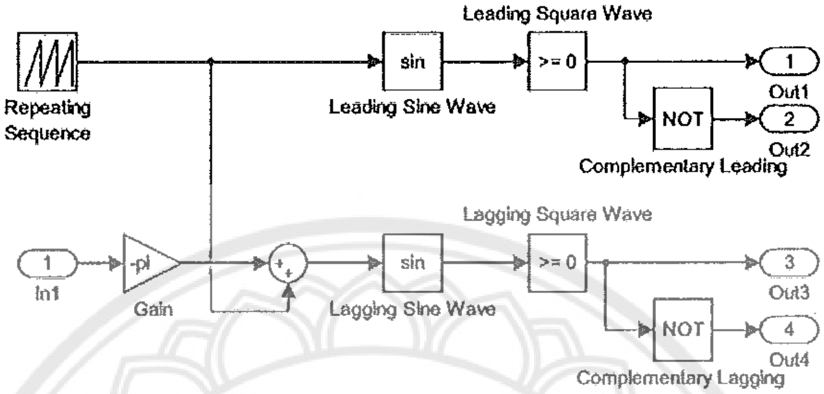

Figure 63 Gate signal generation with phase shift for DAB

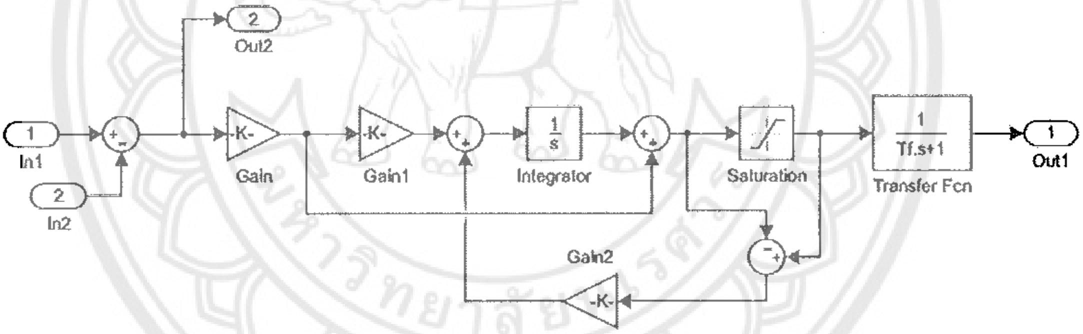

Figure 64 DAB voltage control loop

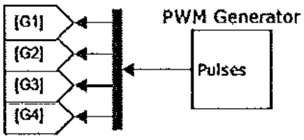

Figure 65 PWM generation for inverter

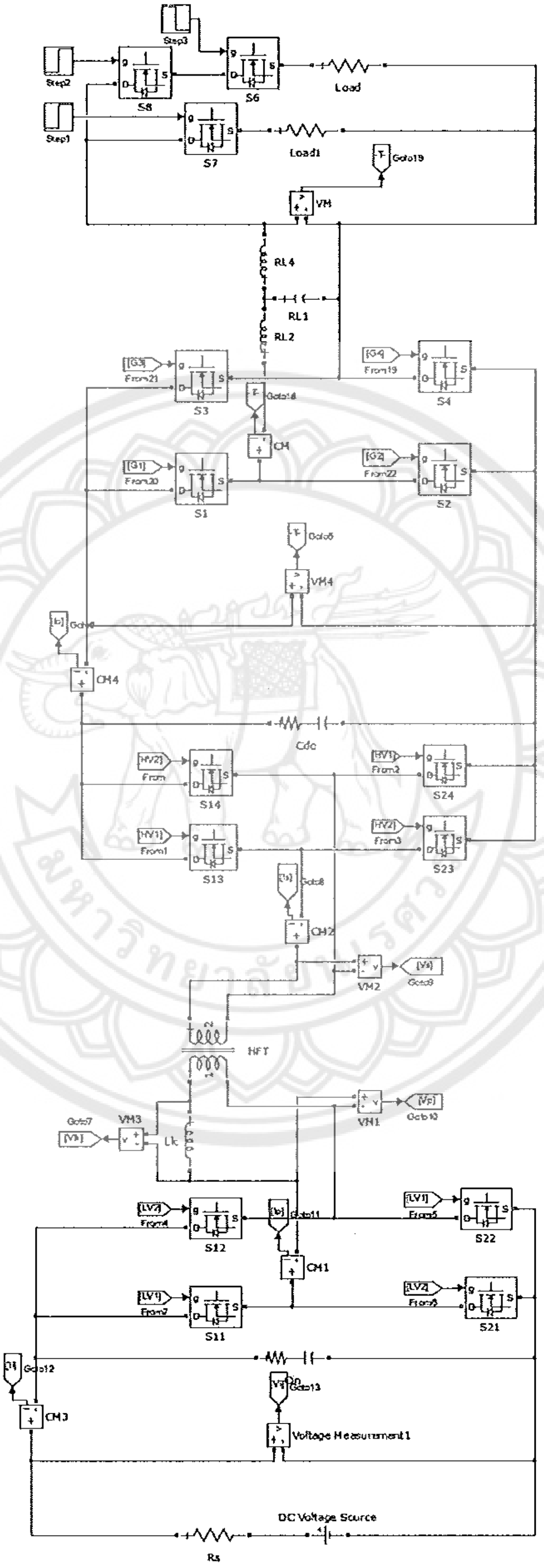

Figure 66: Simulink model of DAB with inverter